

University of St Andrews



Full metadata for this thesis is available in
St Andrews Research Repository
at:

<http://research-repository.st-andrews.ac.uk/>

This thesis is protected by original copyright

Synthesis and Microcrystal Diffraction

Studies of Zeolites

**A thesis presented by Ivor Bull B.Sc. M.Sc. to the
University of St Andrews in application for the degree
of Doctor of Philosophy**



March 2002



12 E 82

Declarations

I, Ivor Bull, hereby certify that this thesis, which is approximately 42000 words in length, has been written by me, that it is the record of work carried out by me and that it has not been submitted in any previous application for a higher degree.

Date 19 April 2002

Signature of candidate_

I was admitted as a research student in March, 1999 and as a candidate for the degree of Ph.D. in March, 2002; the higher study for which this is a record was carried out in the University of St Andrews between 1999 and 2002.

Date 19 April 2002

Signature of candidate

I hereby certify that the candidate has fulfilled the conditions of the Resolution and Regulations appropriate for the degree of Ph.D. in the University of St Andrews and that the candidate is qualified to submit this thesis in application for that degree.

Date 19 April 2002

Signature of supervisor_

In submitting this thesis to the University of St Andrews I understand that I am giving permission for it to be made available for use in accordance with the regulations of the University Library for the time being in force, subject to any copyright vested in the work not being affected thereby. I also understand that the title and abstract will be published, and that a copy of the work may be made and supplied to any *bona fide* library or research worker.

Date 19 April 2007

Signature of candidate _

Courses Attended

The Department of Chemistry requires that postgraduate students attend a number of lecture courses. These courses were "Crystallography" (Dr P. Lightfoot), "Hot Topics in Catalysis" (Prof. D. J. Cole-Hamilton and Dr P. A. Wright) and "Electronic and Magnetic Properties of Solids" (Prof. J. T. S. Irvine).

Acknowledgements

I would like to thank Professor Russell Morris, Dr Paul Wright and Dr Phil Lightfoot for their enthusiastic supervision of this project. I would also like to thank Dr Alex Slawin and Sylvia Williamson for technical help, constructive discussions and guidance. I would also like to thank Dr Simon Teat and Chui Tang for their guidance while at the CCLRC Synchrotron Radiation Source, Daresbury Laboratories, UK.

My thanks are also due to all the past and present members of the Morris group for their help and friendship over the past three years and to the technical staff of the department of chemistry of their support.

My friends "outside" of chemistry deserve a lot of credit for maintaining at least a small degree of sanity within me. There are many names but I shall especially remember my football teammates and all the people who regularly went to Dundee or the Bop.

Finally, I thank the EPSRC for funding this work.

Contents

Declarations	i
Declaration	ii
Courses Attended	iii
Acknowledgements	iv
Contents	v
Abstract	ix
Chapter 1 - Introduction	1
1.1 Definition of zeolites	1
1.2 Applications of zeolites	3
1.3 Synthesis of zeolites	5
1.4 Structure directing agents	6
1.5 Structural studies of zeolites	9
1.6 References	17
Chapter 2 - Aims of Project	22
2.1 Structural studies of zeolites	22
2.2 Synthesis of novel mixed octa-/tetra-hedral frameworks	22
2.3 References	23
Chapter 3 - Experimental	24
3.1 Hydrothermal synthesis	24
3.2 X-ray diffraction	25
3.3 Single-crystal X-ray diffraction	35
3.4 Powder X-ray diffraction	36
3.5 Variable temperature X-ray diffraction	39
3.6 Nuclear Magnetic Resonance Spectroscopy	40

3.7 Thermal Analysis	42
3.8 Other techniques	43
3.8.1 Microanalysis	43
3.8.2 Test for second harmonic generation (SHG)	43
3.9 References	43
Chapter 4 - Ferrierite	46
4.1 Introduction	46
4.2 Experimental	48
4.2.1 Hydrothermal synthesis	48
4.2.2 Calcination of ferrierite	49
4.2.3 Powder X-ray diffraction	49
4.2.4 Single crystal diffraction	49
4.2.5 Solid state NMR	50
4.2.6 DSC	50
4.3 Results and discussion	51
4.3.1 Structure of as-made ferrierite	51
4.3.2 Structure of calcined ferrierite with temperature	60
4.3.3 Second order phase transition of ferrierite	68
4.3.4 Negative thermal expansion of ferrierite	80
4.4 Conclusions	86
4.5 References	87
Chapter 5 - ITQ-4	90
5.1 Introduction	90
5.2 Experimental	92
5.2.1 Synthesis of ITQ-4	92

5.2.2 Single-crystal data collection	92
5.2.3 Solid state NMR	100
5.3 Results and discussion	101
5.3.1 Structure of [BQoI,F]-ITQ-4	101
5.3.2 Disorder	105
5.4 Conclusions	110
5.5 References	112
Chapter 6 - Disordered structures	114
6.1 Introduction	114
6.2 Experimental	115
6.2.1 Single-crystal XRD	115
6.2.2 Solid state NMR	118
6.3 Results and discussion	119
6.3.1 Structure of chabazite	120
6.3.2 Structure of MAPO-17	126
6.4 Conclusions	131
6.5 References	131
Chapter 7 - Novel Materials	133
7.1 Introduction	133
7.2 Experimental	135
7.2.1 Synthesis of scandium sulphate and scandium sulphate templated by cyclen	135
7.2.2 X-ray diffraction	136
7.2.3 Energy dispersive X-ray analysis and elemental analysis	136
7.2.4 NMR	136

7.3 Results and Discussion	
7.3.1 Structural characterisation of cyclen-scandium sulphate/phosphate	137
7.3.2.1 Structure of cyclen-ScSPO	144
7.3.2.2 Structure of cyclen-ScSO	158
7.3.3 Thermal analysis	159
7.4 Conclusions	163
7.5 References	164
Chapter 8 - Conclusions and further work	166
8.1 Summary	166
8.2 Significance of synchrotron radiation	167
8.3 Significance of the location of fluoride	167
8.4 Significance of the synthesis of novel materials	169
8.5 Further work	169
8.6 References	171

Abstract

The topic of this thesis was to obtain information concerning the synthesis and structure of zeolites towards a better understanding of their properties. Single-crystal synchrotron X-ray diffraction provided an opportunity to obtain high-resolution data. This combined with variable temperature studies provided a real opportunity to solve disorder within zeolites and to study thermal properties of zeolites. A complementary technique, solid-state nuclear magnetic resonance, was used to consolidate the presence of certain structural details such as the presence of fluoride and metallo-substitutes; disorder of fluoride; framework defects and phase transitions.

In this study the location of both fluoride and templates was resolved crystallographically in as-made ITQ-4, chabazite, and ferrierite. This provided an insight into electrostatic interactions and distortion effects which have direct structural consequences. In parallel studies, solid state NMR investigations revealed details concerning disorder with structural consequences. A comparison with MAPO-17 illustrates an alternative way of charge balancing via the metallo-substitution of magnesium for aluminium.

Variable temperature X-ray diffraction and solid state NMR reveal the siliceous form of ferrierite to be a negative thermal expansion material at low and high temperatures but in an intermediary region it undergoes a second order displacive phase transition as it expands on heating.

Finally a novel open framework scandium sulphate-phosphate is prepared hydrothermally in the presence of the azamacrocyclic cyclen (1,4,7,10-tetraazacyclododecane) in which secondary building units of formula $\text{Sc}_7(\text{S,P})_{12}\text{O}_{48}$ are linked to give a structure with supercages.

Chapter 1 - Introduction

1.1 Definition of zeolites

The classical definition of a zeolite is a crystalline, porous aluminosilicate with tetrahedral connectivity. However, this definition has been stretched by some relatively recent discoveries of materials virtually identical to the classical zeolite, but consisting of oxide structures with elements other than silicon and aluminium (e.g. lithium, titanium).^{1,2} Nowadays the definition of a zeolite now includes virtually all types of porous oxide structures that have well-defined pore structures due to a high degree of crystallinity, but still must be tetrahedrally connected.

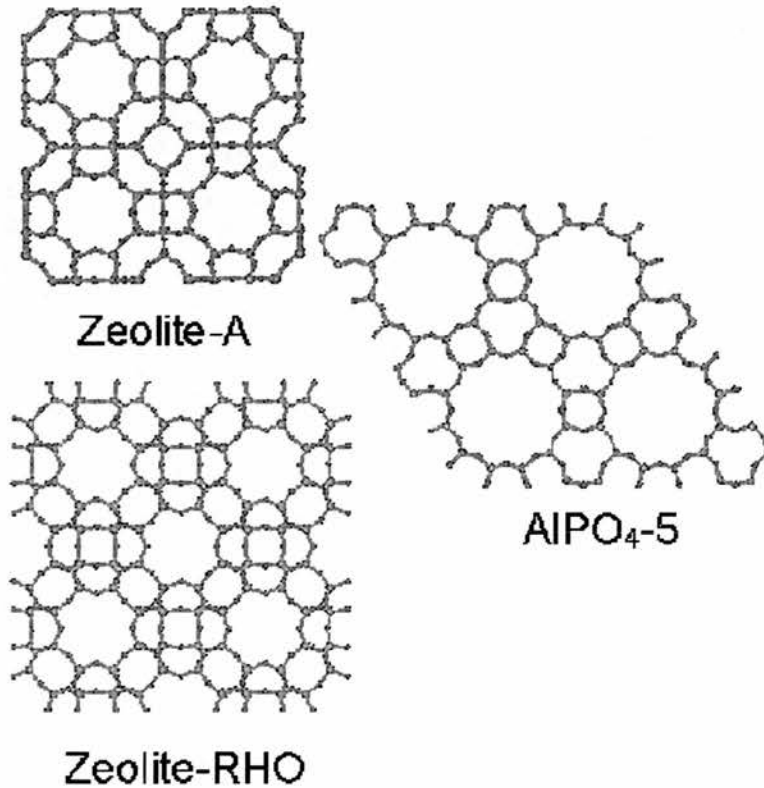


Figure 1.1 Some examples of zeolite frameworks, illustrating their porous nature.

In these crystalline zeolite materials, the metal atoms (classically, silicon or aluminium) are surrounded by four oxygen anions to form an approximate tetrahedron consisting of a metal cation at the centre and oxygen anions at the four apexes. These tetrahedral metals are called T-atoms, and these tetrahedra can stack in numerous ways to produce a variety of beautiful, regular arrays that result in channels. The many potential ways for the stacking to occur is virtually limitless, allowing for hundreds of unique structures. Figure 1.1 depicts a number of examples of these zeolite structures.

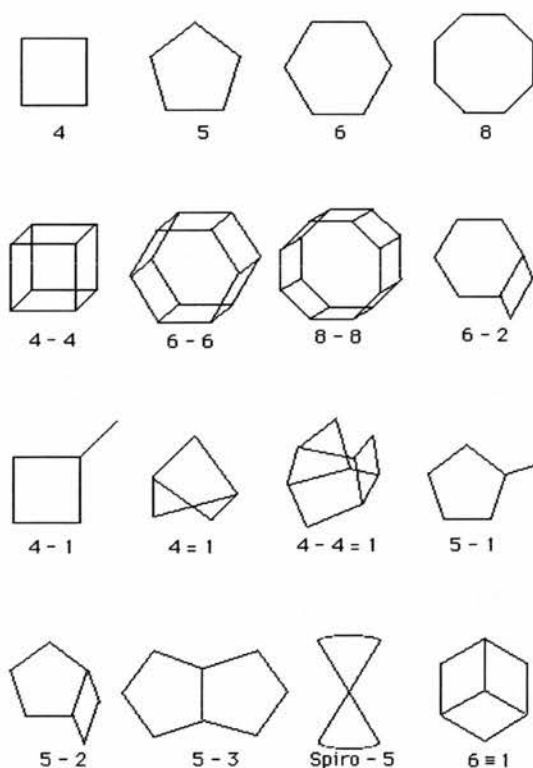


Figure 1.2 Secondary building units of zeolites.

These tetrahedral metal oxide groups are known as the primary building units of zeolites. Although they generate complicated framework networks, they first form simpler building blocks known as secondary building blocks, SBUs.^{3,4} These SBUs are geometric arrangements of the metal oxide tetrahedra (MO_4) from which all

zeolite frameworks can be formed. This is of particular importance when considering the engineering of tailored zeolitic materials and has led to numerous theoretical studies using computer modelling.^{5,6} The number of metal ions contained in the SBU defines it, for instance a double four ring unit (D4R) is composed of two rings composed of four metal atoms. This can be seen in figure 1.2 along with other common SBUs. It is important to note that the SBUs are not necessarily important in the synthetic mechanism though they are thought to be helpful in predicting structures.

1.2 Applications of zeolites

These zeolitic materials are classed by their micro- or meso-porous channels (or pores) formed by the 3-dimensional metal oxide frameworks. In fact these pores often have molecular size dimensions such that they are often termed "molecular sieves". The size and shape of the channels have extraordinary effects on the properties of these materials for adsorption processes, and this property leads to their use in separation processes. Molecules can be separated via shape and size effects related to their possible orientation in the pore, or by differences in strength of adsorption. It was in 1932 that McBain¹ recognised the application of chabazite, a zeolite, in the sorption of gases from the work of Weigel and Steinhoff.⁷ Following this Barrer^{8,9} led the way in the application of these molecular sieves to industry, in the production of pure oxygen from air. The resulting growth of zeolite research, then lead to a diverse array of zeolitic materials and a wide range of industrial applications as ion exchangers, adsorbents, catalysts, and molecular sieves.

Zeolite frameworks also lend themselves to applications in ion exchange. Silicon typically exists in a 4+ oxidation state, and the silicon-oxygen tetrahedra are

electrically neutral. However, in zeolites, aluminium typically exists in the 3+ oxidation state so that aluminium-oxygen tetrahedra form centres that are negatively charged. Thus, zeolite frameworks are typically anionic, and cations populate the pores to compensate this charge in order to maintain electrical neutrality. These cations can participate in ion-exchange processes, and this yields some important properties for zeolites. One of the most well-known ion-exchange applications is water softening (i.e. water which contains hard cations such as Calcium).¹⁰ Hard water is a problem as it does not dissolve soap well and it can cause problems such as scale in pipes, boilers and other equipment. A zeolite that contains soft cations such as sodium will exchange this with the calcium removing the unwanted properties of hard water.

If the zeolitic cations are protons, the zeolite becomes a strong solid acid. Such solid acids form the foundations of zeolite catalysis applications including the important fluidised bed cat-cracking refinery process. Other types of reactive metal cations can also populate the pores to form catalytic materials with unique properties. Thus, zeolites are also commonly used in catalytic operations and catalysis with zeolites is often called "shape-selective catalysis". The importance of these applications is exemplified by the use of zeolite Y in the catalytic cracking of crude oil to yield fuels, light oils and petrochemical feedstocks.¹¹

In addition to these chemical uses, zeolitic frameworks have potential applications wholly due to their physical properties such as negative thermal expansion, NTE. Normally materials expand on heating, however some materials can contract on heating. This unusual thermal property is actually generally exhibited by zeolites and yet there remain few detailed studies.¹²⁻¹⁴ Many materials that are already commercially utilised demonstrate problems in their working environment. For

instance, dental fillings can be known to crack due to expansion with heat. The negative thermal expansivity of these zeolites can be utilised to produce composite materials with zero expansion. Hence NTE zeolites can be used to tailor the thermal expansivity of a composite material to suit its application.

Applications of zeolites are largely dependent on their porous nature and while each year new zeolites are synthesised with different sizes of pores, more uses seem possible. The future of zeolites looks to continue to grow whether it is in catalysis, separation, thermal materials or even in something as diverse as a plant growth material.

1.3 Synthesis of zeolites

Synthesis of these materials has come a long way since Barrer⁸ redirected the

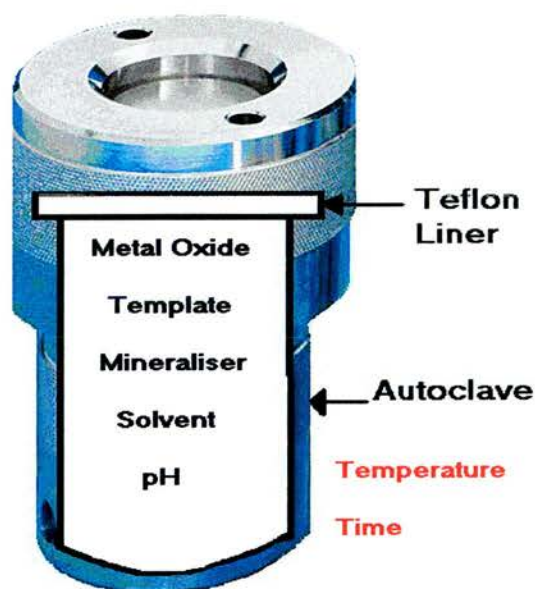


Figure 1.3 Hydrothermal bomb and experimental variables for the hydrothermal synthesis of a zeolite.

synthesis of these materials away from the high temperature chemistry, which was employed to mimic the conditions that natural zeolites were formed under in the earth's crust. He revolutionised zeolite production by applying the process of hydrothermal synthesis. Today the majority of zeolites are synthesised hydrothermally – generally carried out in polytetrafluoroethylene lined acid digestion bombs.

The ever-increasing importance of zeolites in industry means that a better understanding of their synthesis is imperative. Although the synthesis of such materials can appear to be a black art, R. Szostak¹⁵ states that several factors contribute to the successful synthesis of these materials (e.g. composition of the reaction mixture, temperature, and time). The gross composition concerns the framework constituent's ratio, OH⁻ concentration, cations (inorganic and organic), other anions, and water content as shown in figure 1.3. Much research has been carried out on understanding the gross composition and other synthesis variables (e.g. pH) in an attempt to be able to accurately engineer zeolites. It is felt that an understanding of structure directing agents, SDAs, should allow the development of zeolitic materials with predetermined physical and chemical properties.¹⁶

1.4 Structure Directing Agents

The role of SDAs is not fully understood, but it is thought that the zeolite framework grows around the template as illustrated in figure 1.4, and thus the template stabilises its surrounding cage. As a consequence the template should direct the size and shape of the zeolite pore. Crystallographic analysis of sodalite synthesised with tetramethylammonium, TMA, as an SDA shows that the TMA cation is located in the structural cavities (one SDA per cavity). Its role as a SDA is

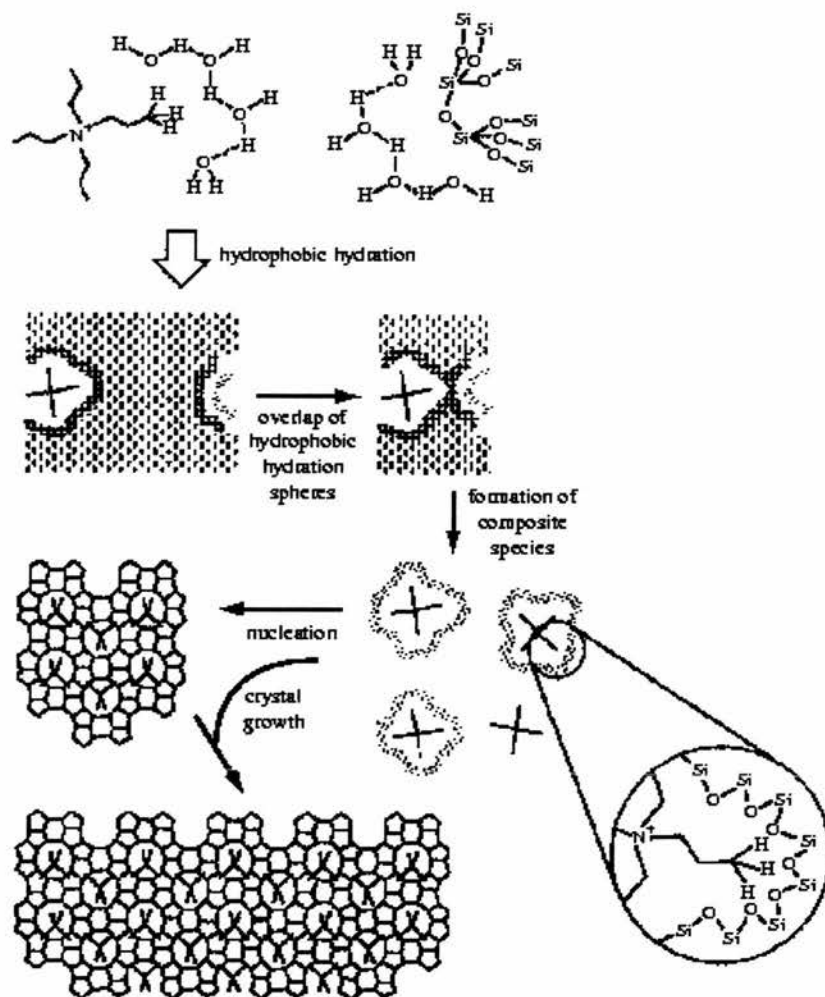


Figure 1.4 Schematic illustration of the formation of siliceous zeolite ZSM-5. Mechanism proposed by Burkett and Davis.⁶¹

further supported by the fact that TMA can not be adsorbed into the sodalite after crystal formation as the TMA is too large to enter the 6-membered ring, access to its occupied cavities.¹⁷ This shape and size correlation between the template and zeolite pore is known as the “lock and key” template theory.^{18,19} This can also be seen in the aluminophosphate STA-2 shown in figure 1.5.²⁰

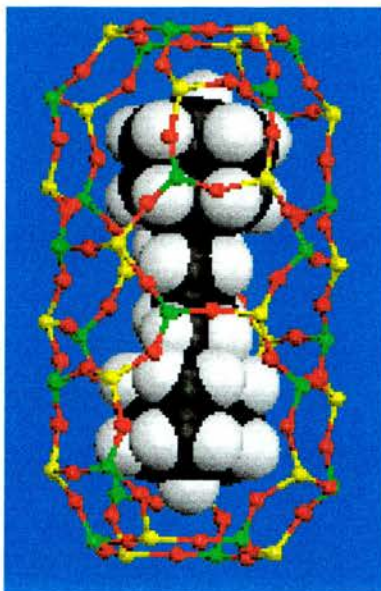


Figure 1.5 The lock and key theory of templates illustrated by the position of the template within the large cavities of STA-2. The template is shown as a space filling model and the inorganic framework by a ball and stick drawing. The aluminium, phosphorus and oxygen atoms are shown as yellow, green and red spheres respectively.

However the fact that the template, tetrapropylammonium (TPA), directs two different channel systems (ZSM-5 & ALPO₄-5) indicates templating may not be this simple.²¹⁻²³ In ZSM-5 there are clear signs of the “lock and key”, where the amine is orientated in the channel intersections and the (C₃H₇) “arms” extend into the channels of the zeolite. However in ALPO₄-5 the TPA occupies the 12 ring channels with all the “arms” lying along it. Further confusion is provided by the fact that two similar templates (TPA & tetrabutylammonium (TBA)) which only differ by one carbon in the alkyl chain produce two different channel orientations (ZSM-5 & ZSM-11, respectively).²⁴ Much work has been carried out utilising synchrotron radiation, in an attempt to fully understand templating by obtaining detailed structural information.^{17,25}

Computer modelling has contributed a great deal towards predicting the structures you may obtain using structure directing agents. In particular Catlow, Thomas et al. at the Royal Institution of Great Britain have done a great deal of work in this field.⁶

The success of this was outlined in their early work in this area where they rationalised the use of existing SDAs in chabazite and other zeolites.^{26,27} More recent work has predicted a whole range of possible structures using SDAs and knowledge of SBUs.⁵ Although this is a useful tool, often syntheses don't go as expected for a number of reasons such as template degradation in the extreme hydrothermal conditions. In addition there are other variables (such as pH, water content and temperature) which must be considered in predicting reactions.

For instance templates can act as charge balancing species and hence the space-filling role may not be the driving force. As mentioned previously zeolitic frameworks may be negatively charged when the framework metal cations are less than 4+. This template-framework charge balancing has been investigated by a number of groups around the world. Casci first showed that the same template can yield different structures dependent on the Si:Al:template ratios.²⁸ The importance of the Si:Al ratio has also been researched by Villaescusa and Cambor.²⁹ Stucky et al. has looked into these interactions in the AlPO and GaPO systems.^{30,31} Some work has been carried out examining the introduction of negative charge onto the framework by the mineraliser (F⁻), which charge balances with the template.^{32,33} This will be reported in the results sections.

A huge number of factors need to be considered when examining structural influences in zeolite formation. Hence it is necessary to scrutinise the whole of the structure to gain a fuller picture of the details of synthetic influences.

1.5 Structural studies of zeolites

A very detailed structural study of zeolites is essential to gain information towards understanding both the synthesis and applications of these materials. Growing large

enough single crystals to allow the structure to be solved using in-house single-crystal diffractometers remains difficult. Although much research concerns the growth of these crystals,³⁴ a lot of the structural work has been carried out using powder x-ray diffraction. This is clearly noted by McCusker in 1991 where she submits a paper entitled “Zeolite Crystallography - Structure Determination in the Absence of Conventional Single-Crystal Data”.³⁵ However zeolite chemistry has been revolutionised by the introduction of synchrotron radiation over the last thirty or so years.

Synchrotron radiation has made a great impact on several areas of physical and biological sciences. In the last thirty years the amount of data available on zeolite materials has exploded largely due to this. The high intensity, tunability, collimation and polarisation of the beam are some of the properties of synchrotron radiation, which provides major advantages in crystallographic studies.^{36,37} Powder and single crystal XRD benefit from the rapid data collection resulting from the high intensity. More importantly, the collimation of the beam results in very narrow, well-defined/well-resolved Bragg peaks allowing for large structure solutions. This is particularly advantageous when examining zeolites with large unit cells.³⁸

There are a number of synchrotron radiation sources around the world, the closest being in Daresbury. Each facility has a storage ring in which electrons are accelerated in a magnetic field to produce a very intense spectrum of continuous X-ray wavelengths. The energy lost in the conversion of radio frequency radiation to electromagnetic radiation is replaced by a klystron. The description that follows is the characteristics of the Daresbury Synchrotron Radiation source, but the general process can be applied to any source. Daresbury has a storage ring of 30 m diameter,

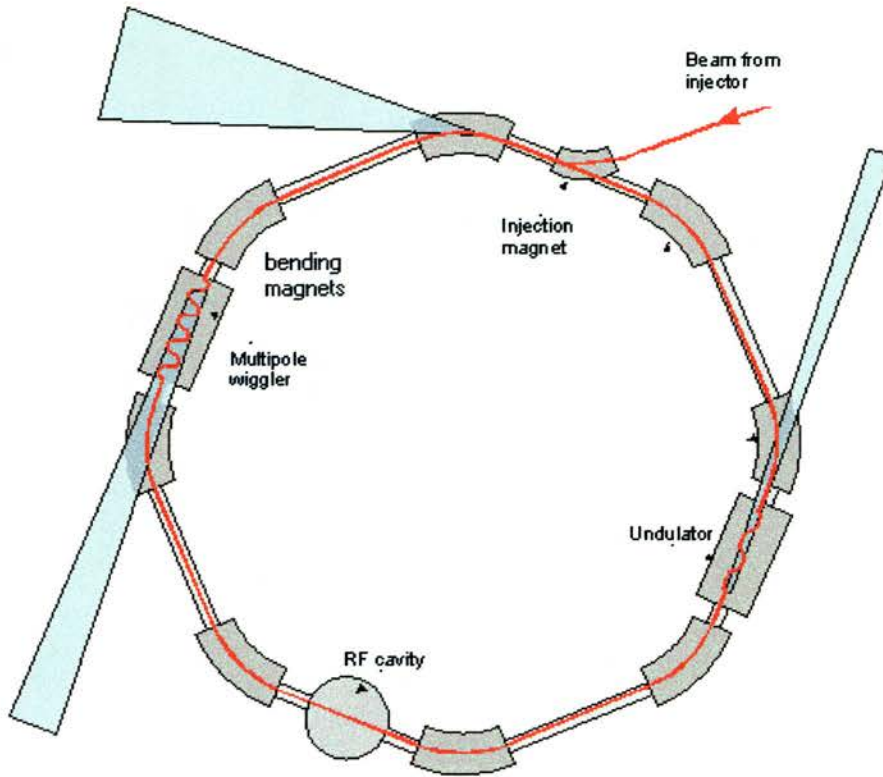


Figure 1.6 A simplified illustration of a storage ring. The beams orbit is maintained by bending magnets, which are all sources of synchrotron radiation. Specialist magnets such as wigglers and undulators are utilised to enhance specific characteristics of the radiation.

in which the electrons are accelerated to an energy of 2 GeV through a radius of 5m.

The basic components of a storage ring are illustrated in figure 1.6.

The electron beam is injected into the ring in pulses to match the klystron frequency. The beam circulates within a high vacuum chamber. In Figure 1.6 it can be seen that several magnets are involved, there are 1.2 T dipole bending magnets to bend the beam around the storage ring and maintain speed. When the beam changes direction, radiation is emitted and each bending magnet results in a fan of highly collimated synchrotron radiation in the plane of the ring as shown in Figure 1.7. The resultant broad spectrum (IR to X-rays) of radiation depends only upon the beam energy and magnetic field. Each magnet is an independent source of radiation and can then be personalised for the experimental needs of the user. Around the storage

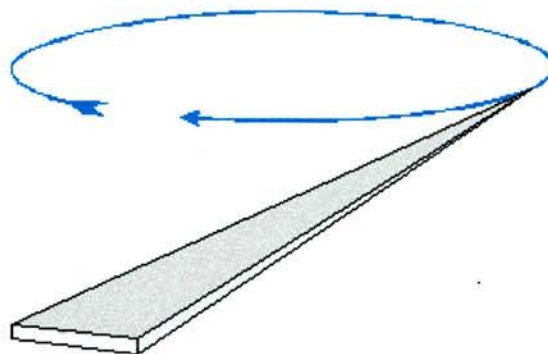


Figure 1.7 Illustration of the collimation of synchrotron radiation emitted at a dipole, bending magnet.

ring there can be anywhere between 10 – 40 stations each housing different experiments.

Magnets such as the wigglers (used to produce an additive series of X-ray beams) and undulators (used to produce interference) can be used to alter the electron beam orbit allowing for shifting the wavelength of the peak in the white continuum of synchrotron radiation. So the beam can be personalised to give intense, tuneable, highly monochromated beams of X-rays to maximise the quality of data collected.

Synchrotron radiation has particularly aided the characterisation and understanding of zeotype materials due to the improved power of powder and single crystal techniques.^{39,40} The structure solution of clathrasil phase “sigma-2” by McCusker from synchrotron powder data clearly demonstrates this power.⁴¹ The use of this technique is further illustrated by the location of the SDA in ITQ-4 by Barrett et al. from synchrotron powder data.²⁹ However Barrett et al. actually made an error in the space group assignment. A later single-crystal study showed the space group to be noncentrosymmetric instead of the previously proposed centrosymmetric space group.³² This highlights the need for single-crystal X-ray diffraction, which provides all the structural details. Single crystal diffraction also benefits from the intensity of

synchrotron radiation as now small crystals with very little scattering power can be characterised, a 6 micron crystal of CaF_2 was solved by Bachmann et al.⁴² This is known as microcrystal diffraction and zeolite chemistry still benefits from synchrotron today.⁴³⁻⁴⁶

This thesis will detail synchrotron single-crystal structural studies of zeolites and it is important to understand the importance of these studies. A greater understanding of zeolite structures has been provided by synchrotron xrd studies (both powder and single-crystal) which in turn has furthered zeolite chemistry and its applications. Single-crystal techniques are very beneficial as they provide a data set, which does not contain any information loss due to reflection overlap as seen in powder. This progression in structural studies can be seen if we consider the information collected on zeolite structures since the first zeolite structure was solved in 1930.⁴⁷ Aniline ($\text{NaAlSi}_2\text{O}_6 \cdot \text{H}_2\text{O}$) was solved from the rotating crystal method to be cubic, Ia-3d. However in these days details such as chemical composition of zeolites were still very theoretical and this is reflected in the qualitative nature of this work. Several tests were carried out in order to confirm the suggested structure. The structure contained water of crystallisation and when this was removed it produced the expected alterations in intensity of reflection of X-rays only for a very few reflections with small glancing angles. The second test involved ion exchange with silver to prove the location of the sodium ions. The changes in intensity provided a positive answer. However, there were some optical anomalies, which suggested that the crystals might not be cubic and may have tetragonal symmetry. They chose not to continue this line of thinking due to the difficulty in devising an experimental way of building up the average cubic structure from the individual units of tetragonal symmetry. This was a great piece of early work but involved a great deal of

endeavour in order to provide a realistic structure with the limited data collected. Today with modern data collection and structure solution techniques, such studies can be considered routine, as long as crystals of a suitable size are available.

In chapter four the thermal behaviour of ferrierite is discussed in great detail and the results will clearly indicate the benefits of a synchrotron single-crystal XRD study. The history of this material clearly indicates the advances made due to single-crystal data and synchrotron radiation, validating my use of this technique towards gaining more information about zeolites. Vaughan carried out the earliest structural work during the 1960s.⁴⁸ It's interesting to note that the crystals used were obtained from a natural source in Canada, which indicates the difficulty in the synthesis of zeolitic materials at that time. The structure was solved using three-dimensional Weissenberg photographs and produced an aluminium containing ferrierite, which had space group Immm. A great deal of time would have been taken to deduce the Immm structure of this natural Al-ferrierite. This technique is rarely used these days for quantitative intensity measurements as modern powder and single-crystal xrd techniques are much faster. Although there is no doubt that this is a remarkable piece of work, the details of the structure of this Al-containing zeolite would not be easily obtained from this technique. Also the human error associated with data analysis in the time before computers may have detracted from the accuracy of this solution.

A more recent single-crystal study of a naturally occurring ferrierite indicated a lowering in symmetry to $P2_1/n$.⁴⁹ It was argued Vaughan's sample had a higher magnesium content and that the $Mg-(H_2O)_6^{2+}$ situated in the cage formed by 6 rings was so tightly occupied that it sterically forced the body centred structure. A later study of synthetic ferrierites containing a variety of cations was expected to

demonstrate a lowering of symmetry. Subtle differences from the Immm structure may have been difficult to see in these powder studies.⁵⁰

Morris et al. utilised the benefits of sharper peaks and increased beam intensity obtained from synchrotron powder XRD to provide a more detailed study of a siliceous ferrierite.⁵¹ They found that the calcined siliceous ferrierite was best described as Pmnn though they couldn't rule out a further possible reduction in symmetry if data was lost due to the peak overlap problem in powder XRD. However

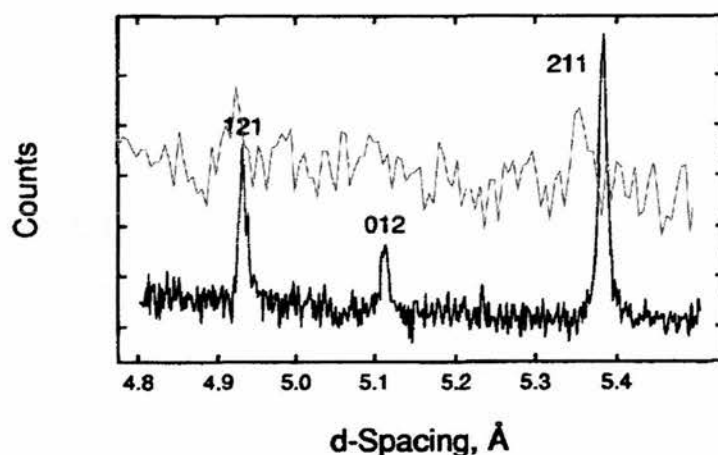


Figure 1.8 Two powder patterns collected for ferrierite – the top one is an in-house Stoe diffractometer using Cu radiation whereas the bottom one is collected using synchrotron radiation.⁵¹ The higher intensity of synchrotron radiation reveals the (012) reflection, which can not be clearly defined using our in-house diffractometer. This reflection is very important as it confirms the reduction in symmetry from Immm to Pmnn in Ferrierite.

Rietveld analysis of neutron diffraction data also produced a marked improvement when refined in Pmnn instead of Immm. This work was important, as it was a purely siliceous ferrierite framework that did not contain any framework extras such as aluminium and consequently provided an important model to compare natural ferrierites with. Up until now this was the most accurate structural study as the

synchrotron radiation produced data that revealed some subtle differences in the powder pattern which may have otherwise been missed.

During the 90s two other single crystal studies of ferrierite were carried out using the Pmnn model. Weigel et al.⁵² provided a study of the as-made ferrierite locating the template molecules. The synthesis of this material is in direct competition with the synthesis of dodecasil as they are both templated by pyridine. Close examination of both of these crystal structures, combined with computer modelling and NMR allowed this competitive reaction to be explained. The location of the propylamine in the ferrierite and not the dodecasil allowed the reaction mechanism to be postulated. These details were provided by a complete data set from a single-crystal XRD study. Lewis and co-workers⁵³ also provided a very detailed single-crystal study of ferrierite that agreed completely with this model. Though they also stated that no framework fluorine was found which had been suggested in Kuperman's work. However these single crystal studies were not carried out using synchrotron radiation which may reveal more details due to the higher resolution and intensity of the data. For instance fluorine may not have been crystallographically located using an in-house diffractometer if there was only a small amount of it there.

It has been suggested that most zeolites exhibit negative thermal expansion.⁶² So a variable temperature, single-crystal XRD study of ferrierite at a synchrotron source would be essential to examine the details of this structural phenomenon. The characterisation of this material is very important if it was to be utilised as a negative thermal expansion material.

For many zeolites the combination of synchrotron radiation with temperature studies is important for studying their structural behaviour. Low temperature techniques have been very important in solving disorder.⁵⁴⁻⁵⁶ This has also been

useful in the study of twinning,⁵⁷ and templating.^{20,32,33,58,59} It has helped in the determination of hydrogen bonding between the host and guest providing a clearer idea of how they interact.⁶⁰

Synchrotron single-crystal XRD has the potential to supply new details of zeolite structures that will uncover unknowns (synthetic, structural, properties etc) enabling a better understanding of zeolites. In most structural zeolite papers if single-crystal XRD isn't used there is normally a quote along the lines of "single crystals were not available so powder XRD was used". The single-crystal technique is largely unrivalled when it comes to supplying structural information though it information gained from additional techniques such as NMR and neutron diffraction is very beneficial. It is hoped that this knowledge should further our ability to plan zeolite syntheses and hence tailor new structures for desired applications. In addition crystallographic structures should provide a database of information from which computer modelling can be based, elucidating more information.

1.6 References

1. J.W. McBain, *The Sorption of Gases and Vapours by Solids*, Rutledge and Sons, London, 1932
2. D.S. Coombs, A. Alberti, T. Armbruster, G. Artioli, C. Colella, E. Galli, J.D. Grice, F. Liebau, J.A. Mandarino, H. Minato, E.H. Nickel, E. Passaglia, D.R. Peacor, S. Quartieri, R. Rinaldi, M. Ross, R.A. Sheppard, E. Tillmanns and G. Vezzalini, *Can. Mineral.*, 1997, **35**, 1571.
3. N. Engel, *Acta Crystallogr. Sect. B. Struct. Commun.*, 1991, **47**, 849.

4. M.M.J. Treacy, K.H. Randall, S. Rao, J.A. Perry and D.J. Chadi, *Z. Kristall.*, 1997, **212**, 768.
5. F. Cora, C.R.A. Catlow and D.W. Lewis, *J. Mol. Catal. A-Chem.*, 2001, **166**, 123.
6. C.R.A. Catlow, L. Ackermann, R.G. Bell, F. Cora, D.H. Gay, M.A. Pereira, G. Sastre, B. Slater and P.E. Sinclair, *Faraday Discuss.*, 1997, 1.
7. O. Weigel, E. Steinhoff, *Z. Kristall.*, 1925, **61**, 125.
8. R.M. Barrer, *Zeolites*, 1981, **1**, 130.
9. R.M. Barrer, *Zeolites*, 1982, **2**, 239.
10. R. Levanmao, N.T. Vu, S.Y. Xiao and A.J. Ramsaran, *J. Mater. Chem.*, 1994, **4**, 1143.
11. H.H. Kung, B.A. Williams, S.M. Babitz, J.T. Miller, W.O. Haag and R.Q. Snurr, *Top. Catal.*, 2000, **10**, 59.
12. L.A. Villaescusa, P. Lightfoot, S.J. Teat and R.E. Morris, *J. Am. Chem. Soc.*, 2001, **123**, 5453.
13. P. Lightfoot, D.A. Woodcock, M.J. Maple, L.A. Villaescusa and P.A. Wright, *J. Mater. Chem.*, 2001, **11**, 212.
14. M.P. Attfield and A.W. Sleight, *Chem. Mat.*, 1998, **10**, 2013.
15. R.M. Szostak, *Handbook of Molecular Sieves*, Van Nostrand Rienhold: New York, 1992.
16. N.Z. Logar, L. Golic and V. Kaucic, *Croat. Chem. Acta*, 1999, **72**, 187.
17. T. Soda, *Jap. Chem. Week*, 1981, 27.
18. B.M. Lok, T.R. Cannan and C.A. Messina, *Zeolites*, 1983, **3**, 282.
19. R.J. Francis and D.J. O'Hare, *J. Chem. Soc.-Dalton Trans.*, 1998, **19**, 3133.

20. G.W. Noble, P.A. Wright, and A. Kvik, *J. Chem. Soc.-Dalton Trans.*, 1997, 4485.
21. J.M. Bennett, J.P. Cohen, E.M. Flanigen, J.J. Pluth, and J.V. Smith, *ACS Sym. Ser.*, 1983, **218**, 109.
22. G.D. Price, J.J. Pluth, J.V. Smith, T. Araki and J.M. Bennett, *Nature*, 1981, **292**, 818.
23. G.D. Price, J.J. Pluth, J.V. Smith, J.M. Bennett, R.L. Patton, *J. Am. Chem. Soc.*, 1982, **104**, 5971.
24. J. B. Nagy, Z. Gabelica, and E.G. Derouane, *Zeolites*, 1983, **3**, 43.
25. G. Muncaster, G. Sankar, C.R.A. Catlow, J.M. Thomas, R.G. Bell, P.A. Wright, S. Coles, S.J. Teat, W. Clegg and W. Reeve, *Chem. Mat.*, 1999, **11**, 158.
26. D.J. Willock, D.W. Lewis, C.R.A. Catlow, G.J. Hutchings and J.M. Thomas, *J. Mol. Catal. A-Chem.*, 1997, **119**, 415.
27. G.J. Hutchings, G.W. Watson, and D.J. Willock, *Chem. Ind.*, 1997, 603.
28. J.L. Casci, *Zeolite Synthesis Using Catalytic Amounts of Template - Structure Blocking Effects and Stoichiometric Syntheses*; Elsevier Science Publ B V: Amsterdam, 1994; Vol. 84, pp 133.
29. P.A. Barrett, M.A. Cambor, A. Corma, R.H. Jones and L.A. Villaescusa, *J. Phys. Chem. B*, 1998, **102**, 4147.
30. X.H. Bu, P.Y. Feng, and G.D. Stucky, *Science*, 1997, **278**, 2080.
31. P.Y. Feng, X.H. Bu, G.D. Stucky, *Nature*, 1997, **388**, 735.
32. I. Bull, L.A. Villaescusa, S.J. Teat, M.A. Cambor, P.A. Wright, P. Lightfoot, and R.E. Morris, *J. Am. Chem. Soc.*, 2000, **122**, 7128.
33. L.A. Villaescusa, P.S. Wheatley, I. Bull, P. Lightfoot, and R.E. Morris, *J. Am. Chem. Soc.*, 2001, **123**, 8797.

34. S.L. Qiu, W.Q. Pang, and R.R. Xu, *Synthesis of large crystals of molecular sieves - A review*; Elsevier Science Publ B V: Amsterdam, 1997; Vol. 105, pp 301.
35. L.B. McCusker, *Acta Crystallogr. Sect. A*, 1991, **47**, 297.
36. C.R.A. Catlow and G.N. Greaves, *Applications of synchrotron radiation*, Blackie: Glasgow, 1990.
37. P. Coppens, *Synchrotron radiation crystallography*, Academic Press: London, 1992.
38. H.M. Rietveld, *J. Appl. Cryst.*, 1969, **2**, 65.
39. A.R. West, *Solid state chemistry and its applications* Chichester, 1984; Vol. Wiley.
40. L.B. McCusker, R.B. Von Dreele, D.E. Cox, D. Louer and P. Scardi, *J. Appl. Crystallogr.*, 1999, **32**, 36.
41. L.B. McCusker, *J. Appl. Crystallogr.*, 1988, **21**, 305.
42. R. Bachmann, H. Kohler, H. Schulz and H.P. Weber, *Acta Crystallogr. Sect. A*, 1985, **41**, 35.
43. D.S. Wragg, and R.E. Morris, *J. Phys. Chem. Solids*, 2001, **62**, 1493.
44. A. Tripathi, J.B. Parise, S.J. Kim, Y.J. Lee, and Y.S. Uh, *Acta Crystallogr. Sect. C-Cryst. Struct. Commun.*, 2001, **57**, 344.
45. Y. Lee, J.B. Parise, A. Tripathi, S.J. Kim, and T. Vogt, *Microporous Mesoporous Mat.*, 2000, **39**, 445.
46. M.J. Gray, J.D. Jasper, A.P. Wilkinson and J.C. Hanson, *Chem. Mat.*, 1997, **9**, 976.
47. W.H. Taylor, *Z. Kristall.*, 1930, **74**, 1.
48. P.A. Vaughan, *Acta Crystallogr.*, 1966, **21**, 983.

49. R. Gramlichmeier, V. Gramlich, and W.M. Meier, *Am. Miner.*, 1985, **70**, 619.
50. I.J. Pickering, P.J. Maddox, J.M. Thomas and A.K. Cheetham, *J. Catal.*, 1989, **119**, 261.
51. R.E. Morris, S.J. Weigel, N.J. Henson, L.M. Bull, M.T. Janicke, B.F. Chmelka and A.K. Cheetham, *J. Am. Chem. Soc.*, 1994, **116**, 11849.
52. S.J. Weigel, J.C. Gabriel, E.G. Puebla, A.M. Bravo, N.J. Henson, L.M. Bull and A.K. Cheetham, *J. Am. Chem. Soc.*, 1996, **118**, 2427.
53. J.E. Lewis, C.C. Freyhardt and M.E. Davis, *J. Phys. Chem.*, 1996, **100**, 5039.
54. S.J. Andrews and A.J. Welch, *Inorg. Chim. Acta - Art. Let.*, 1984, **88**, 153.
55. J.M. Newsam, C.Z. Yang, H.E. King, R.H. Jones and D. Xie, *J. Phys. Chem. Solids*, 1991, **52**, 1281.
56. F. Porcher, M. Souhassou, H. Graafsma, A. Puig-Molina, Y. Dusausoy and C. Lecomte, *Acta Crystallogr. Sect. B - Struct. Sci.*, 2000, **56**, 766.
57. B.B. Iversen, A. Darovsky, R. Bolotovskiy and P. Coppens, *Acta Crystallogr. Sect. B-Struct. Sci.*, 1998, **54**, 174.
58. A.N. Christensen, P. Norby, J.C. Hanson, *Microporous Mesoporous Mat.*, 1998, **20**, 349.
59. N. Zakowsky, P.S. Wheatley, I. Bull, M.P. Attfield and R.E. Morris, *J. Chem. Soc., Dalton Transactions*, 2001, **19**, 2899.
60. S.B. Hong, M.A. Camblor and M.E. Davis, *J. Am. Chem. Soc.*, 1997, **119**, 761.
61. S.L. Burkett and M.E. Davis, *Chem. Mater.*, 1995, **7**, 1453.
62. P. Lightfoot, D.A. Woodcock, M.J. Maple, L.A. Villaescusa and P.A. Wright, *J. Mater. Chem.*, **11**, 212.

Chapter 2 – Aims of Project

2.1 Structural Studies of Zeolites

The driving force for this project is the search for a better understanding of the synthesis, structure and applications of zeolitic materials. It is hoped that this will eventually lead to the rational design of zeolites for specific applications.¹ As discussed in the previous chapter, synchrotron radiation allows the collection of accurate single-crystal X-ray diffraction data from microcrystals. The first objective is to utilise these high flux synchrotron X-rays and the variable temperature facilities at Station 9.8 to obtain valuable information on the negative thermal expansion of ferrierite in order to learn more about this phenomenon and to evaluate the application of this material to NTE materials.

In addition low temperature single-crystal X-ray diffraction should allow the location of templates and fluorine in existing zeolite materials.² This should provide valuable information towards understanding the host-guest relationships and an insight into synthetic influences.

Lastly, it is hoped that utilising the strengths of Station 9.8 we can solve the structure of novel zeolite materials.

2.2 Synthesis of novel mixed octa-/tetra-hedral frameworks

The rational design of new materials is an important goal for zeolite chemists in order to provide varied structures for new technologies. Recently, the US Department of Energy identified the preparation of tailored porous solids as a major challenge and stated potential applications in areas such as shape selective gas or liquid

permiselective membranes, catalytic membrane reactors, energy storage systems, molecular electronic and optoelectronic devices, as well as biomolecule separation, isolation and delivery.³

The study of structurally diverse framework solids is flourishing.⁴ The realisation that most of the elements in the Periodic Table can be incorporated has stimulated the preparation of very many new structures of this type. A key area for the discovery of structures with novel properties is that of frameworks containing both tetrahedrally- and octahedrally-coordinated cations. By experimenting with a range of metal cations that have not yet been used in the hydrothermal synthesis of this kind, such as scandium, it is hoped that novel frameworks can be formed.

2.3 References

1. R.E. Morris and P.A. Wright, *Chem. Ind.*, 1998, **7**, 256.
2. S.J. Andrews and A.J. Welch, *Inorg. Chim. Acta - Art. Let.*, 1984, **88**, 153.
3. T.J. Barton, L.M. Bull, W.G. Klemperer, D.A. Loy, B. McEnaney, M. Misono, P.A. Monson, G. Pez, G.W. Scherer, J.C. Vartuli and O.M. Yaghi, *Chem. Mater.*, 1999, **11**, 2633.
4. J. Rocha and M.W. Anderson, *Eur. J. Inorg. Chem.*, 2000, **10**, 801.

Chapter 3 – Experimental

3.1 Hydrothermal Synthesis

Zeolites are generally prepared using the hydrothermal process, in which the reaction is carried out under high pressure and temperatures in the range of 373 to 473 K.¹ The process involves four stages, the formation of the reaction gel, ageing of this gel, hydrothermal treatment and quenching to produce the product. A gel is prepared including the metal oxide sources, organic template, solvent, and sometimes a mineraliser. A typical gel for an AlPO will have a molar ratio of 1:2 of alumina and phosphoric acid dissolved in 80 molar equivalents of water with 0.5 molar equivalents of the templating amine. The gel is homogenised by stirring and is aged for a time normally about one hour. Following this it is transferred to a Teflon-lined autoclave and heated for a period of days or weeks, after which it is quenched to yield the product from the reaction temperature. The products are recovered by vacuum filtration, washed and dried. Sonication in distilled water may be required to separate crystals from powder.

These days there are many varied microporous structures (such as silicalites, GaPOs, and octahedral/tetrahedral frameworks) which are formed from diverse gel compositions.² Some gels are clear liquids whereas others are a solid paste. Design of these reactions involves carrying out a series of these reactions using the same template with varying the pH and water (or solvent) content. Zeolite crystallisation is a very complex phenomenon which can not be described just by the gel composition, reaction pressure and temperature. It involves polymerisation-depolymerisation, solution-precipitation, nucleation-crystallisation, and other complex phenomena encountered in aqueous colloidal dispersions.³ It still remains a black art to some

extent. However, the more information we can obtain, either by structural studies of the products or in situ observation of the process itself, the nearer we come to understanding this process.

3.2 X-ray Diffraction

A crystalline solid is characterised by its regular, ordered arrangement. The simplest repeating unit of a crystalline structure is known as the unit cell. This is defined by three translations a , b , and c and three angles α , β , and γ . The translational periodicity of crystals is called its lattice, i.e. a periodic collection of points separated by intervals a , b , c along the same three directions. In this three-dimensional ordered array we can locate sets of lattice planes which must be parallel and equally spaced. The reciprocals of these intercepts are the miller indices and each plane can be identified by its h,k,l indices. An example is shown in figure 3.1. In inorganic

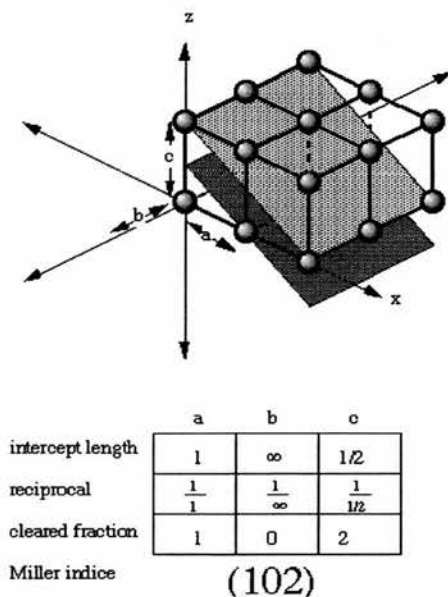


Figure 3.1 An example of a family of lattice planes described by the miller plane (102) (diagram by Dr David Jessey, California State Polytechnic University).

chemistry the determination of structural information (such as interatomic distances and bond angles) is obtained from X-ray diffraction.⁴

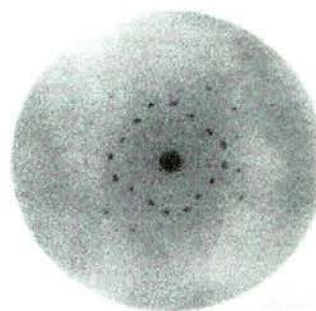


Figure 3.2 Picture of a X-ray diffraction pattern from a Copper Sulphate Crystal

Max von Laue first recognised that crystals diffracted X-rays in 1912 and was awarded the Nobel Prize in physics for this work. An example of this can be seen in figure 3.2 where a beam of X-rays was diffracted by a crystal of copper sulphate to give a characteristic pattern. In 1915 Bragg quantitatively described the conditions of diffraction by a simple relationship known as the Bragg equation:

$$n\lambda = 2d\sin\theta \quad (3.1)$$

He considered diffraction as the reflection of X-rays by the lattice planes of atoms and then the interactions of these as shown in figure 3.3. Where θ is the angle between the incident beam and the lattice plane (described by the family of Miller

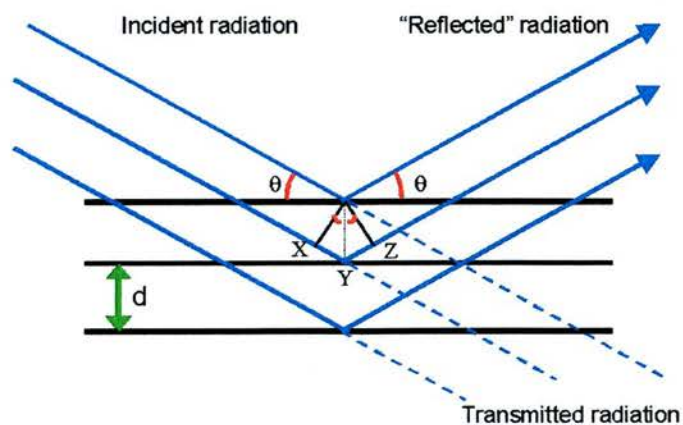


Figure 3.3 Reflection of X-rays by the lattice planes as described by Bragg, where d is the interatomic spacing.

planes (h,k,l) they belong to); d is the distance between atomic layers and $2d\sin\theta$ is the path difference (equal to the distance XY+YZ) between waves scattered between these layers which belong to the same family of h,k,l's; and λ is the wavelength of the incident radiation, where n is an integer. The wavelength of X-rays is of the same order of magnitude as interatomic distances ($\sim 10^{-9}$ m), therefore they are diffracted by a crystal lattice.⁵

If the path difference is a multiple of λ (i.e. an integer) then the waves combine by maximum constructive interference. However, as the incident beam penetrates into the crystal it will be reflected by a great number of lattice planes and if these reflected beams are out-of-phase then this would result in destructive interference. As a consequence of this behaviour we can obtain a x-ray diffraction pattern for a crystal with peaks at θ values that correspond to each of the d-spacings, which characterise this crystal's structure. Measurement of the diffraction pattern geometry and symmetry reveals the unit cell dimensions and provides some useful information about how the molecules are ordered in the unit cell. However for the full structural solution a detailed examination of the intensities is required.

By taking the individual intensities and adding together all these individual waves with correct amplitudes and phases the positions of the atoms can be worked out. This is known as a Fourier transform. X-rays are scattered by the electrons surrounding the atomic nuclei. The degree of this scattering increases with the number of electrons around the atomic nuclei and hence with atomic weight. However it also decreases with increasing 2θ . What is important is the intensity therefore gives information about the electron density and the Fourier transform of the diffraction pattern gives us the electron density and vice-versa.

A series of mathematical equations describe this Fourier Transform and it considers the intensity to be proportional to the square of the structure factor amplitude, $|F(hkl)|$ and a scalar number. This structure factor for a reflection h,k,l is a complex number that can be derived in the following equation:

$$F_{(h,k,l)} = \sum_{j=1}^{\text{atoms}} f_{(j)} \exp[2\pi \cdot i(hx_{(j)} + ky_{(j)} + lz_{(j)})] \quad (3.2)$$

This is a simple summation which extends over all atoms j , with x,y , and z their fractional coordinates. The $f(j)$ is the scattering factor of atom j and depends on the atom type and the diffraction angle of the corresponding reflection (h,k,l) . For $h,k,l = 0$, f equals the atom's number of electrons. So the dimension of $F(hkl)$ then must be electrons. The exponent is *complex* (notice the i in there) with x,y,z the fractional coordinates of each atom in the summation, and h, k, l the three indices of the corresponding reflection. Formula 3.2 shows that if the structure is known, then structure factors can easily be calculated. However in crystallography we know the structure factors (i.e. the intensities) but, not the phases and we wish to determine the structure. Consequently a reverse Fourier transform is required to determine the electron density as shown in equation 3.3.

$$\rho_{(x,y,z)} = \frac{1}{V} \sum_h \sum_k \sum_l F_{(h,k,l)} \exp[-2\pi \cdot i(hx + ky + lz)] \quad (3.3)$$

$F(hkl)$ is in units of electrons and the sum is divided by the cell volume V . The summation is done for each position x,y,z in the (normalised) unit cell. Note also the minus sign now preceding the exponent, as this is transforming an "inverse" space (the h,k,l 's are actually derived from fractional numbers $(1/h,1/k,1/l)$ designating

where corresponding lattice planes intersect the unit cell as mentioned earlier in defining miller indices) into a real or direct space (the electron density at a real point x,y,z in space). So the diffraction pattern (an image of the reciprocal space) is transformed back into the real space of electron density. This transformation is accurate and in principle complete. The crystallographic aim has now been met if the structure factors are known (inverse space from diffraction by electrons) and the actual real structure (the electron density in real space) can be calculated.

However there is a problem, $|F(hkl)|$ only provides information on the amplitude

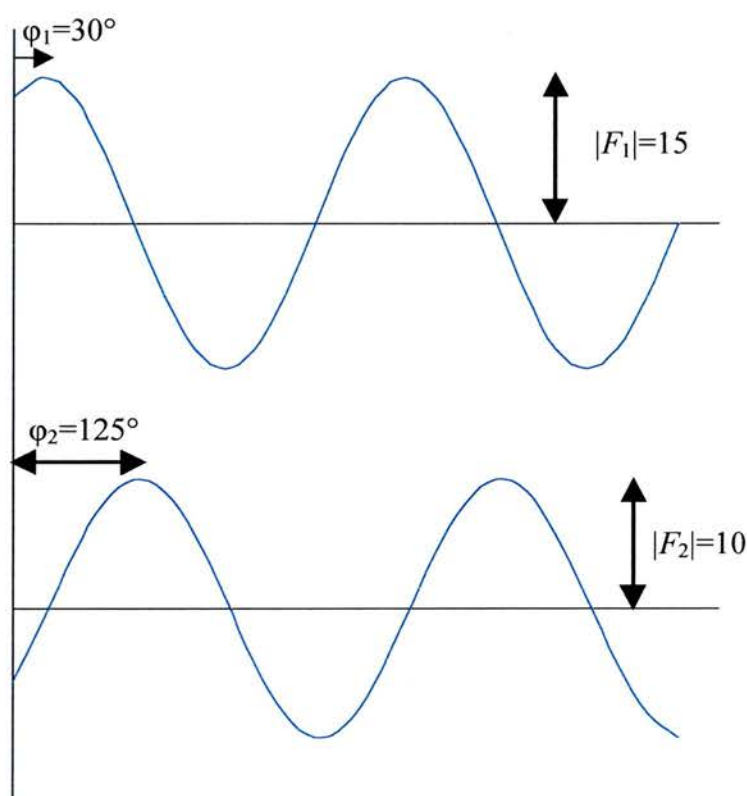


Figure 3.4 Two interacting waves with both amplitudes and phases.

(intensity of the peak). Figure 3.4 illustrates that if the interaction of two waves is to be studied the intensity and the phase must be known. Equation 4 separates the intensity and the phase, ϕ . In the diffraction pattern the amplitudes and phases are needed to obtain the structural solution. The amplitude can be measured as discussed

earlier. However, the phase is a problem because there is no way of knowing the intrinsic phases $\varphi(h,k,l)$ from the diffraction pattern.

$$\rho_{(x,y,z)} = \frac{1}{V} \sum_h \sum_k \sum_l |F_{(h,k,l)}| \exp[-2\pi \cdot i(hx + ky + lz - \varphi_{(h,k,l)})] \quad (3.4)$$

There are several ways round the phase problem by employing statistical techniques, such as direct methods, to produce a structure solution. For single crystal XRD data it is now generally routine to perform structure solutions by statistical “direct methods” to provide a starting model for the structure.⁶ Often there is not enough data using powder data to obtain a good structural model by direct methods, and so solving structures becomes very difficult, although this has become easier over the last decade or so.

Direct methods tries to derive structure factor phases directly from the observed amplitudes using mathematical relationships. As mentioned previously the amplitude and phase are two independent values. Electron density is the Fourier transform of the diffraction pattern which means a set of waves must be added together to produce the electron density. Waves have one half positive and the other negative, except the $F(000)$ which is constant and positive. However the waves must be added together to build up positive areas, since electron density is considered to always be positive ($\rho_{(x,y,z)} \geq 0$) and is located in discrete areas (atoms). There are only so many possible ways to do this and direct methods work by a trial and error to find out the highest probability. It takes the most important (intense) reflections and works out the probable relationships among their phases testing these against recognisable molecular features by calculating the Fourier transforms for the observed amplitudes

and the trial phases. This of course takes a lot of computing and results in an initial structure solution that has the best figure of merit.

Direct methods work best on all atoms being equal. When studying the structure of zeolites this is mostly the best method and is the method utilised in this thesis. However if a structure contained a heavy atom this would not be as suitable and would require to be solved by the Patterson methods, which determine the heavy atom positions from the vectors between them.

Either way this initial model is partially complete and tends only to have located a few of the atoms in the structure. A measure of how good this model is given by the residual factor (R-factor) which is defined as:

$$R = \frac{\sum ||F_{obs}| - |F_{calc}||}{\sum |F_{obs}|} \quad (3.5)$$

The better our model agrees with reality, the better $|F_{obs}|$ agrees with $|F_{calc}|$, and hence the smaller the residual becomes. However, a low value of R does not guarantee that a structure model is good as it can be artificially lowered through the addition of unjustified parameters to the model. In the refinement the total number of parameters being refined should remain substantially less than the number of observations. Variations of this definition include using F^2 instead of $|F|$ values and adding different weighting factors to give a R_w . The weighting factors multiply different reflections, based on their associated standard uncertainty (which is calculated from known statistical properties of X-rays and diffraction and is a measure of the accuracy of the measurement) and so providing information on the accuracy of the measurement when looking at R-factors.

Electron density and difference electron maps can be produced by using the reverse Fourier transform of $|F_{\text{calc}}|$ and the combination of $|F_{\text{calc}}|$ and $|F_{\text{obs}}|$ respectively. The electron density map of the model shows the atoms that are already found whereas the difference electron density map reveals remaining atoms. This provides the basis for a new improved model that can then be refined by least squares.⁷

Least squares refinement takes the model (F_{calc}) and finds values of parameters which fit the experimental data best (F_{obs}), estimates their accuracy and determines the adequacy of the model. So it takes the estimated model refines it to the data and provides an improved estimate model. This provides physical parameters such as atom types and positions, bond lengths and angles from the electron density map obtained from direct methods.

Least squares refinement is similar to fitting a 'best-fit' straight line through a set of points on a graph but is more complicated as there are more variables and the equation relating data (F_{obs}) to parameters (F_{calc}) is far from linear. However lets first consider the linear least squares where a straight line is fitted through a number of points (x_i, y_i). This line would have the equation:

$$y_i = mx_i + c \quad (3.6)$$

or

$$\varepsilon_i = y_i - mx_i - c \quad (3.7)$$

In this case the parameters are the gradient, m , and the intercept, c . The experimental measurements are the pairs of values (x_i, y_i). ε_i is known as the residual of the

equation. The definition of “best fit” is the minimisation of $\sum \epsilon_i^2$ by fitting values of m and c to give a line of linear regression. This is expressed in terms of vectors:

$$\begin{pmatrix} x_1 & 1 \\ x_2 & 1 \\ x_3 & 1 \\ \dots & 1 \\ \dots & 1 \\ x_i & 1 \end{pmatrix} \begin{pmatrix} m \\ c \end{pmatrix} = \begin{pmatrix} y_1 \\ y_2 \\ y_3 \\ \dots \\ \dots \\ y_i \end{pmatrix} \quad (3.8)$$

This can be written more concisely as

$$\mathbf{Ax} = \mathbf{b} \quad (3.9)$$

where A is the left-hand-side of the matrix containing the x values, x is the vector of unknowns m and c , and b is the right-hand-side vector of the y values. A is known as the design matrix. The least squares solution to this observational equation involves premultiplying both sides of (3.9) by the transpose of A then solving for x :

$$(\mathbf{A}^T \mathbf{A})\mathbf{x} = \mathbf{A}^T \mathbf{b} \quad (3.10)$$

These equations are known as the normal equations of least squares. In general there should be at least the same number of equations as unknowns as seen in equation 3.10. The least squares solution is defined as that which minimises the sum of the squares of the residuals of the observational equations. A generalisation for a more complex non-linear system such as a crystal would involve a least squares solution to give the minimisation of the function:

$$\sum w(F_{\text{obs}}^2 - F_{\text{calc}}^2) \quad (3.11)$$

Where F_{obs} and F_{calc} are the experimental and model structure factors respectively.

The least squares matrices for a crystal structure are very large as there have to be an excess of observational equations over unknowns. We saw earlier that weights, w , can be added to improve the accuracy of equations when we look at R-factors, this is

also the case for these observational equations. In addition restraints (these are conditions such as bond length or angle which are satisfied approximately to minimise variances) and constraints (these are the same conditions but, they must be satisfied precisely) can be added to improve the least squares solution. R-factors are provided at the end of the least squares refinement to provide a measure of accuracy.

Another measure of the accuracy of the refinement is the goodness of fit, S

$$S = \left\{ \sum w(F_{\text{obs}} - F_{\text{calc}})^2 / (N-P) \right\}^{1/2} \quad (3.12)$$

where N is the number of data and P the number of parameters. If the weights are correct, S should be close to unity.

Several structural parameters may be refined:

1. Atomic coordinates (x,y,z) – three for each atom in a general position, an atom in a special position may have one or more fixed values
2. Thermal displacement factors – Isotropic or Anisotropic. Isotropic have an equal measure of displacement value in each of the three orthogonal directions, described by U. Anisotropic models describes thermal motion in three dimensions with arbitrarily oriented axes, giving them six U values.
3. Overall scale factor – Scales the observed and calculated intensities to be the same.
4. Site Occupancies – An atom in a general position tends to have an occupancy of one, though disordered structures may be modelled by the use and refinement of non-unit occupancies.
5. Atom type – Atoms assignments must be correct, as incorrect scattering factors for the calculation of F_{calc} would result in an inaccurate refinement by affecting the other parameters (e.g. U).

3.3 Single Crystal X-ray Diffraction

Single crystal X-ray diffraction is by the far the leading technique for structural information in solid state chemistry. In principle you can learn everything there is to know about the structure as data may be obtained for the full three-dimensional lattice structure. These days single crystal diffraction data is usually collected using an area detector (see figure 3.5) as is the case at Daresbury Station 9.8 and in our in-

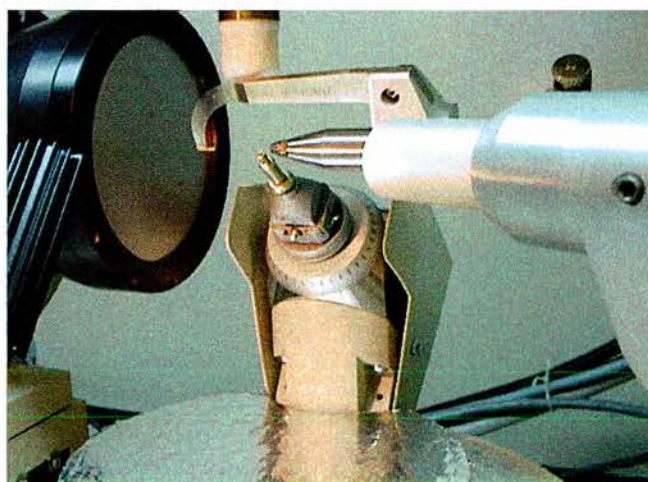


Figure 3.4 A Bruker AXS SMART CCD area detector. This was used to collect data at the CCRLC Daresbury synchrotron source.

house facilities at St Andrews University.

The area detector records the diffracted intensity information over a large area of two-dimensional space, which is then stored digitally as a 'frame' of diffracted intensity information. Many frames are collected in turn, as the crystal is rotated in a series of small steps. The frames are then analysed, and the intensity of each individual 'reflection' can be determined. The charged-coupled device (CCD) area detector has a two-dimensional array of photodiodes behind a light-sensitive phosphorus screen - when X-rays strike the screen, light is produced, the intensity of which is measured by the diodes.⁸ At Daresbury the area detector is combined with synchrotron radiation resulting in a very fast data collection and allows the study of

microcrystals. This is a very attractive quality of the synchrotron source at Daresbury (as discussed in chapter 1.4) as zeolite crystals are often difficult to grow large enough for use on laboratory diffractometers.

The advantage is that CCD detectors available to my use can collect all the data required for a full structure solution. Structure solutions by direct methods are now routinely used due to the high power of modern computers.

3.4 Powder X-ray Diffraction

Powder diffraction allows the structure determination of zeolites from crystalline powders when no large single crystals are available.¹⁰⁻¹² These powders contain many randomly oriented tiny crystals, which diffract X-rays in the same way as a single crystal. Since the crystals are randomly orientated the diffraction pattern only reveals the average of all the crystal orientations, unless of course the crystallites have a preferred orientation. So the three dimensional data from a single crystal pattern is compressed into two dimensions, which leads to peak overlap and data loss. This loss of data makes *ab initio* structure solution from powder diffraction patterns very difficult though not impossible in some cases.

In this thesis no structures are solved from powder, instead our use involved fitting a known model to the data. With a complete structural model and good starting values for background contribution, the unit-cell parameters and the profile parameters, a Rietveld refinement can begin.^{13,14} The structural parameters can be refined as discussed previously in least-squares refinement. In addition to this the profile parameters which are relevant to the powder pattern can be refined. These include the diffractometer zero point, background and peak shape. The profile parameters must be refined before the structural parameters so that the model is as near to perfect before atoms are refined to fit the data. Since powder data suffers

from an inherent loss of information, it is necessary to supplement the data with geometric information (typically bond distances and angles) by applying restraints.

In many cases powder diffraction is only used to obtain accurate lattice parameters and so a structure free (profile parameter) refinement can be carried out. For instance the Le Bail method can be used to obtain a data set similar to a single-crystal diffraction from the powder profile of the structure.

The progress of the Rietveld refinement can be followed by several figures of merit (R values) as was seen in the single crystal refinement. The weighted-profile R value, R_{wp} , is defined as

$$R_{wp} = \left\{ \frac{\sum w_i [y_i(\text{obs}) - y_i(\text{calc})]^2}{\sum w_i [y_i(\text{obs})]^2} \right\}^{1/2} \quad (3.13)$$

where $y_i(\text{obs})$ is the observed intensity at step i , $y_i(\text{calc})$ the calculated intensity, and w_i the weight. The expression in the numerator is minimised during a Rietveld refinement. The R_{wp} value can be misleading in comparing refinements, as it is highly dependent on the treatment of the background in the refinement. If the background has been subtracted, $y_i(\text{obs})$ is the net intensity after subtraction, but if the background is refined, $y_i(\text{obs})$ and $y_i(\text{calc})$ are likely to include a background contribution. So if the background is high it can automatically produce a low R_{wp} . Ideally, the final R_{wp} should approach the statistically expected R value, R_{exp} :

$$R_{exp} = \sqrt{\left\{ (N - P) / \sum_i^N w_i y_i(\text{obs})^2 \right\}} \quad (3.14)$$

where N is the number of observed (data) points and P the number of refined parameters. R_{exp} reflects the quality of the data. The approach of the two R factors is monitored by the goodness of fit

$$\chi^2 = R_{wp} / R_{exp} \quad (3.15)$$

which should approach unity as the refinement is completed.

Large values or unusually small values of χ^2 can be caused by poor data collection. It is extremely important to obtain a data set with high resolution to lessen the problem of peak overlap. Using synchrotron radiation optimises powder data by reducing peak overlap.

Examining a plot of the profile fit can also be used to monitor the refinements (see figure 3.5). This plots the observed and calculated profiles and their difference plot. It greatly aids refinement of the peak shapes. The profile plots can be much more informative than the R values when following refinements. In addition progress can be followed by checking the nature of the parameter shifts (i.e. shift/e.s.d.; are the shifts oscillating, diverging or converging?).

Powder XRD data were collected on the STOE stadip diffractometer, in which the samples are loaded in capillaries that are rotated. The diffracted beams are collected by Debye-Scherrer method.

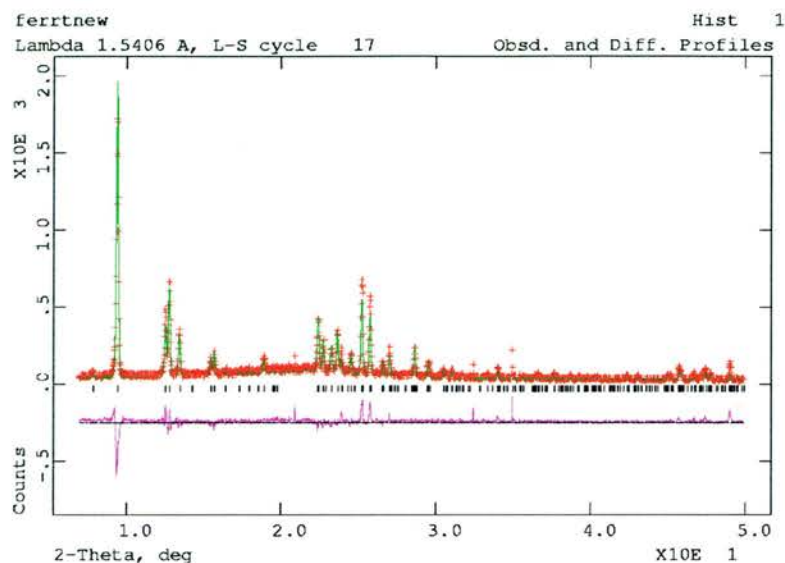


Figure 3.5 A profile fit of siliceous ferrierite. The observed data is shown in red, the calculated pattern in green and the difference plot is shown in purple.

3.5 Variable Temperature X-ray Diffraction

A great number of structural zeolite experiments benefit from variable temperature studies.¹⁵⁻¹⁸ For instance, low temperature XRD allows the solution of disordered structures as thermal motion is minimised.¹⁹ In addition the ability to collect data over a wide range of temperatures allows the study of physical properties such as negative thermal expansion and phase transitions.^{20,21}

Variable temperature single-crystal X-ray diffraction studies were carried out at the CCLRC Synchrotron Radiation Source, Daresbury, which allowed data collection within the temperature range of 30 to 623 K. The low-temperature data (30-90K) were collected using an Oxford Cryosystems Helix liquid helium cryostream. The data collected between 100 and 350 K were collected in a stream of N₂ from an Oxford Cryosystems liquid nitrogen cryostream, and the high-temperature data (350-623 K) were collected using a thermostream hot air heater.

Variable temperature powder X-ray diffraction studies were carried out in-house which allowed data collection within the temperature range of 150 to 623 K. The low-temperature data (150-350 K) were collected using an Oxford Cryosystems Helix liquid nitrogen cryostream. The high-temperature data (350-623 K) were collected using the STOE cylindrical heating element.

Problems of icing of the crystal during the low-temperature data collections were minimised by controlling the airflow into the system. However, high temperature data collections had problems due to the copper crystal holder expanding with heat and having more thermal motion. The data was of less accuracy due to the movement of the crystal.

3.6 Nuclear Magnetic Resonance Spectroscopy

Many chemists associate nuclear magnetic resonance (NMR) spectroscopy with the liquid state, since a majority of organic, inorganic and biochemical materials are characterised by NMR spectra of neat liquids or dilute samples in an appropriate solvent. NMR spectroscopy is one of the most important and versatile techniques for characterising the structure and dynamics of molecules.²² It allows the organic chemist to probe the environment of nuclei with spin $\frac{1}{2}$. An NMR spectrum reveals the chemical shift (peak position) which provides information about the environment of the nucleus from the amount of “chemical shielding” it gains from surrounding electrons. The multiplicity of the lines shows the number of neighbouring spin $\frac{1}{2}$ nuclei with respect to the central peak. In order to simplify certain spectra the technique of decoupling is used to remove this splitting. For instance to remove the C-H coupling in ^{13}C NMR spectra. The distances between the lines of a multiplet

provide the “coupling constants” which can be used to calculate geometric information.

The inorganic chemist utilises solid state NMR to yield important information concerning crystallographic details, local symmetry and environment, and connecting XRD with NMR data. NMR spectra of solid samples are more complex, since isotropic averaging of NMR interactions does not generally occur in the solid state. Instead, motion is relatively restricted in solids, such that the orientation-dependent, anisotropic characteristics of NMR interactions are apparent in the spectra. NMR interactions vary in magnitude depending on their orientation with respect to the applied magnetic field. Because of a multitude of orientation-dependent interactions, the solid-state NMR spectra of polycrystalline powder samples are generally quite broad, and often appear to have very little definition. “Magic angle spinning” (MAS) reduces the line broadening by setting the local magnetic field in the sample to zero. The local field is defined by the equation:

$$B_{loc} = \pm \mu_y r_{xy}^{-3} (3 \cos^2 \theta_{xy} - 1) \quad (3.16)$$

The satellite transitions are removed by rapidly spinning the sample at a speed of the order of the static line width (typically of the order of 6000 – 10000 Hz) and tilting at an angle, θ_{xy} , of $54^\circ 44'$, the so-called magic angle. The $(3 \cos^2 \theta - 1)$ term becomes zero, and the remaining part of the expression is the isotropic chemical shift as would be seen in solution. Also the use of high-power proton decoupling methods is used to reduce dipole-dipole interactions. Combining these methods produces solid state NMR spectra of high resolution. Solid state NMR has been used to examine several zeolite systems.

^{31}P , ^{13}C NMR were collected by the EPSRC solid state NMR service at Durham University.

3.7 Thermal Analysis

Thermogravimetry is used to examine the stability, route of decomposition and structure of microporous materials.^{23,24} The basic technique involves weighing a sample while it is being heated to record weight loss. However mass spectroscopy can be applied to thermal analysis (TG-MS) to provide a more detailed picture of what is occurring.

TG-MS of zeolites is generally used to yield information on the loss of constituent or sorbed water, decomposition reactions of the organic template and the degradation of frameworks to the metal oxide.²⁵

Differential scanning calorimetry (DSC) is used to study thermal transitions such as phase changes.²⁶ A sample of known weight and a reference are heated at a specified rate (usually around 10 °C per minute). This technique insures that both the sample and reference pan are heated at exactly the same rate. Since the pans are different (i.e. one contains material and the other is empty) the heater has to work harder to heat the sample pan and DSC measures this difference. Heat capacities and the transition temperature are recorded on a Perkin-Elmer DSC7 DSC.

3.8 Other techniques

3.8.1 Microanalysis

C, H, N Microanalysis can provide interesting data on the amount of organic template molecule present in the microporous material. Microanalysis was carried out with a Carlo Erba model 1106 elemental analyser.

3.8.2 Test for second harmonic generation (SHG)

In order to observe a second-order nonlinear effect in crystals, the material must pack in a non-centrosymmetric space group. This can be tested using the Kurtz and Perry powder method.²⁷ A powdered zeolite sample should double the frequency of a laser if it demonstrates SHG.¹⁸ A Nd:YAG laser was used in the Physics Department, St Andrews University. In this case the infrared radiation of the laser should double in frequency to produce a green light if the material exhibits SHG.

3.9 References

1. R. M. Szostak, *Molecular Sieves, Principles of Synthesis and Identification*, Van Nostrand Rienhold, New York, 1989, Ch. 1.
2. R. H. Jones, J.M. Thomas, J. Chen, R. Xu, Q. Huo, S. Li, Z. Ma, and A.M. Chippindale, *J. Solid State Chem.*, 1993, **102**, 204.
3. S.T. Wilson in *Verified Synthesis of Zeolitic Materials*, H. Robson and K.P. Lillerud, Elsevier, Amsterdam, 2001, 27.
4. A.K. Cheetham in *Solid State Chemistry Techniques*, A.K. Cheetham and P. Day, Oxford University Press, Oxford, 1988, Ch. 2.
5. A. Guinier, *X-ray Diffraction*, Freeman, San Francisco, 1963, 121.

6. M.M. Woolfson, *Direct Methods in Crystallography*, Oxford University Press, Oxford, 1961.
7. D. Viterbo in *Fundamentals of Crystallography*, C. Giacovazzo, Oxford University Press, Oxford, 1992, Ch. 5.
8. A.M.Z. Slawin, *Chem. Brit.*, 1998, **34**, 31.
9. H.L. Monaco in *Fundamentals of Crystallography*, C. Giacovazzo, Oxford University Press, Oxford, 1992, Ch. 4.
10. H. P. Klug and L.E. Alexander, *X-ray Diffraction Procedures for Polycrystalline and Amorphous Materials*, John Wiley and Sons, New York, 1974
11. A.K. Cheetham and J.C. Taylor, *J. Solid State Chem.*, 1977, **21**, 253.
12. L.B. McCusker, *Acta Crystallogr. Sect. A*, 1991, **47**, 297.
13. H.M. Rietveld, *J. Appl. Cryst.*, 1969, **2**, 65.
14. L.B. McCusker, R.B. Von Dreele, D.E. Cox, D. Louër and P. Scardi, *J. Appl. Cryst.*, 1999, **32**, 36.
15. D.A. Woodcock and P. Lightfoot, *Chem. Mater.*, 1999, **11**, 2508.
16. J.M. Newsam, C.Z. Yang, H.E. King, R.H. Jones and D. Xie, *J. Phys. Chem. Solids*, 1991, **52**, 1281.
17. B.B. Iversen, A. Darovsky, R. Bolotovskiy and P. Coppens, *Acta Crystallogr. Sect. B – Struct. Sci.*, 1998, **54**, 174.
18. I. Bull, L.A. Villaescusa, S. J. Teat, M.A. Camblor, P.A. Wright, P. Lightfoot and R.E. Morris, *J. Am. Chem. Soc.*, 2000, **122**, 7128.
19. S.J. Andrews and A.J. Welch, 1984, **88**, 153.
20. L.A. Villaescusa, P. Lightfoot, S.J. Teat and R.E. Morris, *J. Am. Chem. Soc.*, 2001, **123**, 5453.
21. B. F. Mantzen and M. Sacerdote-Peronnet, *Zeolites*, 1993, **28**, 1017.

22. D.M. Grant and R.K. Harris, *Encyclopaedia of Nuclear Magnetic Resonance Spectroscopy*, John Wiley and Sons, New York, 1996.
23. S. Oliver, A. Kupermann, A. Lough and G.A. Ozin, *J. Mater. Chem.*, 1997, **7**, 807.
24. P.R. Slater and C. Greaves, *Physica C*, 1991, **175**, 172.
25. R.C. MacKenzie, *Differential Thermal Analysis*, R.C. MacKenzie, Academic Press, Oxford, 1970.
26. G.W.H. Höhne, *Differential Scanning Calorimetry: an Introduction for Practitioners*, Springer-Verlag, New York, 1996.
27. S.K. Kurtz and T.T. Perry, *J. Appl. Phys.*, 1968, **39**, 3798

Chapter 4 – Ferrierite

4.1 Introduction

Ferrierite is a zeolitic material discovered by Walter Frederick Ferrier (1865-1950) at mineral mines in Canada. It is well known in nature and also now as a synthetic material.¹ Although it can contain stacking faults,² an understanding of the structure and properties remain important due to its role as a catalyst in many commercial reactions. For example it is important in the petrochemical industry where it acts as a shape-selective catalyst for the production of isobutene. This used to be used as a feedstock in the synthesis of methyl tert-butyl ether (MTBE), an oxygenate additive in unleaded motor fuel,³ although MTBE is not used anymore for environmental reasons. Ferrierite also has applications in radioactive waste disposal and adsorption of alkanes.

Siliceous ferrierite can be readily synthesised by both aqueous⁴ and non-aqueous routes.⁵ The structure of both the as-made and calcined material have been solved using synchrotron X-ray and neutron diffraction. Ferrierite was first solved by Vaughan⁶ in the 1960s from a magnesium-containing mineral sample from Canada and this was confirmed in other work.^{2,7} The crystal structure of ferrierite (see figure 4.1) is built up of 5 membered ring (MR) building units, stacked in the direction of the *c*-axis. These form a matrix of 10MR channels running parallel to the *c*-axis, which are intersected by 8MR channels running parallel to the *b*-axis. Six MR connect the 10MR along the *c*-axis direction. Instead of thinking of this structure in terms of its channels it can also be described as a layered structure. The meandering layers are made of the 5 MR building units running parallel to one another in the *a*-

axis and c -axis directions. A single SiOSi bridging bond at the end of each of the main channels connects these.

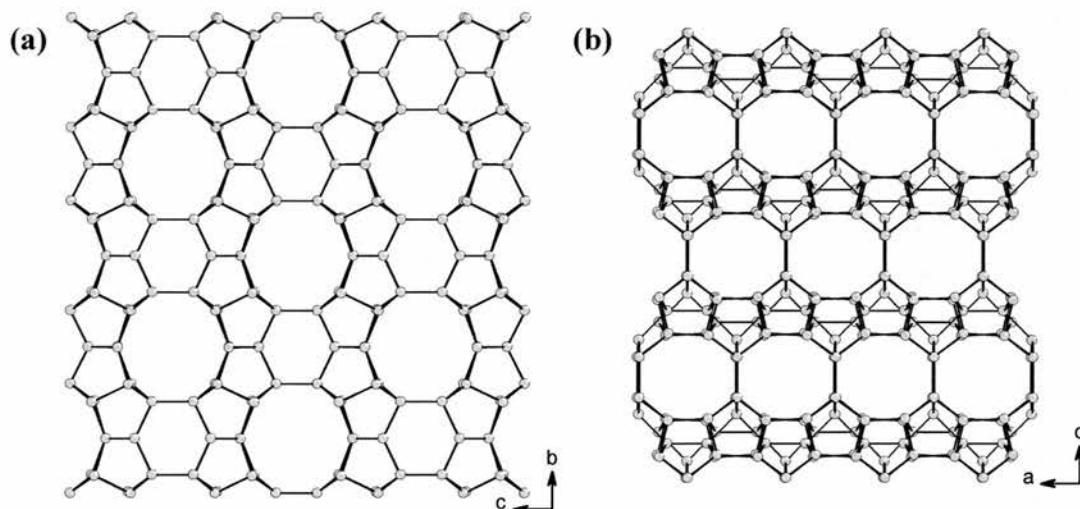


Figure 4.1 Framework topology of ferrierite - the silicons are shown in grey. (a) Shows the rows of 10 MR channels joined by 6 MRs viewed down the a -axis. (b) Shows the 8 MR channels viewed down the b -axis.

Siliceous ferrierite was first solved in 1993 by Kuperman et al. in space group, $Immm$.⁵ A few years later Morris et al., collected powder xrd data at the National Synchrotron Source, Brookhaven National Laboratory and an improved refinement yielded the correct space group $Pnmm$.⁸ At first glance there is not too much difference in the topological framework when comparing the two different symmetries. However, on closer examination of the structure and its behaviour these differences become important. This underlines the advantages of synchrotron radiation once again. In 1996 Davis et al., went one stage further and obtained a single crystal structure which solved in $Pnmm$ and they also managed to locate the pyridine molecules which were acting as structure directing agents.⁹ However many crystallographic attempts at locating fluoride within the framework have been unsuccessful. Here I report the location of fluoride and the synthetic reasoning behind its incorporation into the framework.

Porous structures tend to have properties that are dependent on temperature, so that the pores expand or contract with heating. Many zeolites and AlPO_4s exhibit negative thermal expansion behaviour (NTE).^{10,11,12} These have potential applications in composite materials with tailored thermal expansion (e.g. dental fillings). In addition these zeolite frameworks can undergo phase transitions with temperature as seen in Cristobalite by Dove et al.^{13,14} A crystallographic study of an MFI-type zeolite by Yamahara et al.,¹⁵ showed two distinct phase transitions with temperature and a change in thermal behaviour with phase. NMR and calorimetric studies of the same MFI materials by Letoffe et al agreed with the crystallographic paper.¹⁶ In addition some materials undergo phase transitions with temperature for example Cristobalite. Ferrierite demonstrates both of these behaviours and these will be examined closely in this chapter.

4.2 Experimental

4.2.1 Hydrothermal Synthesis

6.08 g of TEOS (tetraethyl orthosilicate) was hydrolysed in 52.84 g of an aqueous solution of N,N-dimethyl-6-azonium-1,3,3-trimethylbicyclo(3.2.1)octane hydroxide (DMABO-ol). 2.76 mol of template per gram of solution was used. The solution was reduced to a gel by evaporating 4.37g of ethanol and 48.42g of water. 0.61g of HF was added drop-wise while stirring. The resultant paste was transferred to the polytetrafluoroethylene lined acid digestion bomb (23ml, Parr) and 1.84g of pyridine (Pyr) was added. The reaction ratios used were 0.5 DMABO-ol: 0.5 HF: 1.5 H_2O : SiO_2 : 0.8 Pyr. This reaction was carried out under static conditions at 423 K for 38 days. It was then removed from the furnace and quenched. The ferrierite was then washed with deionised water and dried at 353 K. The products contained small

crystals (approximately $50\mu\text{m} \times 50\mu\text{m} \times 10\mu\text{m}$) that were suitable for microcrystal X-ray diffraction studies.

4.2.2 Calcination of ferrierite

Calcination of as-made ferrierite in flowing oxygen at $850\text{ }^\circ\text{C}$ (heating rate 10°min^{-1}) for 10 hours resulted in a crystalline product which was light grey in colour.

4.2.3 Powder X-ray diffraction

Powder x-ray diffraction patterns were collected over the temperature range 100 to 904 K were obtained on a STOE STADIP diffractometer operating on monochromated $\text{Cu K}\alpha_1$. The low temperature data (100 to 300K) were collected using an Oxford Helix liquid nitrogen cryostream and the high temperature data (350 to 904 K) were collected using a STOE cylindrical graphite heating element.

4.2.4 Single Crystal Diffraction

Single crystal X-ray diffraction experiments were then carried out at the CCLRC Synchrotron Radiation Source, Daresbury Laboratory, UK using a Bruker AXS SMART CCD area detector diffractometer on the high flux microcrystal-diffraction facility (station 9.8) of the SRS at Daresbury. The as-made ferrierite was collected using an X-ray wavelength 0.6942 \AA selected by a horizontally focussing silicon (111) monochromator and vertically focussed by a cylindrically bent palladium-coated zerodur mirror. The data sets of calcined ferrierite were collected using an X-ray wavelength of 0.6892 \AA (the experimental details will be given for each experiment within the results and discussion). Corrections were made for the

synchrotron beam intensity decay as part of the standard inter-frame scaling procedures.

4.2.5 Solid State NMR

MAS NMR experiments were carried out on the as-made ferrierite using the EPSRC Solid-State NMR Service (Durham) on a Varian Unityplus 200 MHz spectrometer. The ^{19}F NMR spectra were collected using the following conditions: contact time 1 ms, acquisition time 10 ms, relaxation time of 30 s and a spinning rate 11.44 kHz.

The ^{29}Si NMR spectra of calcined ferrierite were collected on a Bruker DSX 400 (CRMHT Orleans, with Dominique Massiot and Pierre Florian) by Dr Lucy Bull using a 4mm Bruker MAS probe. The sample was spun at 4 kHz and data were collected using a 90° pulse length of $3.5\ \mu\text{s}$ and a relaxation delay of 30 s. Typically thirty two scans were acquired. The spectra are referenced to TMS at 0 ppm. Temperatures were calibrated using the ^{207}Pb temperature dependent NMR shift of $\text{Pb}(\text{NO}_3)_3$. The samples were left for 20 minutes at each temperature in order to reach temperature equilibrium before the ^{29}Si or ^{207}Pb spectra were collected.

4.2.6 DSC

The enthalpy and temperature changes were determined using a Perkin-Elmer DSC7 differential scanning calorimeter (DSC). Data was collected for heating and cooling runs in the temperature range of 123 to 573 K.

4.3 Results and Discussion

4.3.1 Structure of As-made Ferrierite

The structure of as-made ferrierite (PyrF-Si-Fer) was solved by direct methods (SHELXS-97) and refined with full-matrix least-squares technique (SHELXL-97).¹⁷ The final unit cell refined to $a=7.4653(3)$ Å, $b=14.1570(5)$ Å and $c=18.8199(3)$ Å in space group Pnmm to give an R-factor of 5.97 % at 150K. Full details of the data collection and refinement parameters are given in table 4.1. Full details of the structure determination can be found on the attached CD as Crystallographic Information Files. Full atomic coordinates, bond lengths and angles and thermal displacement parameters are given in tables 4.3 to 4.5.

Table 4.1 Crystal data and structure refinement for as-made ferrierite.

Identification code	PyrF-SiFer	
Empirical formula	$C_{20}H_{66}F_4N_4O_{72}Si_{36}$	
Formula weight	2602.01g	
Temperature	150(2) K	
Wavelength	0.69420 Å	
Crystal system	orthorhombic	
Space group	Pnmm	
Unit cell dimensions	$a = 7.4653(3)$ Å	$\alpha = 90^\circ$.
	$b = 14.1570(5)$ Å	$\beta = 90^\circ$.
	$c = 18.8199(3)$ Å	$\gamma = 90^\circ$.
Volume	$1989.00(11)$ Å ³	
Z	1	
Density (calculated)	2.172 Mg/m ³	
Absorption coefficient	0.707 mm ⁻¹	
F(000)	1330	
Crystal size	$0.15 \times 0.05 \times 0.01$ mm ³	
Theta range for data collection	1.76 to 29.40°.	
Index ranges	$-10 \leq h \leq 9$, $-16 \leq k \leq 19$, $-25 \leq l \leq 25$	
Reflections collected	13058	

Independent reflections	2845 [R(int) = 0.0475]
Completeness to theta = 29.40°	93.7 %
Max. and min. transmission	0.9965 and 0.9930
Refinement method	Full-matrix least-squares on F ²
Data / restraints / parameters	2845 / 0 / 162
Goodness-of-fit on F ²	1.273
Final R indices [I>2sigma(I)]	R1 = 0.0597, wR2 = 0.1682
R indices (all data)	R1 = 0.0750, wR2 = 0.1742
Largest diff. peak and hole	0.991 and -0.684 e.Å ⁻³

Table 4.2 Atomic coordinates and equivalent isotropic displacement parameters (Å²) for PyrF-Si-Fer. U(eq) is defined as one third of the trace of the orthogonalized U_{ij} tensor.

	x	y	z	U(eq)
Si(1)	0.0000	0.5000	0.3463(1)	0.011(1)
Si(2)	-0.081(1)	0.7003(1)	0.4164(1)	0.012(1)
Si(3)	-0.2070(1)	0.9992(1)	0.2736(1)	0.011(1)
Si(4)	-0.7159(1)	0.8007(1)	0.3291(1)	0.012(1)
Si(5)	-0.3042(1)	0.7949(1)	0.3200(1)	0.012(1)
O(1)	-0.2518(4)	0.9052(2)	0.3176(1)	0.027(1)
O(2)	0.0000	1.0000	0.2497(2)	0.022(1)
O(3)	-0.1809(3)	0.7439(2)	0.3775(1)	0.028(1)
O(4)	-0.5088(3)	0.7806(2)	0.3460(1)	0.022(1)
O(5)	0.120(3)	0.5911(2)	0.3967(2)	0.030(1)
O(6)	-0.2473(3)	1.0876(2)	0.3254(1)	0.023(1)
O(7)	-0.7776(4)	0.7514(2)	0.2567(1)	0.037(1)
O(8)	-0.0325(5)	0.7120(3)	0.5000	0.025(1)
O(9)	0.1752(4)	0.4937(2)	0.2975(1)	0.033(1)
O(10)	0.1689(3)	0.7573(2)	0.3939(1)	0.025(1)
C(1)	-0.5032(9)	0.5980(7)	0.5000	0.054(2)
C(2)	0.0012(7)	1.0497(5)	0.628(3)	0.057(1)
C(3)	-0.3190(30)	0.9971(17)	0.5000	0.108(5)
C(4)	-0.4020(30)	1.0787(11)	0.5000	0.102(5)
C(5)	-0.4070(30)	0.9180(14)	0.5000	0.130(6)
F(1)	-0.9880(40)	0.6650(30)	0.2620(20)	0.358(18)

Table 4.3 Bond lengths [\AA] and angles [$^\circ$] for PyrF-Si-Fer.

Si(1)-O(9)#1	1.601(3)	O(8)-Si(2)-O(5)	109.91(17)
Si(1)-O(9)	1.601(3)	O(8)-Si(2)-O(10)	107.60(16)
Si(1)-O(5)	1.603(2)	O(5)-Si(2)-O(10)	110.36(14)
Si(1)-O(5)#1	1.603(2)	O(8)-Si(2)-O(3)	108.55(16)
Si(2)-O(8)	1.5929(9)	O(5)-Si(2)-O(3)	109.99(14)
Si(2)-O(5)	1.597(3)	O(10)-Si(2)-O(3)	110.38(14)
Si(2)-O(10)	1.605(2)	O(1)-Si(3)-O(9)#2	111.57(14)
Si(2)-O(3)	1.606(2)	O(1)-Si(3)-O(2)	110.53(12)
Si(3)-O(1)	1.602(2)	O(9)#2-Si(3)-O(2)	107.00(16)
Si(3)-O(9)#2	1.604(3)	O(1)-Si(3)-O(6)	107.04(14)
Si(3)-O(2)	1.6094(12)	O(9)#2-Si(3)-O(6)	110.69(14)
Si(3)-O(6)	1.615(2)	O(2)-Si(3)-O(6)	110.03(12)
Si(4)-O(7)	1.598(2)	O(7)-Si(4)-O(4)	111.68(15)
Si(4)-O(4)	1.604(2)	O(7)-Si(4)-O(6)#3	110.14(13)
Si(4)-O(6)#3	1.606(2)	O(4)-Si(4)-O(6)#3	110.39(14)
Si(4)-O(10)#4	1.615(2)	O(7)-Si(4)-O(10)#4	108.91(15)
Si(5)-O(3)	1.593(2)	O(4)-Si(4)-O(10)#4	107.19(13)
Si(5)-O(7)#5	1.598(2)	O(6)#3-Si(4)-O(10)#4	108.41(13)
Si(5)-O(1)	1.611(2)	O(3)-Si(5)-O(7)#5	110.90(15)
Si(5)-O(4)	1.616(2)	O(3)-Si(5)-O(1)	108.57(14)
Si(5)-F(1)#5	2.14(4)	O(7)#5-Si(5)-O(1)	109.93(13)
O(2)-Si(3)#6	1.6094(12)	O(3)-Si(5)-O(4)	106.52(13)
O(6)-Si(4)#3	1.606(2)	O(7)#5-Si(5)-O(4)	109.82(14)
O(7)-Si(5)#2	1.598(2)	O(1)-Si(5)-O(4)	111.05(14)
O(8)-Si(2)#7	1.5929(9)	O(3)-Si(5)-F(1)#5	168.6(11)
O(9)-Si(3)#5	1.604(3)	O(7)#5-Si(5)-F(1)#5	62.6(11)
O(10)-Si(4)#8	1.615(2)	O(1)-Si(5)-F(1)#5	82.8(10)
C(1)-C(2)#9	1.366(7)	O(4)-Si(5)-F(1)#5	69.2(9)
C(1)-C(2)#10	1.366(7)	Si(3)-O(1)-Si(5)	150.59(17)
C(2)-C(1)#11	1.366(7)	Si(3)-O(2)-Si(3)#6	147.5(2)
C(2)-C(2)#6	1.407(13)	Si(5)-O(3)-Si(2)	161.29(18)
C(3)-C(5)	1.30(2)	Si(4)-O(4)-Si(5)	145.97(17)
C(3)-C(4)	1.31(2)	Si(2)-O(5)-Si(1)	155.6(2)
C(4)-C(5)#12	1.43(3)	Si(4)#3-O(6)-Si(3)	145.13(16)
C(5)-C(4)#12	1.43(3)	Si(4)-O(7)-Si(5)#2	170.0(2)
F(1)-Si(5)#2	2.14(4)	Si(2)-O(8)-Si(2)#7	162.3(3)
O(9)#1-Si(1)-O(9)	110.0(2)	Si(1)-O(9)-Si(3)#5	157.4(2)

O(9)#1-Si(1)-O(5)	109.89(13)	Si(2)-O(10)-Si(4)#8	146.00(17)
O(9)-Si(1)-O(5)	109.77(14)	C(2)#9-C(1)-C(2)#10	119.9(8)
O(9)#1-Si(1)-O(5)#1	109.77(14)	C(1)#11-C(2)-C(2)#6	120.0(4)
O(9)-Si(1)-O(5)#1	109.89(13)	C(5)-C(3)-C(4)	121.5(19)
O(5)-Si(1)-O(5)#1	107.5(2)	C(3)-C(4)-C(5)#12	120.0(13)
		C(3)-C(5)-C(4)#12	118.5(16)

Symmetry transformations used to generate equivalent atoms:

#1 -x,-y+1,z #2 x-1/2,-y+3/2,-z+1/2 #3 -x-1,-y+2,z
 #4 x-1,y,z #5 x+1/2,-y+3/2,-z+1/2 #6 -x,-y+2,z
 #7 x,y,-z+1 #8 x+1,y,z #9 -x-1/2,y-1/2,-z+1/2
 #10 -x-1/2,y-1/2,z+1/2 #11 -x-1/2,y+1/2,z-1/2
 #12 -x-1,-y+2,-z+1

Table 4.4 Anisotropic displacement parameters (\AA^2) for PyrF-Si-Fer. The anisotropic displacement factor exponent takes the form: $-2\pi^2 [h^2 a^{*2} U_{11} + \dots + 2 h k$

	$a^* b^* U_{12}]$					
	U_{11}	U_{22}	U_{33}	U_{23}	U_{13}	U_{12}
Si(1)	0.008(1)	0.012(1)	0.011(1)	0.000	0.000	0.000(1)
Si(2)	0.010(1)	0.012(1)	0.012(1)	0.000(1)	0.000(1)	-0.001(1)
Si(3)	0.007(1)	0.013(1)	0.015(1)	-0.001(1)	0.000(1)	0.000(1)
Si(4)	0.008(1)	0.012(1)	0.015(1)	0.000(1)	-0.001(1)	0.001(1)
Si(5)	0.008(1)	0.011(1)	0.015(1)	0.000(1)	0.002(1)	0.000(1)
O(1)	0.038(1)	0.015(1)	0.029(1)	0.001(1)	0.008(1)	-0.006(1)
O(2)	0.007(1)	0.038(2)	0.020(2)	0.000	0.000	0.002(1)
O(3)	0.016(1)	0.039(1)	0.030(1)	0.012(1)	-0.006(1)	0.003(1)
O(4)	0.007(1)	0.030(1)	0.030(1)	0.006(1)	0.002(1)	0.002(1)
O(5)	0.044(2)	0.017(1)	0.028(1)	-0.008(1)	-0.002(1)	-0.002(1)
O(6)	0.031(1)	0.013(1)	0.024(1)	-0.001(1)	0.004(1)	0.003(1)
O(7)	0.045(2)	0.040(2)	0.027(1)	-0.015(1)	-0.013(1)	0.008(1)
O(8)	0.035(2)	0.030(2)	0.010(1)	0.000	0.000	0.000(1)
O(9)	0.016(1)	0.061(2)	0.022(1)	0.001(1)	0.009(1)	0.004(1)
O(10)	0.013(1)	0.032(1)	0.029(1)	0.009(1)	0.005(1)	-0.006(1)
C(1)	0.061(5)	0.061(5)	0.040(3)	0.000	0.000	0.003(3)
C(2)	0.065(4)	0.066(3)	0.040(3)	-0.012(2)	-0.001(2)	0.001(3)
C(3)	0.129(13)	0.153(16)	0.042(5)	0.000	0.000	-0.005(11)
C(4)	0.174(15)	0.110(10)	0.023(3)	0.000	0.000	-0.052(10)
C(5)	0.200(20)	0.161(16)	0.028(4)	0.000	0.000	-0.010(15)

The structure determination of PyrF-SiFer led to typical FER topology for the framework with five crystallographic nonequivalent Si atoms and ten oxygens in the asymmetric unit (as shown in table 4.2). The Si-O distances and angles are in the normal ranges for silica zeolites: Si-O distances of 1.593(1) to 1.615(1) Å and O-Si-O angles of 107.19(13) to 111.05(14) °. Two crystallographically distinct pyridine (Pyr1 and Pyr2) molecules are occluded in the framework as previously reported by Lewis et al. (see figure 4.2).⁹ Pyr1 occupies the [8²6²6⁴5⁸] cage, namely, the ferrierite cage. It lies along the intersection of the 6 MR and 8 MR channels as shown in figure 4.3a. Pyr2 is located at the intersection of the 10 MR and 8 MR as shown in figure 4.3b. In other words the 8 MR channels contain both pyridine molecules in an alternating sequence with their planes perpendicular to one another, while the 10 MR channel contains only one type of pyridine (pyr2) parallel to one another. The location of the nitrogen on the pyridine molecule proved impossible due to the disorder present caused by the presence of an inversion centre -1 found in the 6-rings or the pyridine might be six-fold disordered.

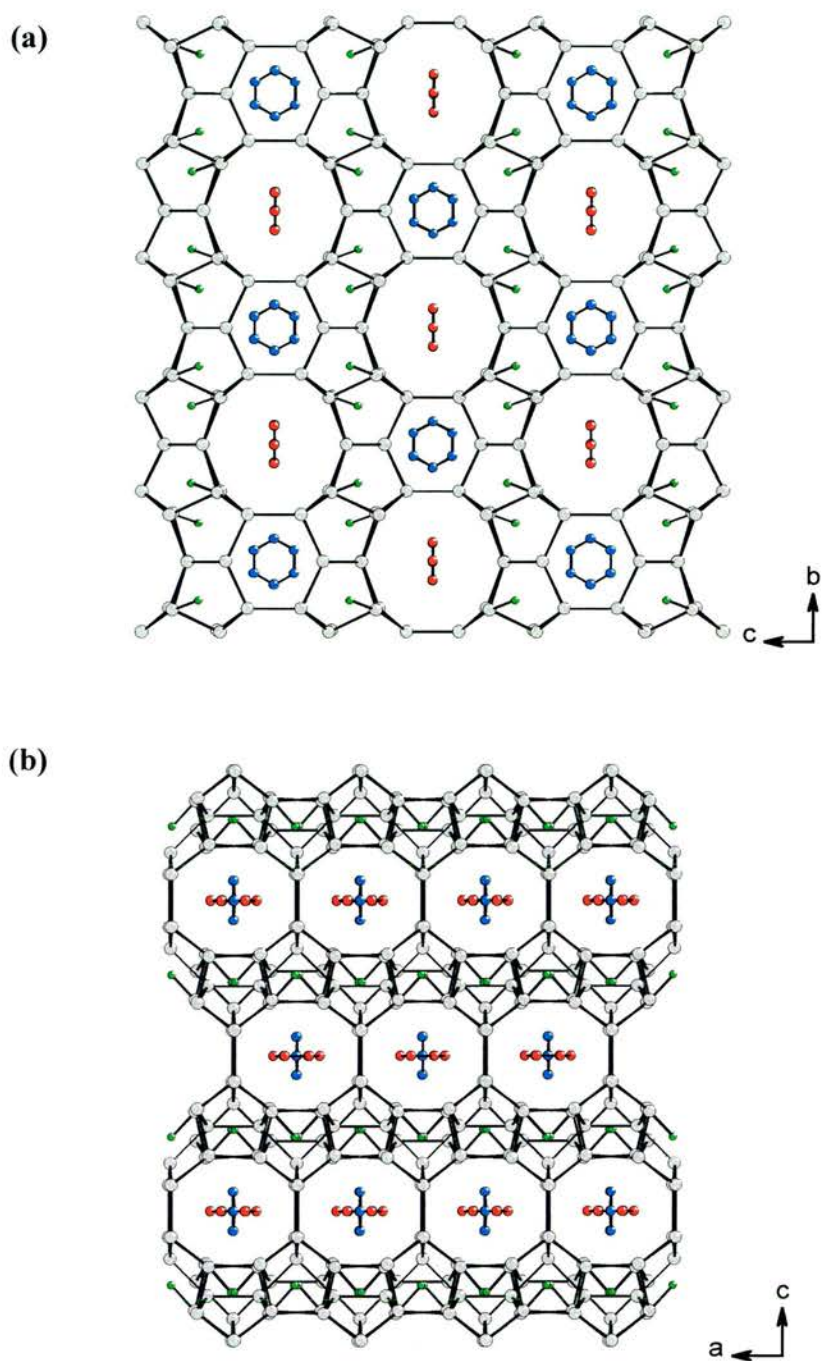


Figure 4.2 Single-crystal structure of as-synthesised Si-FER shows the positioning of the two crystallographically different pyridine guest molecules (designated as py1 (blue) and py2 (red)) and the fluorine location in the framework. Oxygen has been removed for clarity (a) Shows py1 lying parallel to the 6-ring channel and py2 lying perpendicular to the 10 MR channel as viewed down the *a*-axis. (b) Shows py1 and py2, perpendicular to one another, within the 8MR channel as viewed down the *b*-axis.

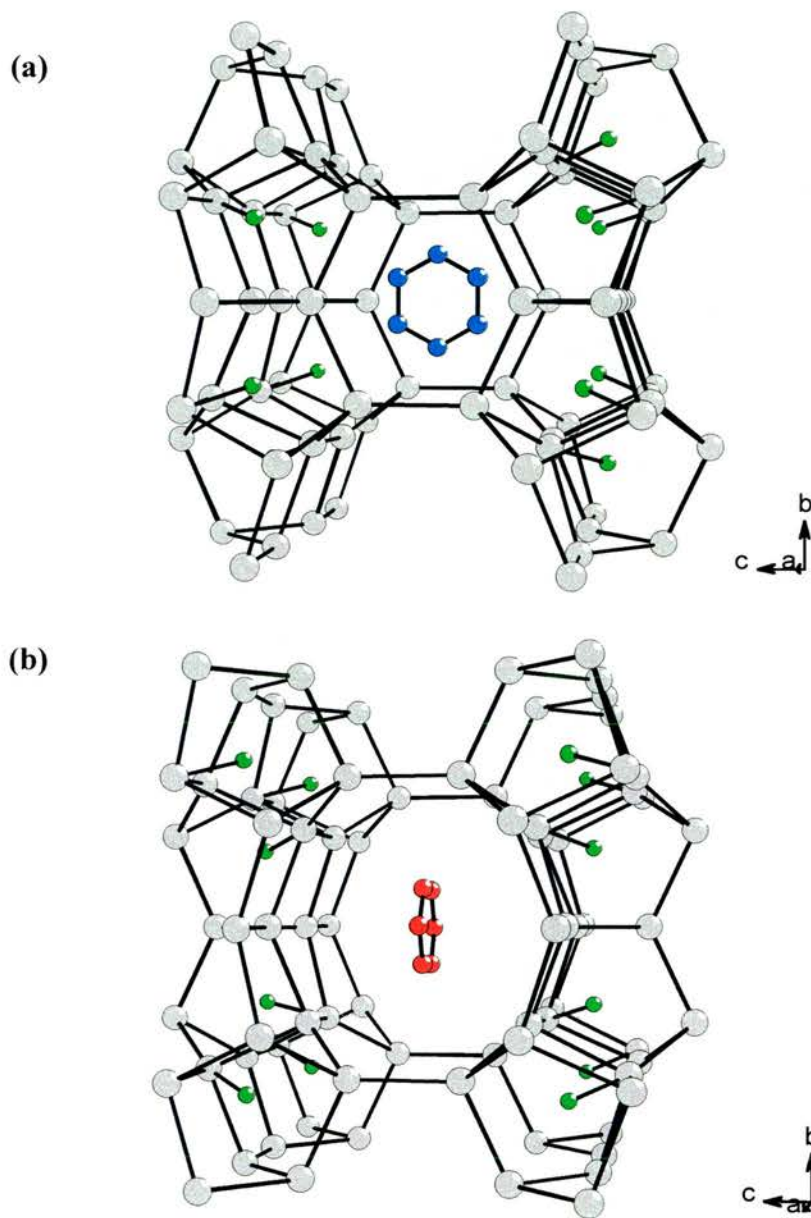


Figure 4.3 Details of the crystal structure of the organic-occupied cages. Oxygen has been removed for clarity. (a) Shows py1 occupying the $[8^2 6^2 4^5 8]$ cage and the charge balancing fluorine (green) within the 5^4 cages. (b) Shows py2 (red) lying in the intersection of the 8 and 10 MR channels.

The synthetic method of Lewis et al. used 1-amino-*n*-propane as a pH modifier and this was located within the framework.⁹ They reported no presence of framework fluorine and instead suggested substitution of aluminium (present as impurities within the starting materials) for silicon to account for the negative charge needed to balance the charge of the organics. In addition it is believed that 1-amino-*n*-propane reacts with HF to form a salt and so removes the possibility of fluorine entering the framework. However, our synthetic method did not contain any 1-amino-*n*-propane and so did not contain any of these complications. As a consequence the reaction was carried out at a more acidic pH where pyridine would be present as C₅NH₆⁺ which would need charge balancing by a negative species. Here we report the presence of fluoride within the 5⁴ rings as shown in figure 4.4a. The ¹⁹F MAS NMR showing a peak located at -56.4 ppm confirms this. This value is in agreement with those recorded for the fluoride anions of [SiO₄F] units in siliceous zeolites prepared in fluoride medium (-50 to -80 ppm). The Si-F distance of 2.141(38) Å is also typical of those reported in siliceous zeolites. The fluoride is disordered over every second 5⁴ ring surrounding the channel systems. Distances between the pyridine molecules and the fluoride are in the range of 5.10(5) and 8.69(5) Å.

The location of the fluorine within 5-rings is also seen within ITQ-4 and ITQ-9 where it occupies the [4³5²6¹] cage.^{20,21} The fluorine demonstrates contrasting static and dynamic disorder within this cage, in the cases of ITQ-9 and ITQ-4 respectively. The two crystallographic fluorine sites per cage reflect the dynamic disorder in ITQ-4 (see chapter 5). Ferrierite seems to have one crystallographic site per cage, which is suggestive of static disorder. However a ²⁹Si NMR would be needed to confirm this.

In summary it has been shown that the synthetic approach can influence the inclusion of framework fluorine. Pyridine remains the templating agent, however due

to the acidic conditions it becomes protonated and results in the incorporation of fluoride into the framework.

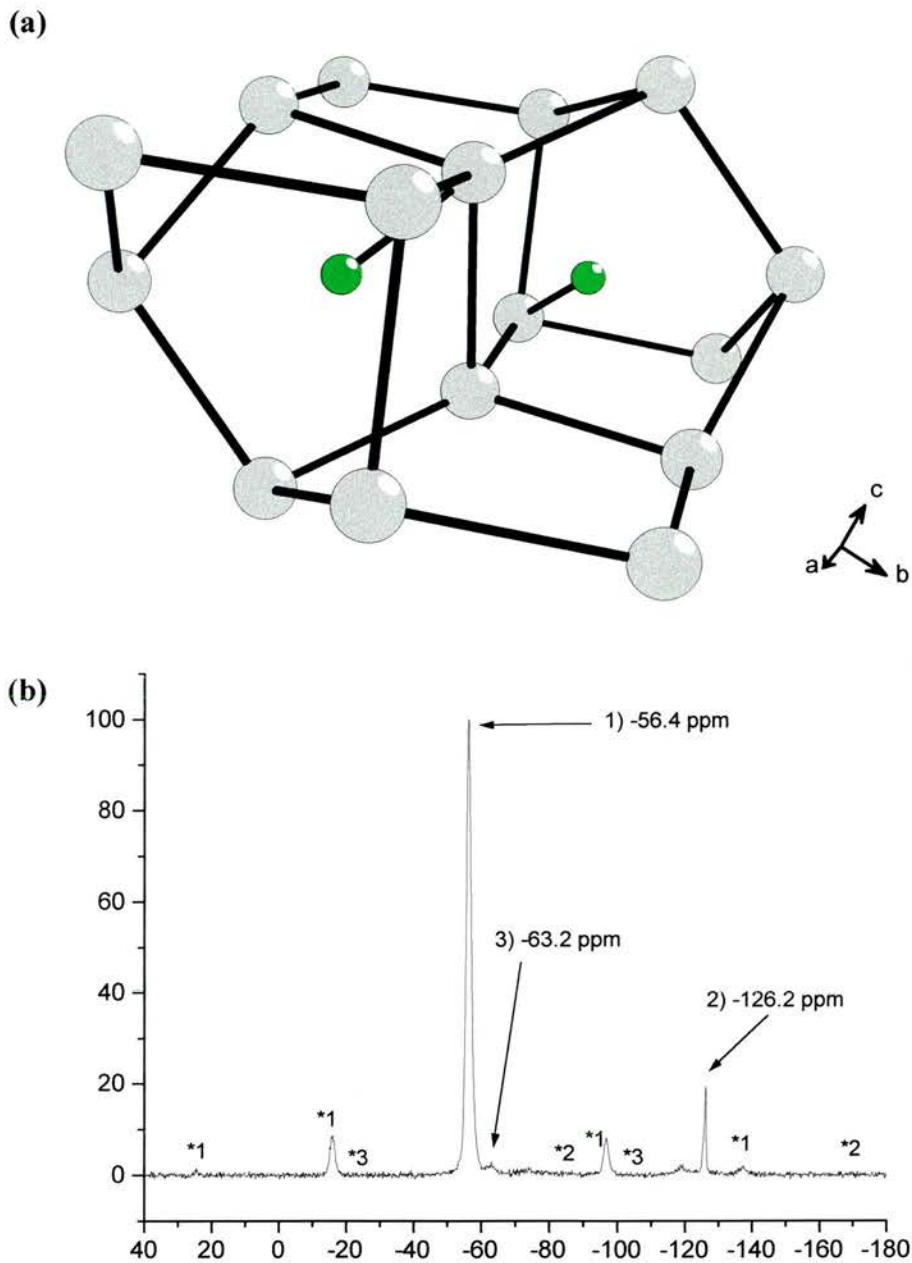


Figure 7.4 (a) Shows the location of fluorine within every second 5^4 ring (Si-F distance = 2.121(38) Å). Oxygen has been removed for clarity. (b) ^{19}F MAS NMR spectrum of PyrF-SiFer confirming the presence of fluoride. The peaks labelled with a * relate to spinning side bands.

4.3.2 Structure of Calcined Ferrierite with Temperature.

The structure of calcined ferrierite was solved by direct methods (SHELXS-97) and refined with full-matrix least-squares technique (SHELXL-97).¹⁷ It was refined in space group Pnm and Immm for all 13 data sets which were collected between 133K and 513K- full details of a low, medium and high temperature data collection can be found in tables 4.4 to 4.11. Full details of the structure determination can be found on the attached CD as Crystallographic Information Files. A representative framework of calcined ferrierite can be seen in figure 4.1, which was collected at 133K.

Table 4.4 lists the crystal data and refinement details for the variable temperature study. Later in the chapter there is a discussion of a phase transition from Pnm to Immm with increasing temperature, and this is reflected in the choice of refinement details shown in table 4.4. Pnm details are shown for the low and medium temperature data sets (i.e. 133 and 300 K) and the Immm details are shown for the high temperature data set (513 K). It can be noted that the number of reflections collected is considerably lower for the Immm data set as all the systematically absent reflections ($h+k+l \neq 2n$) are discarded during the integration in SADABS. In addition problems with beam at the CCLRC Synchrotron Radiation Source, Daresbury Laboratories, resulted in a reduction in data within some of the data sets. Time constraints meant we could only collect one shell of data, which restricted our index ranges to approximately two thirds of the normal range. However this easily covers the required data range for an orthorhombic cell.

Table 4.5 shows the atomic positions and the equivalent isotropic displacement parameters for the aforementioned data. It clearly illustrates that the equivalent isotropic displacement parameters increase with temperature as the atoms vibrate

more. In addition the crystallographic origin was kept the same for each refinement to simplify the variable temperature study of the framework.

Table 4.4 Crystal data and structure refinement for ferrierite collected at 133, 300 and 513 K.

Identification code	Ferrierite		
Empirical formula	O ₇₂ Si ₃₆		
Formula weight	2163.24		
Crystal system	orthorhombic		
Crystal size	0.05 x 0.05 x 0.05 mm		
Z	1		
Density (calculated)	1.843 Mg/m ³		
Absorption coefficient	0.693 mm ⁻¹		
Refinement method	Full-matrix least-squares on F ²		
Temperature	133(2) K	300(2) K	513(2) K
Wavelength	0.68920 Å	0.68920 Å	0.68920 Å
Space group	Pnmm	Pnmm	Immm
Unit cell dimensions	a = 7.411(3) Å b = 14.070(5) Å c = 18.687(10) Å	a = 7.4156(4) Å b = 14.0613(7) Å c = 18.7183(13) Å	a = 7.454(6) Å b = 14.099(11) Å c = 18.692(13) Å
Volume	1948.7(15) Å ³	1951.8(2) Å ³	1964(3) Å ³
F(000)	1080	1080	1080
θ range for data collection	2.81 to 29.50°	2.81 to 29.49°	2.89 to 30.05°
Index ranges	-7 ≤ h ≤ 10, -20 ≤ k ≤ 19, -22 ≤ l ≤ 25	-7 ≤ h ≤ 10, -20 ≤ k ≤ 19, -24 ≤ l ≤ 25	-4 ≤ h ≤ 10, -19 ≤ k ≤ 2, -14 ≤ l ≤ 18
Reflections collected	12999	13387	1985
Independent reflections	2898 [R(int) = 0.0508]	2908 [R(int) = 0.0550]	1015 [R(int) = 0.0489]
Completeness to θ = 29.50°	94.4 %	94.5 %	61.8 %
Max. & min. transmission	0.9863 & 0.9662	0.9939 & 0.9699	
Data / restraints / parameters	2898 / 0 / 125	2908 / 0 / 125	1015 / 0 / 71
Goodness-of-fit on F ²	1.108	1.015	1.117
Final R indices [I > 2σ(I)]	R1 = 0.0511, wR2 = 0.1107	R1 = 0.0438, wR2 = 0.1085	R1 = 0.0906, wR2 = 0.2184
R indices (all data)	R1 = 0.0680, wR2 = 0.1158	R1 = 0.0670, wR2 = 0.1160,	R1 = 0.1352, wR2 = 0.2567

Largest diff. peak & hole

0.665 & -0.535

0.510 & -0.468

0.782 & -1.173

Table 4.5 Atomic coordinates and equivalent isotropic displacement parameters (\AA^2) for ferrierite at 133, 300 and 513K. $U(\text{eq})$ is defined as one third of the trace of the orthogonalized U_{ij} tensor.

133 K	x	y	z	U(eq)
Si(1)	0.2227(1)	0.6969(1)	0.3333(1)	0.008(1)
Si(2)	0.1897(1)	0.2918(1)	0.3168(1)	0.007(1)
Si(3)	0.5120(1)	0.7993(1)	0.4169(1)	0.006(1)
Si(4)	0.5000	1.0000	0.3476(1)	0.007(1)
Si(5)	0.2919(1)	0.4992(1)	0.2732(1)	0.009(1)
O(1)	0.5590(4)	0.7899(2)	0.5000	0.011(1)
O(2)	0.5000	0.5000	0.2502(2)	0.019(1)
O(3)	0.2419(3)	0.4019(2)	0.3128(1)	0.020(1)
O(4)	0.4758(3)	0.9086(2)	0.3973(1)	0.015(1)
O(5)	0.2514(3)	0.5844(2)	0.3282(1)	0.016(1)
O(6)	0.3340(3)	0.7380(2)	0.4001(1)	0.011(1)
O(7)	0.3205(3)	0.2387(2)	0.3711(1)	0.014(1)
O(8)	0.135(3)	0.7202(2)	0.3450(1)	0.019(1)
O(9)	0.2970(3)	0.7466(2)	0.2615(1)	0.018(1)
O(10)	0.6750(3)	0.9868(2)	0.2983(1)	0.021(1)

300 K	x	y	z	U(eq)
Si(1)	0.2176(1)	0.6987(1)	0.3307(1)	0.012(1)
Si(2)	0.1953(1)	0.2940(1)	0.3190(1)	0.011(1)
Si(3)	0.5084(1)	0.7993(1)	0.4166(1)	0.010(1)
Si(4)	0.5000	1.0000	0.3468(1)	0.012(1)
Si(5)	0.2927(1)	0.4994(1)	0.2731(1)	0.014(1)
O(1)	0.5422(4)	0.7896(2)	0.5000	0.020(1)
O(2)	0.5000	0.5000	0.2499(2)	0.027(1)
O(3)	0.2446(3)	0.4043(1)	0.3149(1)	0.032(1)
O(4)	0.4833(3)	0.9086(2)	0.3965(1)	0.028(1)
O(5)	0.2522(3)	0.5867(1)	0.3255(1)	0.027(1)
O(6)	0.3296(2)	0.7414(1)	0.3960(1)	0.021(1)
O(7)	0.3215(3)	0.2424(2)	0.3749(1)	0.027(1)
O(8)	0.87(2)	0.7187(2)	0.3448(1)	0.027(1)
O(9)	0.2835(3)	0.7484(2)	0.2585(1)	0.032(1)

	O(10)	0.6751(3)	0.9912(2)	0.2979(1)	0.034(1)
513 K					
	x	y	z	U(eq)	
Si(1)	0.0000	0.2992(2)	0.0835(2)	0.026(1)	
Si(2)	0.2939(2)	0.2021(1)	0.1755(1)	0.029(1)	
Si(3)	0.0000	0.5000	0.1536(2)	0.029(1)	
Si(4)	0.2059(4)	0.0000	0.2268(2)	0.034(1)	
O(1)	0.5000	0.2185(5)	0.1562(6)	0.059(3)	
O(2)	0.2507(9)	0.0911(3)	0.1807(3)	0.055(2)	
O(3)	0.0000	0.2897(7)	0.0000	0.043(3)	
O(4)	0.0000	0.0000	0.2502(7)	0.060(4)	
O(5)	0.1756(8)	0.5867(1)	0.3255(3)	0.056(2)	
O(6)	0.0000	0.7414(1)	0.3960(4)	0.057(3)	
O(7)	0.1738(11)	0.5000	0.2018(5)	0.063(3)	
O(8)	0.2500	0.2500	0.2500	0.073(3)	

Table 4.6 Bond lengths [Å] and angles [°] for ferrierite at 133 K.

Si(1)-O(8)	1.599(2)	Si(5)-O(10)#5	1.605(2)
Si(1)-O(5)	1.600(2)	Si(5)-O(5)	1.607(2)
Si(1)-O(6)	1.603(2)	O(1)-Si(3)#6	1.5962(13)
Si(1)-O(9)	1.610(2)	O(2)-Si(5)#3	1.6013(13)
Si(2)-O(7)	1.590(2)	O(7)-Si(3)#3	1.599(2)
Si(2)-O(3)	1.598(2)	O(8)-Si(2)#2	1.605(2)
Si(2)-O(9)#1	1.600(2)	O(9)-Si(2)#7	1.600(2)
Si(2)-O(8)#2	1.605(2)	O(10)-Si(5)#8	1.605(2)
Si(3)-O(1)	1.5962(13)	O(8)-Si(1)-O(5)	109.82(13)
Si(3)-O(7)#3	1.599(2)	O(8)-Si(1)-O(6)	108.58(12)
Si(3)-O(4)	1.604(2)	O(5)-Si(1)-O(6)	109.56(12)
Si(3)-O(6)	1.608(2)	O(8)-Si(1)-O(9)	110.90(13)
Si(4)-O(4)#4	1.596(2)	O(5)-Si(1)-O(9)	109.53(12)
Si(4)-O(4)	1.596(2)	O(6)-Si(1)-O(9)	108.42(12)
Si(4)-O(10)#4	1.602(2)	O(7)-Si(2)-O(3)	109.80(13)
Si(4)-O(10)	1.602(2)	O(7)-Si(2)-O(9)#1	111.07(13)
Si(5)-O(3)	1.599(2)	O(3)-Si(2)-O(9)#1	109.11(13)
Si(5)-O(2)	1.6013(13)	O(7)-Si(2)-O(8)#2	108.27(12)

O(3)-Si(2)-O(8)#2	110.17(13)	O(3)-Si(5)-O(10)#5	111.42(13)
O(9)#1-Si(2)-O(8)#2	108.40(13)	O(2)-Si(5)-O(10)#5	107.20(15)
O(1)-Si(3)-O(7)#3	108.87(14)	O(3)-Si(5)-O(5)	107.42(13)
O(1)-Si(3)-O(4)	109.82(14)	O(2)-Si(5)-O(5)	110.27(12)
O(7)#3-Si(3)-O(4)	109.14(12)	O(10)#5-Si(5)-O(5)	109.88(13)
O(1)-Si(3)-O(6)	108.97(13)	Si(3)#6-O(1)-Si(3)	153.0(2)
O(7)#3-Si(3)-O(6)	110.63(12)	Si(5)-O(2)-Si(5)#3	148.8(2)
O(4)-Si(3)-O(6)	109.40(12)	Si(2)-O(3)-Si(5)	155.17(17)
O(4)#4-Si(4)-O(4)	108.88(17)	Si(4)-O(4)-Si(3)	152.51(15)
O(4)#4-Si(4)-O(10)#4	109.38(12)	Si(1)-O(5)-Si(5)	143.19(15)
O(4)-Si(4)-O(10)#4	109.73(12)	Si(1)-O(6)-Si(3)	140.21(14)
O(4)#4-Si(4)-O(10)	109.73(12)	Si(2)-O(7)-Si(3)#3	166.32(16)
O(4)-Si(4)-O(10)	109.38(12)	Si(1)-O(8)-Si(2)#2	147.53(16)
O(10)#4-Si(4)-O(10)	109.73(19)	Si(2)#7-O(9)-Si(1)	163.05(17)
O(3)-Si(5)-O(2)	110.68(11)	Si(4)-O(10)-Si(5)#8	154.42(17)

Symmetry transformations used to generate equivalent atoms:

#1 -x+1/2,y-1/2,-z+1/2 #2 -x,-y+1,z #3 -x+1,-y+1,z
 #4 -x+1,-y+2,z #5 x-1/2,-y+3/2,-z+1/2 #6 x,y,-z+1
 #7 -x+1/2,y+1/2,-z+1/2 #8 x+1/2,-y+3/2,-z+1/2

Table 4.7 Bond lengths [\AA] and angles [$^\circ$] for ferrierite at 300 K.

Si(1)-O(6)	1.5949(19)	Si(5)-O(2)	1.5975(11)
Si(1)-O(8)	1.5964(19)	Si(5)-O(5)	1.600(2)
Si(1)-O(9)	1.598(2)	O(1)-Si(3)#6	1.5879(8)
Si(1)-O(5)	1.598(2)	O(2)-Si(5)#3	1.5975(11)
Si(2)-O(7)	1.5804(19)	O(7)-Si(3)#3	1.5945(19)
Si(2)-O(9)#1	1.593(2)	O(8)-Si(2)#2	1.5984(19)
Si(2)-O(3)	1.595(2)	O(9)-Si(2)#7	1.593(2)
Si(2)-O(8)#2	1.5984(19)	O(10)-Si(5)#8	1.594(2)
Si(3)-O(1)	1.5879(8)	O(6)-Si(1)-O(8)	108.17(11)
Si(3)-O(4)	1.593(2)	O(6)-Si(1)-O(9)	108.94(11)
Si(3)-O(7)#3	1.5945(19)	O(8)-Si(1)-O(9)	111.10(12)
Si(3)-O(6)	1.6029(19)	O(6)-Si(1)-O(5)	109.50(11)
Si(4)-O(4)#4	1.591(2)	O(8)-Si(1)-O(5)	109.81(12)
Si(4)-O(4)	1.591(2)	O(9)-Si(1)-O(5)	109.30(12)
Si(4)-O(10)#4	1.594(2)	O(7)-Si(2)-O(9)#1	111.03(12)
Si(4)-O(10)	1.594(2)	O(7)-Si(2)-O(3)	110.01(12)
Si(5)-O(3)	1.590(2)	O(9)#1-Si(2)-O(3)	108.99(12)
Si(5)-O(10)#5	1.594(2)	O(7)-Si(2)-O(8)#2	108.01(11)

O(9)#1-Si(2)-O(8)#2	108.89(12)	O(3)-Si(5)-O(2)	110.73(10)
O(3)-Si(2)-O(8)#2	109.90(12)	O(10)#5-Si(5)-O(2)	107.42(14)
O(1)-Si(3)-O(4)	109.46(14)	O(3)-Si(5)-O(5)	107.51(12)
O(1)-Si(3)-O(7)#3	108.97(13)	O(10)#5-Si(5)-O(5)	110.17(12)
O(4)-Si(3)-O(7)#3	109.40(11)	O(2)-Si(5)-O(5)	110.12(11)
O(1)-Si(3)-O(6)	108.86(12)	Si(3)-O(1)-Si(3)#6	159.3(2)
O(4)-Si(3)-O(6)	109.67(11)	Si(5)-O(2)-Si(5)#3	148.4(2)
O(7)#3-Si(3)-O(6)	110.48(11)	Si(5)-O(3)-Si(2)	153.20(15)
O(4)#4-Si(4)-O(4)	108.49(16)	Si(4)-O(4)-Si(3)	155.21(15)
O(4)#4-Si(4)-O(10)#4	109.68(11)	Si(1)-O(5)-Si(5)	145.39(14)
O(4)-Si(4)-O(10)#4	109.57(12)	Si(1)-O(6)-Si(3)	143.70(13)
O(4)#4-Si(4)-O(10)	109.57(12)	Si(2)-O(7)-Si(3)#3	164.00(15)
O(4)-Si(4)-O(10)	109.68(11)	Si(1)-O(8)-Si(2)#2	148.06(15)
O(10)#4-Si(4)-O(10)	109.83(19)	Si(2)#7-O(9)-Si(1)	167.41(16)
O(3)-Si(5)-O(10)#5	110.91(12)	Si(5)#8-O(10)-Si(4)	156.64(17)

Symmetry transformations used to generate equivalent atoms:

#1 -x+1/2,y-1/2,-z+1/2 #2 -x,-y+1,z #3 -x+1,-y+1,z
#4 -x+1,-y+2,z #5 x-1/2,-y+3/2,-z+1/2 #6 x,y,-z+1
#7 -x+1/2,y+1/2,-z+1/2 #8 x+1/2,-y+3/2,-z+1/2

Table 4.8 Bond lengths [\AA] and angles [$^\circ$] for ferrierite 513 K.

Si(1)-O(3)	1.566(4)	O(3)-Si(1)#6	1.566(4)
Si(1)-O(6)	1.588(7)	O(4)-Si(4)#7	1.596(5)
Si(1)-O(5)	1.598(6)	O(7)-Si(4)#4	1.607(9)
Si(1)-O(5)#1	1.598(6)	O(8)-Si(2)#4	1.582(2)
Si(2)-O(8)	1.582(2)	O(3)-Si(1)-O(6)	108.9(5)
Si(2)-O(5)	1.584(6)	O(3)-Si(1)-O(5)	109.1(3)
Si(2)-O(1)	1.595(3)	O(6)-Si(1)-O(5)	109.8(3)
Si(2)-O(2)	1.600(5)	O(3)-Si(1)-O(5)#1	109.1(3)
Si(3)-O(7)	1.578(8)	O(6)-Si(1)-O(5)#1	109.8(3)
Si(3)-O(7)#2	1.578(8)	O(5)-Si(1)-O(5)#1	110.1(5)
Si(3)-O(6)#2	1.589(8)	O(8)-Si(2)-O(5)	109.7(2)
Si(3)-O(6)	1.589(8)	O(8)-Si(2)-O(1)	109.7(4)
Si(4)-O(2)#3	1.583(5)	O(5)-Si(2)-O(1)	108.3(4)
Si(4)-O(2)	1.583(5)	O(8)-Si(2)-O(2)	108.8(2)
Si(4)-O(4)	1.596(5)	O(5)-Si(2)-O(2)	110.0(3)
Si(4)-O(7)#4	1.607(9)	O(1)-Si(2)-O(2)	110.4(4)
O(1)-Si(2)#5	1.595(3)	O(7)-Si(3)-O(7)#2	110.4(8)

O(7)-Si(3)-O(6)#2	109.5(3)	O(4)-Si(4)-O(7)#4	108.0(6)
O(7)#2-Si(3)-O(6)#2	109.5(3)	Si(2)#5-O(1)-Si(2)	148.8(7)
O(7)-Si(3)-O(6)	109.5(3)	Si(4)-O(2)-Si(2)	150.3(4)
O(7)#2-Si(3)-O(6)	109.5(3)	Si(1)#6-O(3)-Si(1)	170.2(7)
O(6)#2-Si(3)-O(6)	108.6(6)	Si(4)#7-O(4)-Si(4)	148.2(10)
O(2)#3-Si(4)-O(2)	108.5(5)	Si(2)-O(5)-Si(1)	154.7(4)
O(2)#3-Si(4)-O(4)	110.6(3)	Si(1)-O(6)-Si(3)	158.3(6)
O(2)-Si(4)-O(4)	110.6(3)	Si(3)-O(7)-Si(4)#4	158.7(8)
O(2)#3-Si(4)-O(7)#4	109.5(3)	Si(2)-O(8)-Si(2)#4	180.0(8)
O(2)-Si(4)-O(7)#4	109.5(3)		

Symmetry transformations used to generate equivalent atoms:

#1 -x,y,z #2 -x,-y+1,z #3 x,-y,z #4 -x+1/2,-y+1/2,-z+1/2
 #5 -x+1,y,z #6 x,y,-z #7 -x,-y,z

Table 4.9 Anisotropic displacement parameters (\AA^2) for ferrierite at 133 K. The anisotropic displacement factor exponent takes the form: $-2\pi^2 [h^2 a^*^2 U_{11} + \dots + 2 h k a^* b^* U_{12}]$

	U_{11}	U_{22}	U_{33}	U_{23}	U_{13}	U_{12}
Si(1)	0.007(1)	0.008(1)	0.008(1)	-0.001(1)	-0.002(1)	0.001(1)
Si(2)	0.006(1)	0.008(1)	0.007(1)	0.001(1)	-0.001(1)	0.000(1)
Si(3)	0.007(1)	0.007(1)	0.005(1)	0.000(1)	0.001(1)	0.000(1)
Si(4)	0.007(1)	0.008(1)	0.008(1)	0.000	0.000	0.001(1)
Si(5)	0.007(1)	0.008(1)	0.011(1)	-0.001(1)	-0.001(1)	0.001(1)
O(1)	0.013(1)	0.016(1)	0.005(1)	0.000	0.000	-0.003(1)
O(2)	0.010(1)	0.029(2)	0.017(2)	0.000	0.000	0.003(1)
O(3)	0.030(1)	0.007(1)	0.021(1)	0.001(1)	0.004(1)	-0.003(1)
O(4)	0.021(1)	0.008(1)	0.016(1)	0.004(1)	0.003(1)	0.000(1)
O(5)	0.021(1)	0.009(1)	0.017(1)	-0.003(1)	0.003(1)	0.001(1)
O(6)	0.011(1)	0.015(1)	0.007(1)	-0.001(1)	-0.001(1)	-0.005(1)
O(7)	0.011(1)	0.018(1)	0.012(1)	0.004(1)	-0.005(1)	0.001(1)
O(8)	0.007(1)	0.025(1)	0.024(1)	-0.008(1)	-0.002(1)	0.004(1)
O(9)	0.024(1)	0.020(1)	0.009(1)	0.005(1)	-0.002(1)	0.000(1)
O(10)	0.015(1)	0.027(1)	0.020(1)	0.002(1)	0.011(1)	0.003(1)

Table 4.10 Anisotropic displacement parameters (\AA^2) for calcined ferrierite at 300K.

The anisotropic displacement factor exponent takes the form: $-2\pi^2[h^2a^*{}^2U_{11} + \dots + 2 h k a^* b^* U_{12}]$

	U_{11}	U_{22}	U_{33}	U_{23}	U_{13}	U_{12}
Si(1)	0.011(1)	0.012(1)	0.013(1)	-0.001(1)	-0.002(1)	0.000(1)
Si(2)	0.010(1)	0.012(1)	0.012(1)	0.001(1)	-0.001(1)	0.001(1)
Si(3)	0.010(1)	0.011(1)	0.008(1)	0.000(1)	0.001(1)	0.000(1)
Si(4)	0.012(1)	0.012(1)	0.012(1)	0.000	0.000	0.000(1)
Si(5)	0.011(1)	0.012(1)	0.019(1)	-0.001(1)	-0.002(1)	0.000(1)
O(1)	0.025(1)	0.027(2)	0.010(1)	0.000	0.000	-0.004(1)
O(2)	0.010(1)	0.043(2)	0.029(2)	0.000	0.000	0.001(1)
O(3)	0.045(1)	0.013(1)	0.038(1)	0.002(1)	0.007(1)	-0.007(1)
O(4)	0.040(1)	0.015(1)	0.030(1)	0.007(1)	0.005(1)	0.001(1)
O(5)	0.038(1)	0.013(1)	0.030(1)	-0.004(1)	0.004(1)	0.004(1)
O(6)	0.018(1)	0.028(1)	0.018(1)	-0.003(1)	-0.004(1)	-0.007(1)
O(7)	0.019(1)	0.035(1)	0.027(1)	0.008(1)	-0.009(1)	0.005(1)
O(8)	0.011(1)	0.035(1)	0.035(1)	-0.009(1)	-0.003(1)	0.002(1)
O(9)	0.040(1)	0.036(1)	0.019(1)	0.011(1)	0.001(1)	-0.004(1)
O(10)	0.022(1)	0.050(2)	0.031(1)	0.001(1)	0.014(1)	0.004(1)

Table 4.11 Anisotropic displacement parameters (\AA^2) for calcined ferrierite at 512

K. The anisotropic displacement factor exponent takes the form: $-2\pi^2[h^2a^*{}^2U_{11} + \dots + 2 h k a^* b^* U_{12}]$

	U_{11}	U_{22}	U_{33}	U_{23}	U_{13}	U_{12}
Si(1)	0.019(1)	0.034(1)	0.025(2)	0.002(1)	0.000	0.000
Si(2)	0.020(1)	0.035(1)	0.032(2)	0.003(1)	0.000(1)	0.003(1)
Si(3)	0.021(2)	0.031(2)	0.036(3)	0.000	0.000	0.000
Si(4)	0.020(1)	0.032(1)	0.048(3)	0.000	-0.003(1)	0.000
O(1)	0.019(4)	0.074(5)	0.083(8)	0.016(5)	0.000	0.000
O(2)	0.066(4)	0.039(2)	0.060(5)	0.006(2)	0.000(3)	-0.004(2)
O(3)	0.047(7)	0.061(6)	0.021(10)	0.000	0.000	0.000
O(4)	0.022(5)	0.084(8)	0.074(11)	0.000	0.000	0.000
O(5)	0.040(3)	0.072(3)	0.056(5)	0.015(3)	-0.006(3)	0.016(3)

O(6)	0.084(8)	0.039(3)	0.048(6)	-0.007(3)	0.000	0.000
O(7)	0.033(5)	0.111(7)	0.044(7)	0.000	-0.035(5)	0.000

4.3.3 Second Order Phase Transition of Ferrierite.

The discussion concerning the two reported space groups (Pnmm and Immm) for ferrierite in the literature instigated a NMR study to examine if the symmetry of ferrierite was temperature dependent.⁸ ^{29}Si Magic angle spinning NMR indicated that ferrierite undergoes a possible phase transition with temperature (see figure 4.4). At

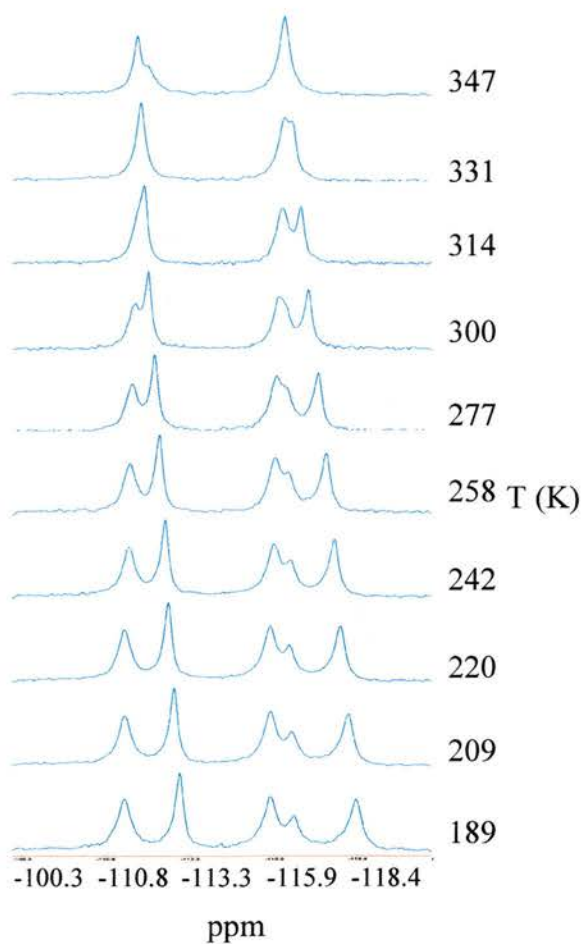


Figure 4.4 Temperature dependence of ^{29}Si NMR spectra for purely siliceous FER.

low temperature it is in space group Pnmm whereas above room temperature it moves towards Immm. This change in symmetry is evident as the number of

crystallographically distinct T atoms reduces from 5 to 4 respectively. The DSC curve (see figure 4.5) quite clearly shows a second order phase transition between 283 and 421 K relating to this change in symmetry. The transition temperature is 360 K with an associated enthalpy change of 24.71 Jg^{-1} .

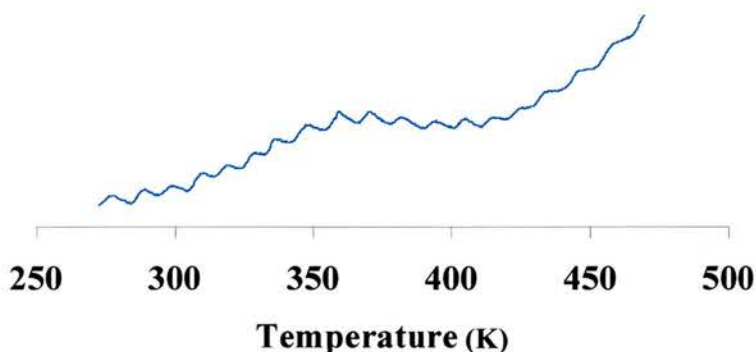


Figure 4.5 Experimental DSC curve corresponding to the second order phase transition in siliceous ferrierite.

The single crystal data were refined in both Pnnm and Immm over the temperature range of 133 and 513 K. The resulting wR2 values can be seen in Figure 4.6 and these show that at low temperatures Ferrierite is Pnnm. However as temperature increased the refinements of this material in Pnnm and Immm became closer together. Above room temperature the wR2 values were better for the Immm structure. The differences are not large as the high temperature data is less good. Reasons for this include the heat softening the glue and glass on which the crystals were mounted leading to difficulties in crystal centring throughout the data collection. In addition this is a second order phase transition which means that it occurs over a broad temperature range leading to a loss of information due to xrd being an average of atom positions. However the data correlates well with the phase change seen in the NMR studies.

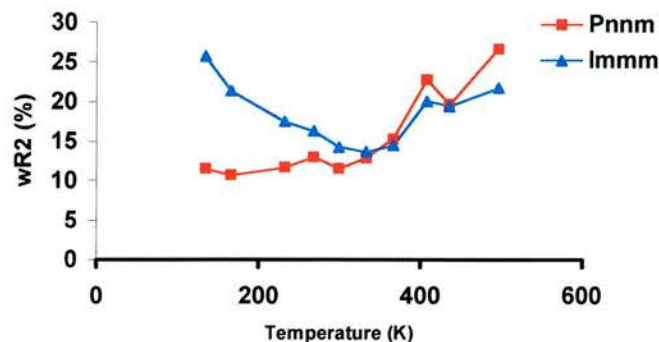


Figure 4.6 wR2 values for each of the single crystal refinements in both Pnnm and Immm. At low temperatures the structure is clearly Pnnm, as the wR2 is 15% better. Then as temperature increases towards room temperature the wR2 values are equally good for Pnnm and Immm. As we move into the higher temperatures the Immm structure is slightly better. However the refinements aren't as accurate at high temperatures due to problems associated with data collection.

This symmetry change also imposes certain constraints on SiOSi bond angles. One of the SiOSi bond angles in the Immm is constrained to 180° (as reported previously by Morris et al.⁸ in their powder work), on heating the corresponding SiOSi bond angle in the Pnnm structure can be seen to approach 180° (see figure 4.7). This indicates that the structure is indeed moving towards Immm. The bond angle is a little unstable in Pnnm, though I would apportion this to problems associated with high correlations because the extra symmetry is not modelled - as T atoms become equivalent - which results in poorer data. In addition the Pnnm high temperature refinements are of slightly less precision compared to the lower temperatures.

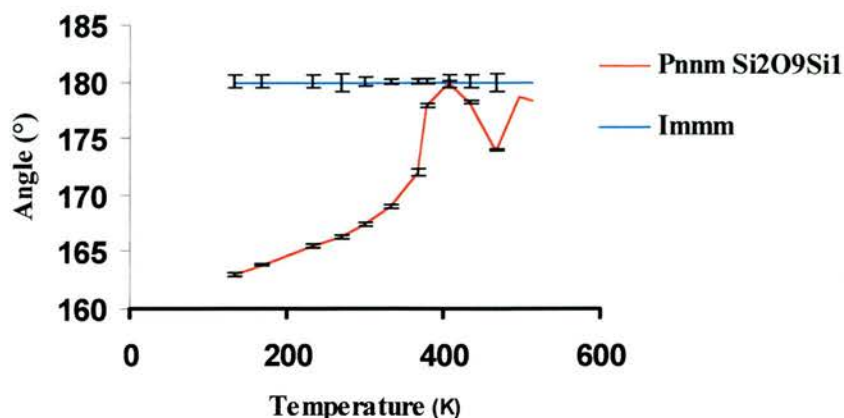


Figure 4.7 It can be seen that with increasing temperature the Si2O8Si1 bond angle in Pnnm approaches the value of the corresponding Si2O8Si2 bond angle in Immm, which is constrained to 180° by symmetry.

Although the 180° bond angle mentioned makes good crystallographic sense (as the space group enforces this), it seems highly unlikely that this angle would exist chemically. A discussion of this issue is found later in the chapter.

The effect the different symmetry has on bond angles can also be seen in the shape of the channels as seen in figure 4.8a. In Pnnm the 10 MR and 8 MRs are egg shaped with one end wider than the other, whereas in Immm the channels are oval. The symmetry changes from Pnnm to Immm with increasing temperature results in two T atoms becoming equivalent and this can be seen in the bond angles (see figure 4.8b). In both the 8 MR and the 10 MR the Si3O7Si2 and Si3O6Si1 angles in Pnnm move towards the value of the corresponding Si1O5Si2 angle in Immm (i.e. 2 T atoms are reduced to one). Furthermore in the 10 MR, the Si2O3Si5 and Si5O5Si1 angles in the Pnnm refinements approach the value of the corresponding Si2O2Si4 angle in Immm as temperature is increased. These changes are clear evidence that the structure is undergoing a Pnnm to Immm phase transition.

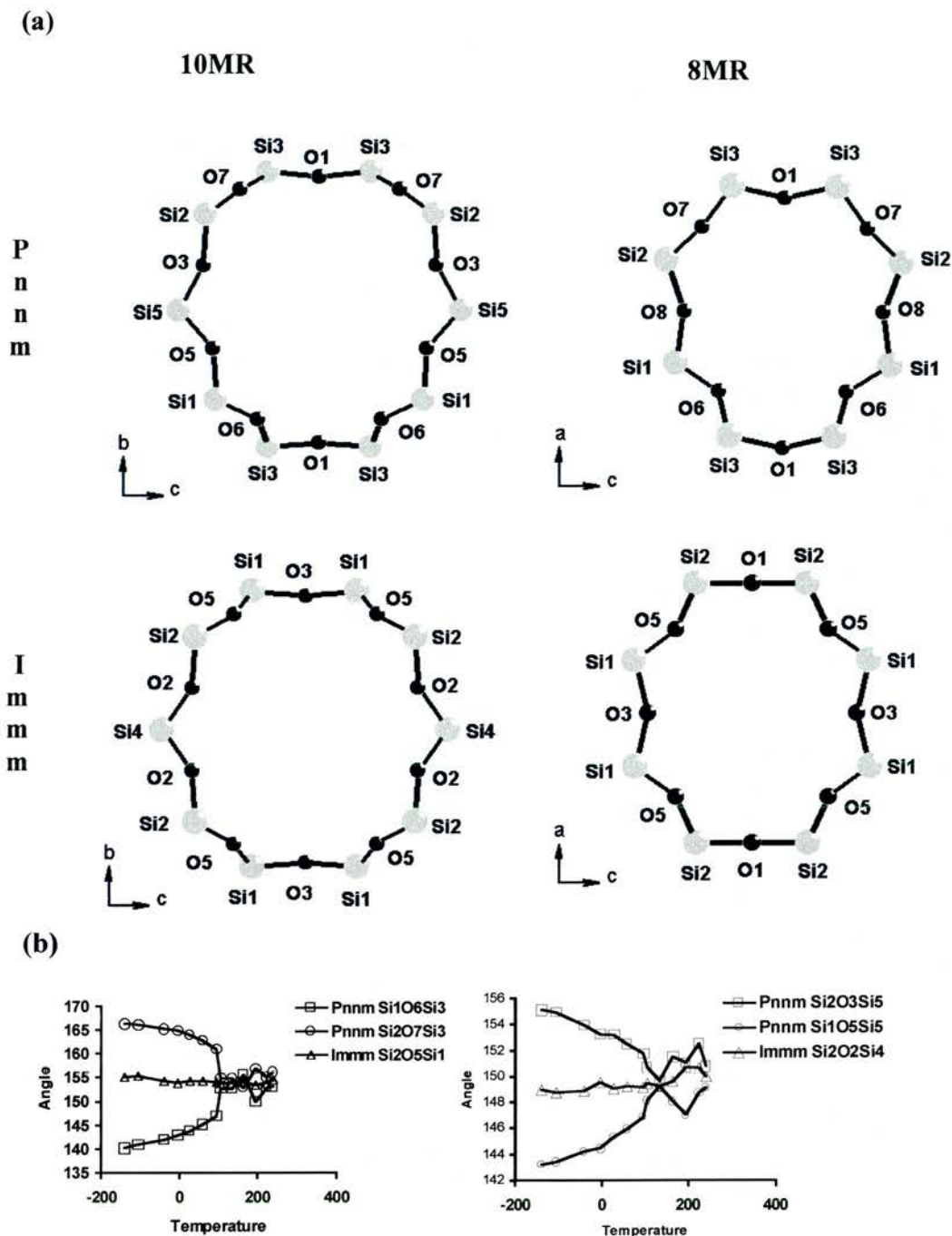


Figure 4.8 (a) depicts the different shapes of the 8MR and 10MR in the Pnnm and the Immm structures. The Pnnm channels can be described, as egg shaped with one end wider than the other, i.e. in the 8MR and 10MR the Si2-Si2 distance is larger than the Si1-Si1 distance. However when Immm symmetry is imposed on the structure, the channels become oval in shape and the two Pnnm distances that differed become equal. This can be seen in (b) where the two individual angles in the Pnnm models merge towards the Immm value with temperature.

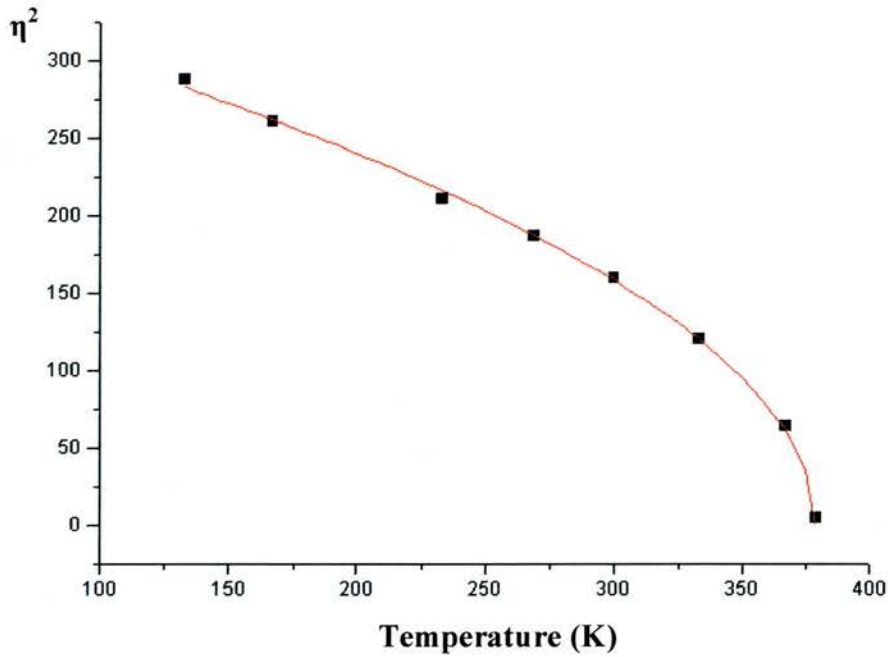


Figure 4.9 Experimental data (in relation to the angle change seen in fig. 4.7) for the temperature dependence of the order parameter (η) as stated in the Landau Theory. The red trendline can be fitted to the term $|T_c - T|^\beta$, giving $\beta=0.5$. This relates to a second order phase transition.

In the Landau theory the order parameter, η , is a measure of the distortion caused by a phase transition. In this case we examine the changes in bond angles with temperature discussed in the previous two paragraphs. When we apply the Landau theory of phase transitions to these changes, we obtain a graph of order parameter, η^2 , versus temperature (see figure 4.9).¹³ This trendline can be fitted to $|T_c - T|^\beta$, where T_c is the transition temperature and β is termed the “critical exponent”. β describes the variation of the order parameter with temperature for the phase transition. For a second order phase transition it is stated that $\beta=0.5$ for which our value agrees.

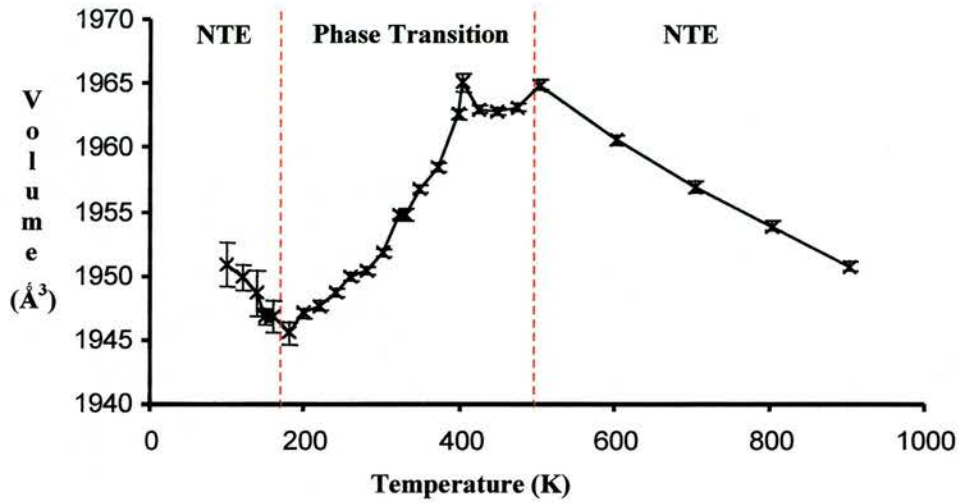


Figure 4.10 Powder XRD data shows the affect that the phase transition has on the thermal behaviour of Ferrierite. The region of positive thermal expansion approximately coincides with a low symmetry to high symmetry phase transition.

It has now clearly been established that Ferrierite undergoes a second order phase transition from Pnmm to Immm between 283 and 421 K, and if we examine the powder xrd results in figure 4.10 it can quite clearly be seen that it has an affect on the thermal behaviour. Many zeolites demonstrate negative thermal expansion, NTE, and Ferrierite does exhibit NTE behaviour when in Pnmm or Immm. However during this second order phase transition the material expands as a result of the change in shape of the channels. This change in thermal expansivity may be associated with excitation of phonon modes that result in the structure beginning to move towards the higher symmetry. Clearly when the channels move from being egg shaped to oval there will be an net increase on volume as the shape removes the short and fat ends to produce a symmetrical oval channel. The DSC shows no evidence for another phase transition and the crystallography shows no evidence of, for example, a monoclinic distortion. However, further experiments at even lower temperatures would be

needed to prove this. It can be concluded that when Ferrierite is Pnmm or Immm it behaves as an NTE material, but when at temperatures just below the phase transition this behaviour is interrupted.

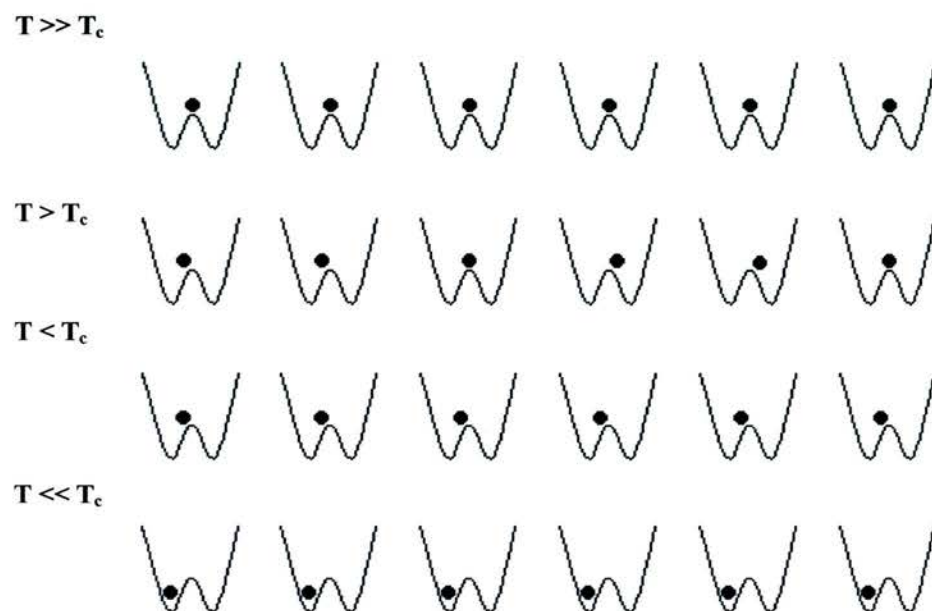


Figure 4.11 Sequence illustrating the ordering of atoms in the displacive limit. At temperatures much higher than the transition temperature, T_c , ($T \gg T_c$) the atoms vibrate about the zero position, and the effects of the double-well potential are not important. On cooling towards T_c ($T > T_c$) the effects of the double well potential become significant and short-range order is observed where neighbouring atoms are temporarily displaced from the origin. Slightly below T_c ($T < T_c$) all the atoms vibrate in displaced positions that are shifted away from the origin. At very low temperatures ($T \ll T_c$) all the atoms occupy the same position in the double-well potential.

The reason for this phase transition is due to a long range driving force, described by Dove in his review of phase transitions in minerals,¹⁸ in which the atom vibrations can be described by a double-well potential. An atom interacts with its neighbours by harmonic forces and these result in an ordering of a structure. Figure 4.11 illustrates how the atom positions vary with temperature due to their vibrations, which has obvious implications on the structure. In the case of this phase transition the atoms, at high temperatures the atoms have a great deal of vibrational energy and this results in the atoms ordering into one average position and hence high symmetry (Immm).

However on cooling the atoms have less energy and fall to one of the lower energy states to either side of the high temperature position and results in lower symmetry (Pnmm).

There are a variety of influences on this double well potential. One of the contributions to this double-well potential is the SiOSi bond angles moving from the normal value of $\sim 145^\circ$ to that of a higher energy, i.e. 180° . The driving force for the Pnmm to Immm phase transition is quite clearly the resulting constraint of 180° bond angle. However local deformations must occur to allow this 180° angle as depicted in figure 4.12. In ferrierite the remaining tetrahedra rotate to try and accommodate this angle via a mechanism which is described by the rigid unit model resulting in a displacive transition.¹⁹

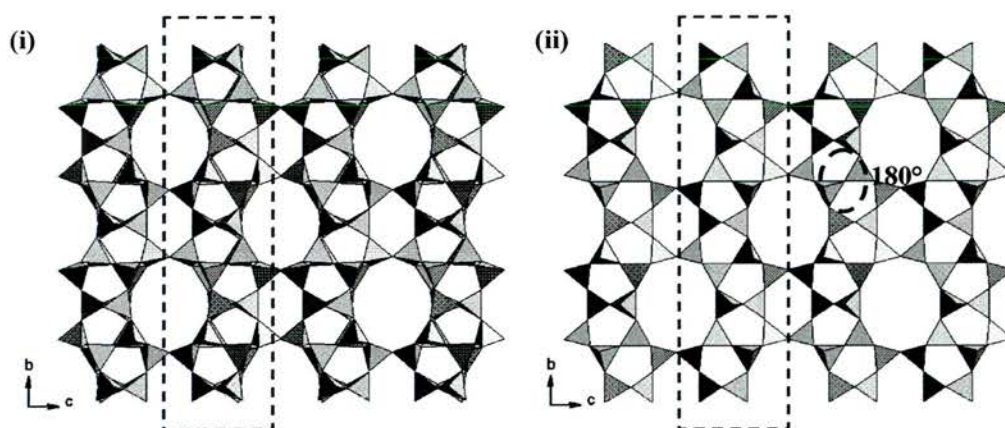


Fig. 4.12 The transition from (i) Pnmm to the higher symmetry of Immm (ii) lines up the layers (outlined within the dashed box) due to the 180° constraint in the latter (outlined in the dashed circle). This can be seen looking down the a and b axes. It can also be seen that the tetrahedra are rotating to obtain this 180° .

This model of the phase transition is as crystallographically accurate as our data allows us to be due to the resolution of the technique. However as mentioned previously the 180° bond angle does not make chemical sense. Figure 4.13 illustrates a more sensible model of what should be seen. In our crystallographic structure the O8 is located on a special position leading to the constrained 180°

angle, however it is more chemically accurate to try and refine the O8 displaced slightly from this special position. This was carried out for the highest three temperatures, which should correlate well to Immm. The isotropic displacement parameters improved when this was done as seen in table 4.11. However when the atom was refined anisotropically the atom had non-positive definite which is a sign that the resolution of our data is not good enough or that the model is poor. The resolution of our data is 0.6882 Å (d-min) as a wavelength of 0.6883 Å was used to collect data up to $2\theta=30.05$. The distances between the O8 on the special position and the displaced position were 0.211, 0.151, and 0.201 Å at 240, 224, and 195 K respectively. Hence the resolution is not good enough to see such small differences. However, the Difference Fourier Map was examined (see figure 4.14) to determine if there was displacement and it could be seen that there was a large amount of electron density around the O8 special position. If there were two distinct atomic positions the electron density in the Difference Fourier Map would be expected to be the shape of a peanut. Although there was no clear peanut shape that would clearly suggest the displaced model, the electron density did seem rather expansive and round, which would suggest that the atom is not located exclusively on the special position. This is illustrated in figure 4.14.

Table 4.11 Atomic coordinates and equivalent isotropic displacement parameters (Å²) for O8 on two positions (i.e. special position that results in the 180 ° angle and displaced slightly from this position) at 240, 224 and 195 K. $U(eq)$ is defined as one third of the trace of the orthogonalized U_{ij} tensor.

	x	y	z	$U(eq)$
240 K				
O8 special	0.25	0.25	0.25	0.07336
O8 displaced	0.236681	0.261612	0.245299	0.05532
224 K				
O8 special	0.25	0.25	0.25	0.05976
O8 displaced	0.245149	0.258297	0.245289	0.05235

195 K				
O8 special	0.25	0.25	0.25	0.06286
O8 displaced	0.226925	0.243226	0.252079	0.04832

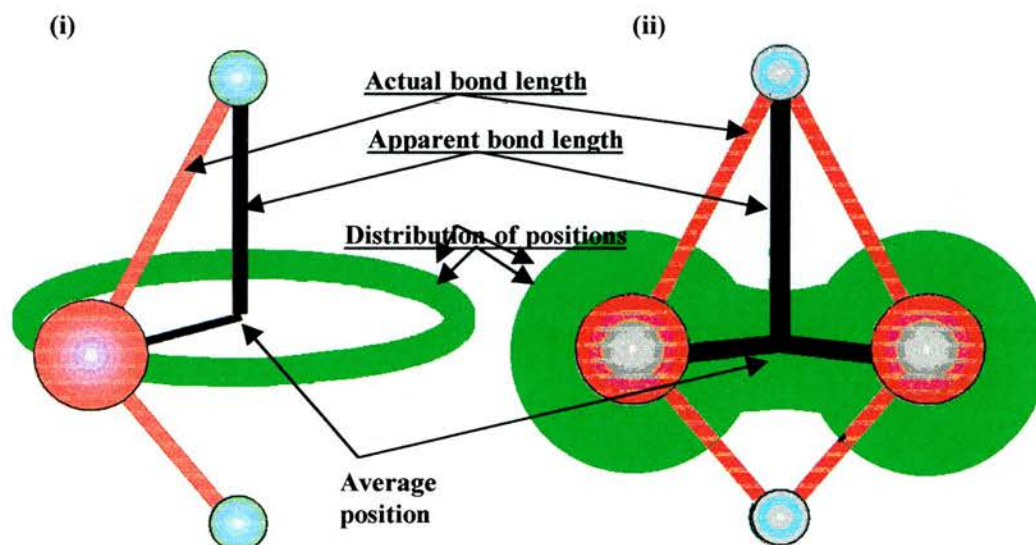


Figure 4.13 Illustration of the difference between actual instantaneous interatomic separations and the separation in average positions where the Si is the blue circles and the O is the red circle. There are two possibilities for the positions of these: (i) this models the oxygen is free to rotate between the silicon atoms resulting in a disc-like distribution of electron density whereas (ii) models the oxygen vibrating in two positions either side of the average position (each $\frac{1}{2}$ occupied) resulting in a peanut shape distribution of electron density. In this case the average position is the special position (x,y,z) 0.25,0.25,0.25 which leads to the 180° constraint.

In conclusion ferrierite does indeed undergo a 2nd order displacive phase transition between 280 and 421 K. Either side of this phase transition the material exhibits NTE and a discussion of the low temperature Pnnm NTE will follow in the next section.

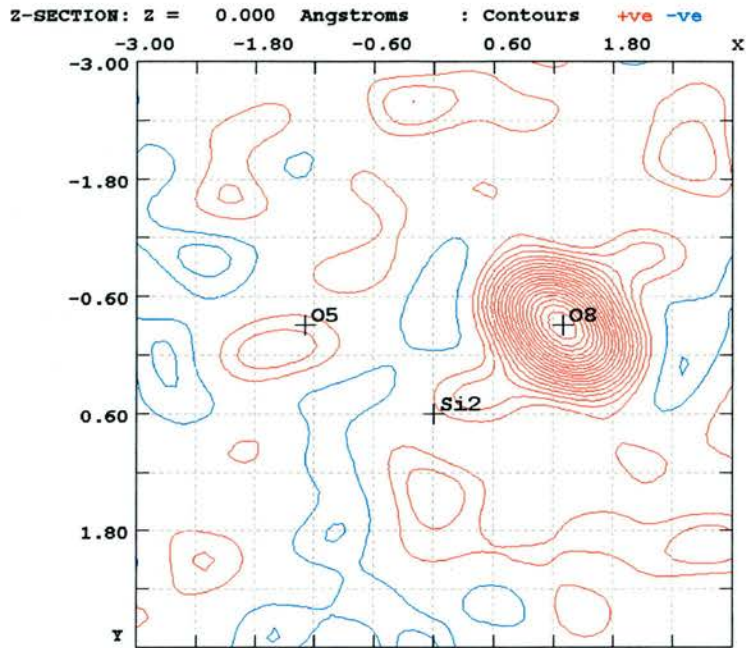


Figure 4.14 Difference Fourier Map showing the electron density along the O5Si2O8 plane. It is clear that the electron density does not demonstrate a purely peanut or a purely disc-like distribution. Instead it is suggestive of a mix of the two.

4.3.4 Negative Thermal Expansion of Ferrierite

As seen previously in figure 4.10 ferrierite demonstrates NTE at low temperature (< 300 K) when Pnm and at high temperature (>500 K) when Immm. The phase transition is the first factor that limits our study of the NTE, as we do not want to confuse the structural changes due to the transition with the influences on the NTE. This symmetry change imposes certain constraints on Si-O-Si bond angles limiting the amount of variance in the structure with temperature and hence straying from the expected NTE trend. Secondly high temperature data becomes less precise as data collection becomes more difficult. Reasons for this include the heat softening the glue and glass on which the crystals were mounted leading to difficulties in crystal centering throughout the data collection. In addition the atoms vibrate more with

heat and the refinements become less accurate. So the only region we could examine was the NTE of the low temperature Pnmm phase.

Six data sets were collected between 133 K and 300 K at the CCLRC Synchrotron Radiation Source, Daresbury Laboratories, UK using the microcrystal X-ray diffractometer with a CCD detector. These were refined by least squares in Pnmm and a single crystal structure solved with an R-factor of 4.5% at 133K. These low temperature structures were used to explain the NTE behaviour.

Powder X-ray diffraction experiments were carried out to measure the extent of NTE. These experiments were carried out on a Stoe in-house X-ray diffractometer (Cu-K α radiation). The unit cells obtained from this data agreed in their trends with those from the single crystal data (see figure 4.15). However, because of the differences in absolute values obtained between the two methods, both the single crystal and powder unit cells for each temperature were used in the refinements. There were no qualitative differences between the results in terms of trends in atomic positions.

X-ray crystallography allows us to examine the change in average atomic position with temperature. It must be noted that I haven't looked very closely at dynamic reasons (i.e. phonons) for the effects although these are discussed.

One of the most important factors in previous studies of NTE materials has been the transverse vibrations of two co-ordinated atoms. All the oxygen atoms in zeolite structures are two co-ordinated, and transverse vibrations of these atoms can outweigh the expansion of individual Si-O bonds and lead to a decrease in distance between the two silicon atoms connected by the same oxygen atom. In ferrierite there are ten crystallographically independent Si-O-Si bond angles. Eight of the Si-Si

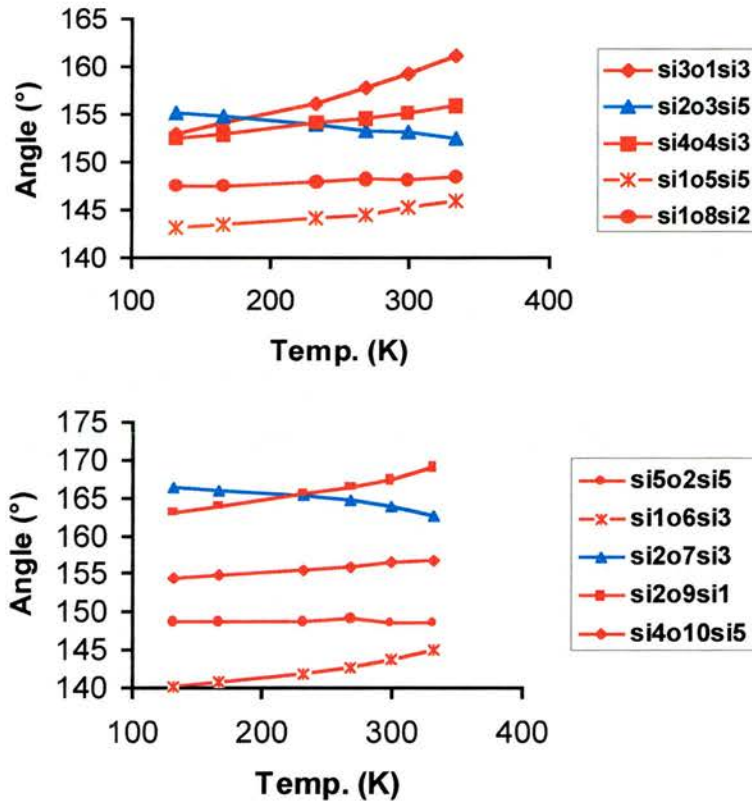


Figure 4.16 The variation of the Si-O-Si bond angles in the ferrierite structure with temperature. Ordinarily when temperature increase the Si-O-Si bond angle should decrease and this can be seen in red. However, Si2O7Si3 and Si2O3Si5 are both decreasing (shown in blue) which allows for the NTE behaviour.

distances increase slightly as expected with temperature (since bond distances become larger as vibrational energy increases with temperature), but two Si-Si distances decrease over the temperature range. Interestingly when we examine the Si-O-Si bond angles it can be seen that two of the angles decrease significantly (see

figure 4.16). It seems these two bond angles are wholly responsible for the NTE behaviour. They have values considerably higher than the other Si-O-Si angles (166° compared to 140°) and perhaps the reason for its ability to contract is the increased flexibility.

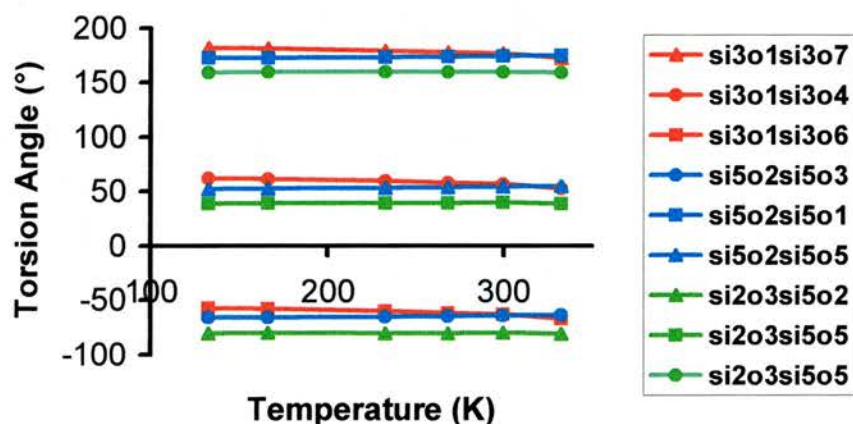


Figure 4.17 Plot of selected torsion angles to illustrate the consistency of the angle with temperature indicating its not of primary importance in the NTE behaviour of the Pnmm of ferrierite.

In previous studies the twisting of tetrahedra allowed for NTE behaviour and this would be reflected in the torsion angles as seen in the structure of IFR.¹⁰ However in ferrierite there is little change in any of the torsion angles (see figure 4.17). The NTE behaviour seems to be largely due to the decrease in the two bond angles as a result of the transverse vibrations.

For descriptive purposes the structure of ferrierite can be thought of as a layered structure along two of the crystallographic planes. Viewed down the *a*-axis we have layers of [5⁴] cages separated by a chain of alternating 10 MR and 6 MR along the *b*-axis direction. There are also layers of [5⁴] cages separated by 8MR when viewed down the 010 along the *b*-axis direction. These 10 and 8 MR are not simple to

describe, as they are not wholly symmetrical in character. In figure 4.18 it can be seen that one side of the ring is slightly larger than the other side. It can be thought of as egg-shaped.

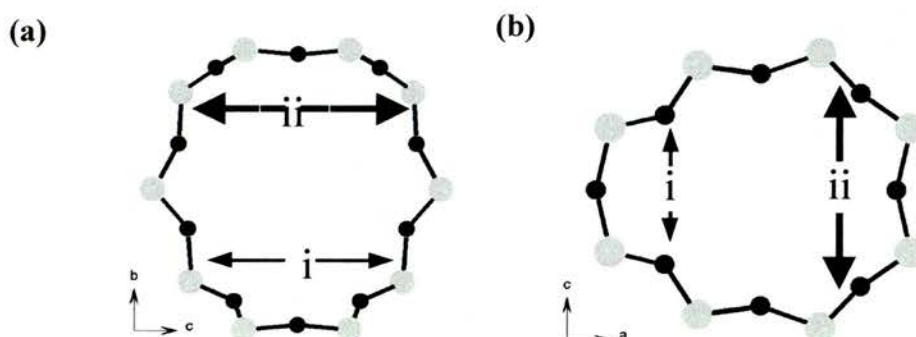


Figure 4.18 Illustration of the egg shapes of the channel systems; (a) 10MR and (b) 8MR. The short end is denoted *i*, and the large end is denoted *ii*.

The NTE behaviour seen along every crystallographic axis is a result of the shrinking of the large porous rings. It can be thought of as an expansion of the dense areas into the void space or the dense layers squashing into the free space (a little like when you press a sponge).

The *a*-axis is relatively simple to describe as seen in figure 4.19 and exhibits the smallest change over the temperature range. It contracts by 0.002 Å due to the squeezing of the 8 MR by the expanding layers. The 8 MR shrinks due to decrease in Si2-O7-Si3 angle leading to a contraction that outweighs all the other expansions.

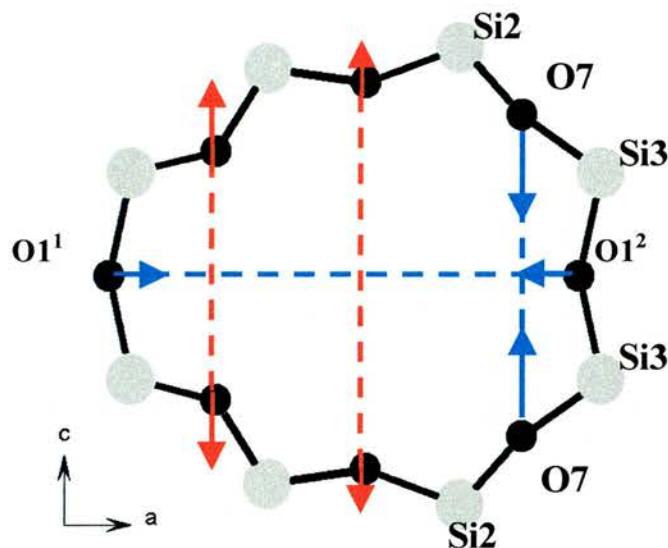


Figure 4.19 Illustration of the *a*-axis contraction – the blue and red arrows indicating components of motions leading to contractions and expansions respectively. The decrease in the Si2O7Si3 angle results in the shortening of the Si2-Si3 distance, which allows the contraction of the O1¹-O1² distance. A NTE of 0.02 Å is seen along the *a*-axis.

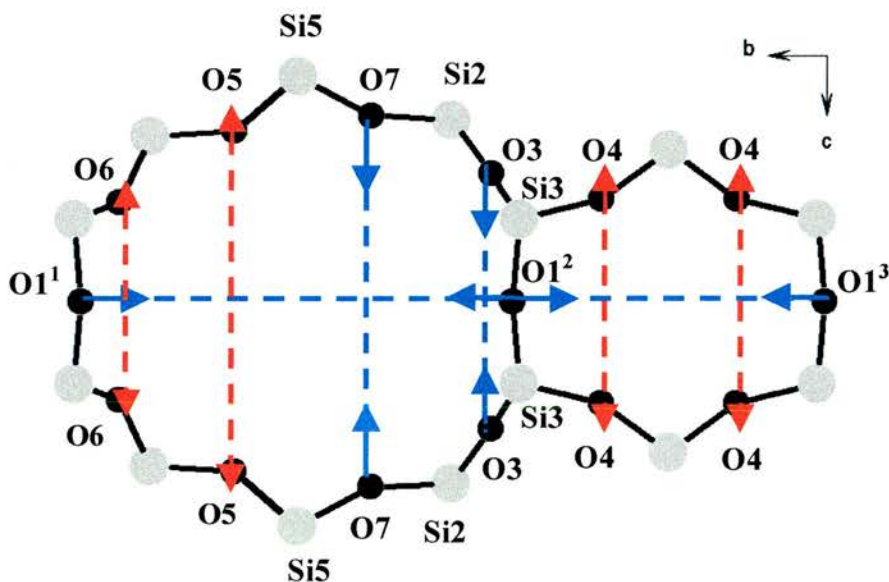


Figure 4.20 The *b*-axis contraction is illustrated above – the blue and red arrows indicate components of motions, parallel to the crystallographic axes, of atoms that lead to contractions and expansions respectively. The O1¹ to O1² contraction is allowed due to the decrease in Si5O7Si2 and Si2O3Si3 bond angles resulting in distances decreasing. The O1² to O1³ distance decreases through a combination of the previous bond angles decreasing and the expansion of the O4-O4 distance in the 6MR allowing the oxygens to move closer together. The overall decrease in the *b*-axis can be calculated using the cosine rule to calculate the O1¹ to O1³ distance, which contracts from 14.0636 Å at 133 K to 14.0562 Å at 333 K. A NTE of 0.073 Å along the *b*-axis.

This contraction occurs at the larger side of the ring and is probably due to the larger angle making this part of it more flexible. The ring closes at the large side and results in a contraction of 0.002 \AA along the a -axis. This agrees with NTE value obtained from the powder study.

The b -axis involves the squashing of the 10 MR as the layers expand. There are two Si-O-Si angles that result in shortening of the Si-O bond lengths as seen in figure 4.20. This results in the 10MR collapsing inwards at one end and a contraction along the b -axis. There is also a contribution to the NTE along the b -axis from the 6MR. The shortening of the Si-O bonds due to the decreasing bond angles at the large end of the 10MR allows space for the 6MR to contract into as it is squashed by the expanding small side of the 10MR. The combined interaction leads to a contraction of 0.0073 \AA along the b -axis that compares favourably with the powder value.

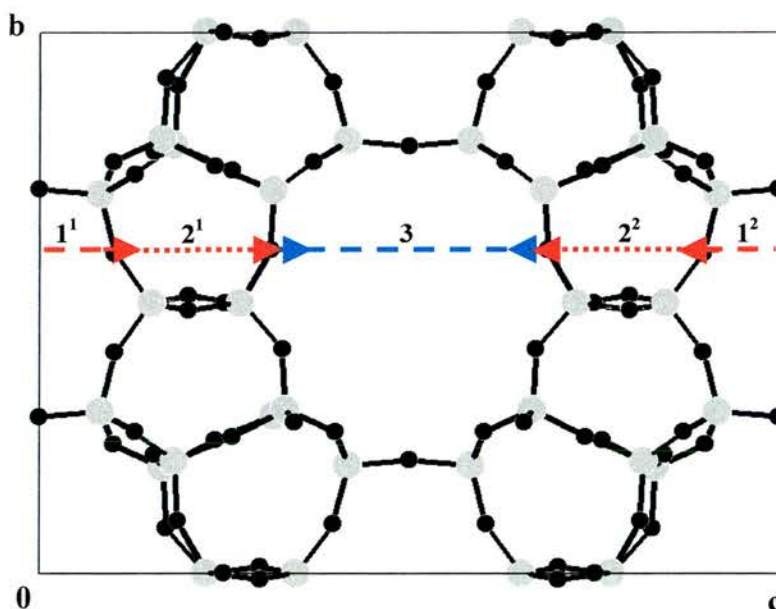


Figure 4.21 The c -axis contraction is illustrated above – the blue and red arrows indicate components of motions, parallel to the crystallographic axes, of atoms that lead to contractions and expansions respectively. There are 3 components to the NTE of the c -axis: the contraction of the 10MR (distance 3), minus the expansion of the 6MR (distance $1^1 + 1^2$), minus the expansion of the dense part (distance $2^1 + 2^2$). A calculated NTE of 0.04 \AA compared favourably with the measured 0.07 \AA when it is considered that it was assumed that all distances were on the same plane.

The movement of the layers together accounts for the *c*-axis contraction. This can be thought of in terms of the amount that either of the two large rings (10MR, 8MR) is squashed combined with how much the dense framework and 6MR expands in the *c* direction. In figure 4.21 the 10MR contraction is described. It is assumed that the atoms along *c*-axis are on the same plane to simplify what is otherwise a very complicated mathematical model. Yet again it is the two larger Si-O-Si angles which are collapsing allowing for the contraction.

4.4 Conclusions

Microcrystal X-ray diffraction experiments have provided an accurate probe of the structure of the as-made ferrierite and the changes in atomic position of calcined ferrierite with temperature.

This has allowed the location of the template and fluoride within the framework of the as-made ferrierite. This result is the first time that fluoride has been located crystallographically and confirmed by NMR in a purely siliceous ferrierite. New synthetic conditions have been reported which result in the incorporation of fluoride into the framework to counter balance the charge of the suggested protonated pyridine.

An evaluation of the thermal behaviour of ferrierite has revealed that it undergoes a phase transition between two regions of negative thermal expansion behaviour. This has important implications for applications in such materials since the material shows varying behaviour with temperature. These complications would probably mean that this material is not suitable for most negative thermal applications.

The mechanism of NTE displayed by ferrierite at low temperature is similar to that seen in many zeolites such as IFR¹⁰ or CHA¹¹. Most structures display NTE at least partly due to the effect of the transverse vibrations on distances between atoms

(where the transverse vibrations have enough energy that they can outweigh the individual expansions of Si-O bonds). However ferrierite shows this behaviour in regions of the framework, which contrast to that seen in a typical zeolite. For instance in both CHA and IFR the transverse vibrations, which result in NTE, are associated with Si-O-Si that bridge 6-rings. Whereas the transverse vibrations, responsible for the NTE of ferrierite, are associated with Si-O-Si angles which are non-bridging and associated with larger channel systems. Another difference is that the NTE of ferrierite seems to be solely due to transverse vibrations whereas, in other zeolites (including IFR and CHA) an additional mechanism where fairly rigid tetrahedra rotate cooperatively (rigid unit model), resulting in zeolite columns expanding, but production of NTE due to the decrease in distance between the columns. I would suggest that at high temperature ferrierite would display this behaviour as the egg shape of the channels responsible for the low temperature NTE will not be possible. Unfortunately very high temperature data collection is currently outwith the capability of station 9.8.

This work has led to a more thorough understanding of the properties of ferrierite. In addition it has revealed complications which need to be evaluated in all zeolites before considering them as materials for negative thermal expansion applications.

4.5 References

1. W.S. Wise and R.W. Tschernich, *Am. Mineral.*, 1976, **61**, 60.
2. R. Gramlich-Meier, W.M. Meier and B.K. Smith, *Zeit. Kristallogr.*, 1984, **169**, 201.
3. J. Haggin, *C&EN*, 1993, **October 25**, 30.
4. H. Gies and R. P. Gunawardane, *Zeolites*, 1987, **7**, 442

5. A. Kuperman, S. Nadimi, S. Oliver, G.A. Ozin, J.M. Garces and M.M. Olken, *Nature*, 1993, **365**, 239.
6. P.A. Vaughan, *Acta Crystallogr.*, 1966, **21**, 983.
7. A. Alberti and C. Sabelli, *Zeit. Kristallogr.*, 1987, **178**, 249.
8. R.E. Morris, S.J. Weigel, N.J. Henson, L.M. Bull, M.T. Janicke, B.F. Chmelka and A.K. Cheetham, *J. Am. Chem. Soc.*, 1994, **116**, 11849.
9. J. E. Lewis, C. C. Freyhardt and M.E. Davis, *J. Phys. Chem.*, 1996, **100**, 5039
10. L.A. Villaescusa, P. Lightfoot, S. J. Teat and R.E. Morris, *J. Am. Chem. Soc.*, 2001, **123**, 5453.
11. D.A. Woodcock, P. Lightfoot, L.A. Villaescusa, M.-J. Diaz-Cabañas and M.A. Cambor, *Chem. Mater.*, 1999, **11**, 2508.
12. P. Tschaufeser and S.C. Parker, *J. Phys. Chem.*, 1995, **99**, 10609.
13. M. T. Dove, *Am. Mineral.*, 1997, **82**, 213.
14. K. D. Hammonds, V. Heine and M.T. Dove, *J. Phys. Chem. B*, 1998, **102**, 1759.
15. K. Yamahara, K. Okazaki and K. Kawanura, *Catalysis Today*, 1995, **23**, 39.
16. J. M. Letoffe, B. F. Mentzen and P. Claudy, *Thermochimica Acta*, 1996, **288**, 1.
17. G.M Sheldrick, *Programs SHELXS-97 and SHELXL-97*, University of Gottingen, Germany, 1997.
18. A. P. Giddy, M. T. Dove, G. S. Pawley and V. Heine, *Acta Crystallographica*, 1993, **A49**, 697-703.
19. M.T. Dove, A.K.A. Pryde and D.A. Keen, *Mineralogical Magazine*, 2000, **64**, 267.
20. I. Bull, L.A. Villaescusa, S.J. Teat, M.A. Cambor, P.A. Wright, P. Lightfoot and R.E. Morris, *J. Am. Chem. Soc.*, 2000, **122**, 7128.

21. L.A. Villaescusa, P.S. Wheatley, I. Bull, P. Lightfoot and R.E. Morris, *J. Am. Chem. Soc.*, 2001, **123**, 8797.

Chapter 5 - ITQ-4

5.1 Introduction

This chapter outlines the importance of combining single-crystal synchrotron X-ray diffraction with low temperatures to accurately locate template positions and fluoride ions within zeolite frameworks (in this case the IFR framework). My primary aim was to understand the location of fluoride and templates within the framework. However the results showed a reduction in the framework symmetry from centrosymmetric to noncentrosymmetric which had important implications towards applications in nonlinear optics (NLO). An understanding of this structure is imperative if this zeolite (and other potential zeolites) are to be utilised as nonlinear optical materials. This underlined the importance of obtaining structural detail from such synchrotron single-crystal studies. In addition to this I demonstrate that this low temperature data collection allowed the accurate modelling of disorder in ITQ-4,

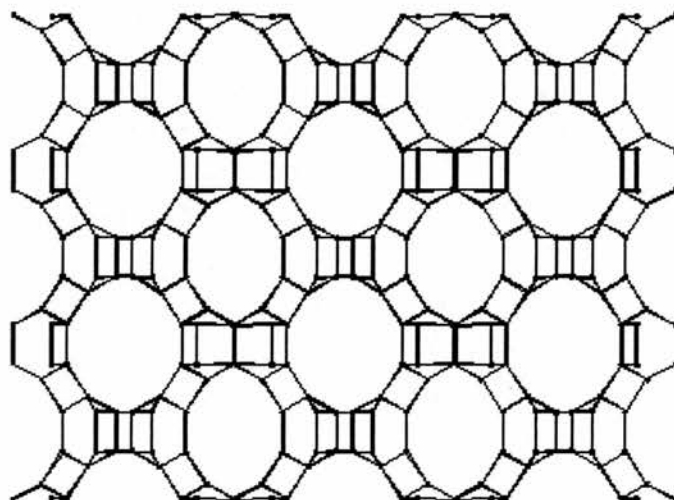


Figure 5.1 The one-dimensional 8 MR channels parallel to the c -axis, which is characteristic of the IFR topology.

which allows a greater understanding of host-guest relationships.

It has been known for a number of years that pure silica zeolite phases can be prepared hydrothermally in the presence of fluoride ions as mineralisers.¹ However, it was only recently that NMR and X-ray diffraction studies have indicated that F⁻ can interact strongly with the framework silicon atoms, giving rise to pentacoordinated [SiO_{4/2}F]⁻ in a number of pure silica phases.² Purely siliceous zeolite IFR can be prepared from fluoride-containing media using benzylquinuclidinium (BQ⁺) or benzyl-hydroxyquinuclidinium (BQoI⁺) cations as templating (structure-directing) agents.³ The structure of calcined IFR (i.e., where the template and fluoride have been thermally removed) was originally solved from powder X-ray diffraction data, and showed the framework topology to be centrosymmetric (monoclinic space group I2/m, a non standard setting of C2/m).⁴ The framework structure consists of small [4³5²6¹] cages linked together to form a unidimensional channel system (see figure 5.1). Further powder diffraction studies identified the fluoride ion positions in the as-made material as being inside the small cages and also identified possible template positions.³ However, because of the inherent problems of powder X-ray diffraction, further details of the structure could not be determined with any great precision.

Here I report the single-crystal structure of as-made ITQ-4 solved from synchrotron radiation.⁵ This reveals how fluoride, added as a mineraliser to a zeolite synthesis, leads to crystallisation in a polar noncentrosymmetric space group for zeolite IFR, a framework whose topological symmetry is centrosymmetric and therefore nonpolar. This also leads to a noncentrosymmetric ordering of the organic template molecules in the channels, which is vital if materials with good NLO properties are to be prepared.⁶⁻⁸ The reasons for this ordering can be traced to the

influence of the fluoride ion on the structure of the framework. I also show that this noncentrosymmetric ordering is independent of whether the template is or isn't hydroxylated, illustrating that no additional template-framework interactions (such as hydrogen bonding) influence the polar alignment. When the fluoride ions and templates are removed by calcination, the framework symmetry is centrosymmetric.

5.2 Experimental

5.2.1 Synthesis of ITQ-4

Samples of ITQ-4 were synthesised hydrothermally from a starting mixture of composition $\text{SiO}_2:0.5 \text{ SDA}: 0.5 \text{ HF}: 15 \text{ H}_2\text{O}$ by Villaescusa et al.³ This was heated at 150 °C in Teflon-lined stainless steel autoclaves rotated at 60 rpm for 12.5 days. The SDAs used were *N*-benzylquinuclidinium (see figure 5.2) or benzylhydroxyquinuclidinium cations. The solids were recovered by filtration, washing and drying.

5.2.2 Single-crystal data collection

Both the ITQ-4 materials (containing BQol and BQ), had single-crystal X-ray diffraction data collected on the Bruker AXS Smart CCD area-detector diffractometer at the high-flux microcrystal diffraction station at the CCLRC Synchrotron Radiation Source, Daresbury Laboratories, UK. The synchrotron beam was



Figure 5.2 Representational model of the organic cation *N*-benzylquinuclidinium. Drawing generated using the programme Weblab Viewer.

monochromated with a Si(111) bent crystal providing a constant wavelength, this is noted in table 5.1.

Data were collected at 200 K for [BQol,F]-ITQ-4 and solved in space group *I m*. Refinements of the centrosymmetric *I2/m* models against data collected were unsatisfactory. For example, in the [BQol,F]-ITQ-4 case at 200 K the refinement stopped with an agreement factor, R_1 , of approximately 10.7 % compared to the 5.07 % for the noncentrosymmetric *Im* model at the same temperature.

Table 5.1 Crystal data and structure refinement for [BQol,F]-ITQ-4 200K.

Identification code	[BQol,F]-ITQ-4 200 K	
Empirical formula	$C_{28}H_{40}F_2N_2O_{66}Si_{32}$	
Formula weight	2397.50	
Temperature	290(2) K	
Wavelength	0.69940 Å	
Crystal system	monoclinic	
Space group	<i>I m</i>	
Unit cell dimensions	$a = 18.513(3)$ Å	$\alpha = 90^\circ$.
	$b = 13.4326(18)$ Å	$\beta = 101.103(3)^\circ$.
	$c = 7.6841(10)$ Å	$\gamma = 90^\circ$.
Volume	$1875.1(4)$ Å ³	
Z	1	
Density (calculated)	2.123 Mg/m ³	
Absorption coefficient	0.424 mm ⁻¹	
F(000)	1216	
Crystal size	0.02 x 0.01 x 0.01 mm ³	
Theta range for data collection	1.86 to 29.86°.	
Index ranges	-25 ≤ h ≤ 26, -13 ≤ k ≤ 18, -10 ≤ l ≤ 10	
Reflections collected	6891	
Independent reflections	4618 [R(int) = 0.0310]	
Completeness to theta = 29.86°	91.8 %	
Max. and min. transmission	0.9958 and 0.9916	
Refinement method	Full-matrix least-squares on F ²	
Data / restraints / parameters	4618 / 220 / 350	
Goodness-of-fit on F ²	1.062	
Final R indices [I > 2σ(I)]	R1 = 0.0512, wR2 = 0.1294	

R indices (all data)	R1 = 0.0592, wR2 = 0.1346
Absolute structure parameter	0.3(3)
Largest diff. peak and hole	0.706 and -0.650 e.Å ⁻³

Full details of the structure determination can be found on the attached CD as Crystallographic Information Files. Full atomic coordinates, bond lengths and angles and thermal displacement parameters of the [BQoL,F]-ITQ-4 at 200 K are given in tables 5.2 to 5.4.

Table 5.2 Atomic coordinates and equivalent isotropic displacement parameters (Å²) for [BQoL,F]-ITQ-4 at 200 K. U(eq) is defined as one third of the trace of the orthogonalized U_{ij} tensor.

	x	y	z	U(eq)	Occupancy
Si(1)	0.2131(1)	0.3873(1)	0.2312(2)	0.011(1)	1.00000
Si(2)	0.2344(1)	0.3863(1)	-0.3505(2)	0.011(1)	1.00000
Si(3)	0.3746(1)	0.3854(1)	0.1848(2)	0.014(1)	1.00000
Si(4)	0.765(1)	0.3827(1)	-0.2976(2)	0.009(1)	1.00000
Si(5)	0.4763(1)	0.1147(1)	-0.1750(2)	0.007(1)	1.00000
Si(6A)	-0.0374(3)	0.1077(3)	0.0577(6)	0.014(1)	0.50000
O(1A)	0.0424(6)	0.1773(9)	0.0744(16)	0.009(3)	0.50000
O(14A)	-0.0797(8)	0.1513(14)	-0.1304(19)	0.030(5)	0.50000
O(16A)	-0.0593(5)	0.1428(7)	0.2393(11)	0.005(2)	0.50000
O(7A)	0.0069(9)	0.0000	0.0780(20)	0.019(2)	0.25000
Si(6B)	-0.0231(3)	0.1139(3)	0.0569(6)	0.013(1)	0.50000
O(1B)	0.0500(6)	0.1804(10)	0.0981(17)	0.010(3)	0.50000
O(14B)	-0.0704(7)	0.1469(11)	-0.1327(15)	0.017(3)	0.50000
O(16B)	-0.0696(6)	0.1302(9)	0.2096(13)	0.019(3)	0.50000
O(7B)	-0.0001(9)	0.0000	0.0490(20)	0.019(2)	0.25000
Si(7)	0.0648(1)	0.2947(1)	0.0589(2)	0.010(1)	1.00000
Si(8)	0.3846(1)	0.2963(1)	-0.1756(2)	0.012(1)	1.00000
O(2)	0.4020(2)	0.1812(3)	-0.1977(7)	0.020(1)	1.00000
O(3)	0.0454(2)	0.3231(4)	-0.1477(6)	0.014(1)	1.00000
O(4)	0.4014(3)	0.3222(4)	0.0325(6)	0.017(1)	1.00000
O(5)	0.3859(4)	0.5000	0.1433(11)	0.024(2)	0.50000
O(6)	0.0705(4)	0.5000	-0.2619(10)	0.016(1)	0.50000

O(8)	0.4531(3)	0.0000	-0.1754(8)	0.011(1)	0.50000
O(9)	0.2986(3)	0.3133(3)	-0.2592(7)	0.019(1)	1.00000
O(10)	0.1513(2)	0.3120(3)	0.1321(6)	0.017(1)	1.00000
O(11)	0.2888(3)	0.3590(4)	0.1764(7)	0.024(1)	1.00000
O(12)	0.1607(2)	0.3526(3)	-0.2826(6)	0.015(1)	1.00000
O(13)	0.0307(3)	0.3556(3)	-0.4921(6)	0.016(1)	1.00000
O(15)	0.0186(3)	0.3652(3)	0.1642(6)	0.019(1)	1.00000
O(17)	0.2184(3)	0.3753(2)	-0.5636(8)	0.023(1)	1.00000
O(18)	0.2544(3)	0.5000	-0.2919(10)	0.017(1)	0.50000
O(19)	0.1894(4)	0.5000	0.1727(9)	0.024(2)	0.50000
F(1)	-0.1208(5)	0.0384(6)	0.0148(13)	0.052(2)	0.50000
C(1)	0.1779(8)	0.0000	0.0027(17)	0.068(4)	0.50000
C(2)	0.2568(7)	0.0000	0.1093(19)	0.049(3)	0.50000
C(3)	0.2946(6)	0.0861(7)	0.1640(14)	0.066(3)	1.00000
C(4)	0.3615(5)	0.0890(6)	0.2696(13)	0.057(2)	1.00000
C(5)	0.3971(6)	0.0000	0.3192(16)	0.051(3)	0.50000
N(2)	0.1692(6)	0.0000	-0.1960(20)	0.073(4)	0.50000
C(7)	0.0914(8)	0.0261(12)	-0.2822(18)	0.100(10)	0.50000
C(8)	0.0802(9)	0.0272(11)	-0.4800(20)	0.108(8)	0.50000
C(6A)	0.2190(10)	0.0744(11)	-0.2622(18)	0.093(9)	0.50000
C(9A)	0.2076(11)	0.0740(12)	-0.4597(19)	0.114(8)	0.50000
O(2H)	0.0570(19)	0.1240(20)	-0.5450(30)	0.200(20)	0.25000
C(6B)	0.1859(10)	-0.1005(10)	-0.2659(17)	0.102(11)	0.50000
C(9B)	0.1731(10)	-0.1004(10)	-0.4651(18)	0.107(8)	0.50000
O(1H)	0.1169(18)	-0.1715(11)	-0.5340(30)	0.125(14)	1.00000
C(10)	0.1503(8)	0.0000	-0.5460(20)	0.088(4)	0.50000

Table 5.3 Bond lengths [\AA] and angles [$^\circ$] for [BQol,F]-ITQ-4 at 200 K.

Si(1)-O(17)#1	1.569(7)	O(16A)-Si(6A)-F(1)	87.6(5)
Si(1)-O(11)	1.585(5)	O(14A)-Si(6A)-F(1)	76.6(7)
Si(1)-O(10)	1.605(5)	O(7A)-Si(6A)-F(1)	87.5(6)
Si(1)-O(19)	1.616(3)	O(1A)-Si(6A)-F(1)	173.6(6)
Si(2)-O(9)	1.595(5)	Si(7)-O(1A)-Si(6A)	137.5(8)
Si(2)-O(17)	1.614(6)	Si(3)#4-O(14A)-Si(6A)	140.5(12)
Si(2)-O(12)	1.616(5)	Si(8)#5-O(16A)-Si(6A)	145.3(7)
Si(2)-O(18)	1.615(3)	Si(6A)#6-O(7A)-Si(6A)	121.9(11)
Si(3)-O(14A)#2	1.585(14)	O(7B)-Si(6B)-O(16B)	110.1(7)
Si(3)-O(5)	1.594(3)	O(7B)-Si(6B)-O(1B)	108.8(6)
Si(3)-O(4)	1.601(5)	O(16B)-Si(6B)-O(1B)	109.4(6)
Si(3)-O(14B)#2	1.625(12)	O(7B)-Si(6B)-O(14B)	109.5(7)
Si(3)-O(11)	1.616(5)	O(16B)-Si(6B)-O(14B)	110.5(6)
Si(4)-O(12)	1.594(5)	O(1B)-Si(6B)-O(14B)	108.5(6)
Si(4)-O(3)	1.597(5)	O(7B)-Si(6B)-F(1)	75.7(6)
Si(4)-O(6)	1.606(2)	O(16B)-Si(6B)-F(1)	66.4(5)
Si(4)-O(13)	1.612(4)	O(1B)-Si(6B)-F(1)	175.0(6)
Si(5)-O(8)	1.599(2)	O(14B)-Si(6B)-F(1)	71.5(6)
Si(5)-O(15)#3	1.609(4)	Si(7)-O(1B)-Si(6B)	131.9(8)
Si(5)-O(13)#2	1.614(4)	Si(3)#4-O(14B)-Si(6B)	148.0(10)
Si(5)-O(2)	1.620(5)	Si(6B)-O(16B)-Si(8)#5	150.9(8)
Si(6A)-O(16A)	1.598(9)	Si(6B)#6-O(7B)-Si(6B)	147.9(12)
Si(6A)-O(14A)	1.616(12)	O(1B)-Si(7)-O(15)	110.2(5)
Si(6A)-O(7A)	1.655(9)	O(1B)-Si(7)-O(10)	105.5(4)
Si(6A)-O(1A)	1.732(13)	O(15)-Si(7)-O(10)	109.4(3)
Si(6A)-F(1)	1.779(9)	O(1B)-Si(7)-O(3)	113.6(5)
O(1A)-Si(7)	1.641(13)	O(15)-Si(7)-O(3)	108.7(3)
O(14A)-Si(3)#4	1.585(14)	O(10)-Si(7)-O(3)	109.2(3)
O(16A)-Si(8)#5	1.562(9)	O(1B)-Si(7)-O(1A)	7.4(7)
O(7A)-Si(6A)#6	1.655(9)	O(15)-Si(7)-O(1A)	111.4(4)
Si(6B)-O(7B)	1.592(6)	O(10)-Si(7)-O(1A)	111.2(4)
Si(6B)-O(16B)	1.598(10)	O(3)-Si(7)-O(1A)	106.8(5)
Si(6B)-O(1B)	1.601(11)	O(16A)#3-Si(8)-O(2)	107.3(4)
Si(6B)-O(14B)	1.612(10)	O(16A)#3-Si(8)-O(4)	106.6(4)
Si(6B)-F(1)	2.044(9)	O(2)-Si(8)-O(4)	108.1(3)
O(1B)-Si(7)	1.599(13)	O(16A)#3-Si(8)-O(9)	116.4(4)
O(14B)-Si(3)#4	1.625(12)	O(2)-Si(8)-O(9)	107.4(3)
O(16B)-Si(8)#5	1.662(11)	O(4)-Si(8)-O(9)	110.7(3)
O(7B)-Si(6B)#6	1.592(6)	O(16A)#3-Si(8)-O(16B)#3	10.7(5)

Si(7)-O(15)	1.596(4)	O(2)-Si(8)-O(16B)#3	112.6(5)
Si(7)-O(10)	1.608(5)	O(4)-Si(8)-O(16B)#3	112.3(4)
Si(7)-O(3)	1.605(5)	O(9)-Si(8)-O(16B)#3	105.7(4)
Si(8)-O(16A)#3	1.562(9)	Si(8)-O(2)-Si(5)	135.1(3)
Si(8)-O(2)	1.596(5)	Si(4)-O(3)-Si(7)	142.1(3)
Si(8)-O(4)	1.607(5)	Si(3)-O(4)-Si(8)	144.5(3)
Si(8)-O(9)	1.614(5)	Si(3)-O(5)-Si(3)#7	149.8(6)
Si(8)-O(16B)#3	1.662(11)	Si(4)-O(6)-Si(4)#7	157.4(5)
O(5)-Si(3)#7	1.594(3)	Si(5)#6-O(8)-Si(5)	148.9(4)
O(6)-Si(4)#7	1.606(2)	Si(2)-O(9)-Si(8)	148.9(3)
O(8)-Si(5)#6	1.599(2)	Si(1)-O(10)-Si(7)	145.9(3)
O(13)-Si(5)#4	1.614(4)	Si(1)-O(11)-Si(3)	148.1(4)
O(15)-Si(5)#5	1.609(4)	Si(4)-O(12)-Si(2)	141.3(3)
O(17)-Si(1)#8	1.569(7)	Si(5)#4-O(13)-Si(4)	151.6(3)
O(18)-Si(2)#7	1.615(3)	Si(7)-O(15)-Si(5)#5	151.3(3)
O(19)-Si(1)#7	1.616(3)	Si(1)#8-O(17)-Si(2)	166.9(3)
F(1)-F(1)#6	1.033(15)	Si(2)-O(18)-Si(2)#7	142.1(4)
C(1)-N(2)	1.502(19)	Si(1)#7-O(19)-Si(1)	139.1(5)
C(1)-C(2)	1.531(18)	F(1)#6-F(1)-Si(6A)	121.5(3)
C(2)-C(3)	1.376(13)	F(1)#6-F(1)-Si(6B)	119.7(3)
C(2)-C(3)#6	1.376(13)	Si(6A)-F(1)-Si(6B)	2.5(3)
C(3)-C(4)	1.344(13)	N(2)-C(1)-C(2)	116.6(11)
C(4)-C(5)	1.382(10)	C(3)-C(2)-C(3)#6	114.5(12)
C(5)-C(4)#6	1.382(10)	C(3)-C(2)-C(1)	122.7(6)
N(2)-C(6B)	1.507(13)	C(3)#6-C(2)-C(1)	122.7(6)
N(2)-C(6B)#6	1.507(13)	C(4)-C(3)-C(2)	124.4(9)
N(2)-C(6A)	1.513(13)	C(3)-C(4)-C(5)	118.4(8)
N(2)-C(6A)#6	1.513(13)	C(4)#6-C(5)-C(4)	119.7(11)
N(2)-C(7)#6	1.506(13)	C(6B)-N(2)-C(6B)#6	127.1(15)
N(2)-C(7)	1.506(13)	C(6B)-N(2)-C(6A)	106.8(10)
C(7)-C(8)	1.493(16)	C(6B)#6-N(2)-C(6A)	26.9(11)
C(7)-C(6B)#6	2.00(3)	C(6B)-N(2)-C(6A)#6	26.9(11)
C(8)-O(2H)	1.431(10)	C(6B)#6-N(2)-C(6A)#6	106.8(10)
C(8)-C(10)	1.526(15)	C(6A)-N(2)-C(6A)#6	82.6(14)
C(8)-C(9B)#6	1.96(3)	C(6B)-N(2)-C(7)#6	83.0(12)
C(6A)-C(9A)	1.492(16)	C(6B)#6-N(2)-C(7)#6	107.1(9)
C(6A)-C(6A)#6	2.00(3)	C(6A)-N(2)-C(7)#6	126.7(13)
C(9A)-C(10)	1.510(15)	C(6A)#6-N(2)-C(7)#6	106.8(8)
C(9A)-C(9A)#6	1.99(3)	C(6B)-N(2)-C(7)	107.1(9)
C(6B)-C(9B)	1.503(16)	C(6B)#6-N(2)-C(7)	83.0(12)

C(6B)-C(7)#6	2.00(3)	C(6A)-N(2)-C(7)	106.8(8)
C(9B)-O(1H)	1.435(10)	C(6A)#6-N(2)-C(7)	126.7(13)
C(9B)-C(10)	1.510(15)	C(7)#6-N(2)-C(7)	26.9(12)
C(9B)-C(8)#6	1.96(3)	C(6B)-N(2)-C(1)	112.0(8)
C(10)-C(9B)#6	1.510(15)	C(6B)#6-N(2)-C(1)	112.0(8)
C(10)-C(9A)#6	1.510(15)	C(6A)-N(2)-C(1)	112.9(9)
C(10)-C(8)#6	1.526(15)	C(6A)#6-N(2)-C(1)	112.9(9)
O(17)#1-Si(1)-O(11)	110.8(3)	C(7)#6-N(2)-C(1)	110.8(11)
O(17)#1-Si(1)-O(10)	108.2(3)	C(7)-N(2)-C(1)	110.8(11)
O(11)-Si(1)-O(10)	108.0(3)	C(8)-C(7)-N(2)	112.6(12)
O(17)#1-Si(1)-O(19)	109.7(3)	C(8)-C(7)-C(6B)#6	90.4(8)
O(11)-Si(1)-O(19)	110.9(3)	N(2)-C(7)-C(6B)#6	48.5(6)
O(10)-Si(1)-O(19)	109.1(3)	O(2H)-C(8)-C(7)	109.9(12)
O(9)-Si(2)-O(17)	111.4(3)	O(2H)-C(8)-C(10)	108.5(11)
O(9)-Si(2)-O(12)	106.8(3)	C(7)-C(8)-C(10)	112.1(12)
O(17)-Si(2)-O(12)	107.5(3)	O(2H)-C(8)-C(9B)#6	76.5(16)
O(9)-Si(2)-O(18)	110.3(3)	C(7)-C(8)-C(9B)#6	89.9(8)
O(17)-Si(2)-O(18)	110.9(3)	C(10)-C(8)-C(9B)#6	49.3(6)
O(12)-Si(2)-O(18)	109.7(3)	C(9A)-C(6A)-N(2)	111.4(11)
O(14A)#2-Si(3)-O(5)	114.3(7)	C(9A)-C(6A)-C(6A)#6	89.8(7)
O(14A)#2-Si(3)-O(4)	107.6(7)	N(2)-C(6A)-C(6A)#6	48.7(7)
O(5)-Si(3)-O(4)	107.1(4)	C(6A)-C(9A)-C(10)	113.5(12)
O(14A)#2-Si(3)-O(14B)#2	6.5(10)	C(6A)-C(9A)-C(9A)#6	90.2(7)
O(5)-Si(3)-O(14B)#2	110.2(6)	C(10)-C(9A)-C(9A)#6	48.8(7)
O(4)-Si(3)-O(14B)#2	104.9(5)	C(9B)-C(6B)-N(2)	111.2(11)
O(14A)#2-Si(3)-O(11)	108.5(7)	C(9B)-C(6B)-C(7)#6	88.4(8)
O(5)-Si(3)-O(11)	111.8(3)	N(2)-C(6B)-C(7)#6	48.5(7)
O(4)-Si(3)-O(11)	107.2(3)	O(1H)-C(9B)-C(6B)	109.4(11)
O(14B)#2-Si(3)-O(11)	115.1(6)	O(1H)-C(9B)-C(10)	108.6(11)
O(12)-Si(4)-O(3)	107.7(3)	C(6B)-C(9B)-C(10)	113.3(11)
O(12)-Si(4)-O(6)	109.6(3)	O(1H)-C(9B)-C(8)#6	75.4(14)
O(3)-Si(4)-O(6)	108.8(3)	C(6B)-C(9B)-C(8)#6	91.3(8)
O(12)-Si(4)-O(13)	110.0(3)	C(10)-C(9B)-C(8)#6	50.0(7)
O(3)-Si(4)-O(13)	110.9(3)	C(9B)#6-C(10)-C(9B)	126.5(14)
O(6)-Si(4)-O(13)	109.8(3)	C(9B)#6-C(10)-C(9A)	27.7(11)
O(8)-Si(5)-O(15)#3	109.3(3)	C(9B)-C(10)-C(9A)	106.9(10)
O(8)-Si(5)-O(13)#2	111.3(3)	C(9B)#6-C(10)-C(9A)#6	106.9(10)
O(15)#3-Si(5)-O(13)#2	108.2(3)	C(9B)-C(10)-C(9A)#6	27.7(11)
O(8)-Si(5)-O(2)	108.0(3)	C(9A)-C(10)-C(9A)#6	82.4(14)
O(15)#3-Si(5)-O(2)	110.7(3)	C(9B)#6-C(10)-C(8)#6	105.4(9)

O(13)#2-Si(5)-O(2)	109.4(3)	C(9B)-C(10)-C(8)#6	80.7(12)
O(16A)-Si(6A)-O(14A)	120.8(8)	C(9A)-C(10)-C(8)#6	125.6(14)
O(16A)-Si(6A)-O(7A)	112.4(7)	C(9A)#6-C(10)-C(8)#6	105.5(9)
O(14A)-Si(6A)-O(7A)	123.2(9)	C(9B)#6-C(10)-C(8)	80.7(12)
O(16A)-Si(6A)-O(1A)	97.6(5)	C(9B)-C(10)-C(8)	105.4(9)
O(14A)-Si(6A)-O(1A)	97.5(7)	C(9A)-C(10)-C(8)	105.5(9)
O(7A)-Si(6A)-O(1A)	93.7(6)	C(9A)#6-C(10)-C(8)	125.6(14)
		C(8)#6-C(10)-C(8)	27.7(12)

Symmetry transformations used to generate equivalent atoms:

#1 x,y,z+1 #2 x+1/2,-y+1/2,z-1/2 #3 x+1/2,-y+1/2,z+1/2
 #4 x-1/2,-y+1/2,z+1/2 #5 x,-y+1,z #6 x,-y,z
 #7 x-1/2,-y+1/2,z-1/2 #8 x,y,z-1

Table 5.4 Anisotropic displacement parameters (\AA^2) for [BQoI,F]-ITQ-4 at 200 K.

The anisotropic displacement factor exponent takes the form: $-2\pi^2 [h^2 a^*{}^2 U_{11} + \dots +$

	$2 h k a^* b^* U_{12}]$					
	U_{11}	U_{22}	U_{33}	U_{23}	U_{13}	U_{12}
Si(1)	0.013(1)	0.013(1)	0.009(1)	-0.001(1)	0.004(1)	-0.001(1)
Si(2)	0.010(1)	0.010(1)	0.013(1)	0.001(1)	0.001(1)	0.002(1)
Si(3)	0.016(1)	0.012(1)	0.013(1)	0.000(1)	0.002(1)	-0.002(1)
Si(4)	0.009(1)	0.010(1)	0.008(1)	0.001(1)	0.002(1)	0.000(1)
Si(5)	0.011(1)	0.002(1)	0.008(1)	0.001(1)	0.005(1)	0.002(1)
Si(7)	0.014(1)	0.009(1)	0.007(1)	0.000(1)	0.003(1)	0.001(1)
Si(8)	0.009(1)	0.010(1)	0.018(1)	0.001(1)	0.002(1)	0.002(1)
O(2)	0.021(2)	0.010(2)	0.023(2)	-0.004(2)	-0.008(2)	0.008(1)
O(3)	0.019(2)	0.015(2)	0.011(2)	0.004(2)	0.007(2)	-0.001(2)
O(4)	0.020(2)	0.017(2)	0.013(2)	-0.002(2)	0.002(2)	0.004(2)
O(5)	0.026(3)	0.016(3)	0.028(4)	0.000	-0.001(3)	0.000
O(6)	0.022(3)	0.005(2)	0.022(3)	0.000	0.008(2)	0.000
O(8)	0.023(3)	0.000(2)	0.013(3)	0.000	0.010(2)	0.000
O(9)	0.010(2)	0.015(2)	0.030(3)	0.002(2)	0.001(2)	0.005(2)
O(10)	0.015(2)	0.016(2)	0.018(2)	-0.008(2)	-0.002(2)	-0.003(2)
O(11)	0.014(2)	0.031(3)	0.031(3)	-0.009(2)	0.014(2)	0.000(2)
O(12)	0.013(2)	0.015(2)	0.018(2)	0.003(2)	0.003(2)	0.003(1)
O(13)	0.017(2)	0.020(2)	0.008(2)	-0.004(1)	-0.007(1)	0.001(2)
O(15)	0.028(2)	0.016(2)	0.014(2)	-0.006(2)	0.011(2)	0.002(2)
O(17)	0.029(2)	0.028(1)	0.010(1)	-0.004(2)	0.002(1)	-0.003(2)
O(18)	0.009(2)	0.009(3)	0.029(4)	0.000	-0.007(2)	0.000

O(19)	0.040(4)	0.016(3)	0.015(3)	0.000	0.006(3)	0.000
F(1)	0.046(5)	0.034(4)	0.077(7)	-0.005(4)	0.014(5)	-0.006(3)
C(1)	0.059(8)	0.101(11)	0.047(7)	0.000	0.016(6)	0.000
C(2)	0.049(7)	0.029(5)	0.059(8)	0.000	-0.010(6)	0.000
C(3)	0.079(7)	0.042(5)	0.072(6)	0.000(4)	0.003(5)	0.028(5)
C(4)	0.067(5)	0.030(3)	0.070(6)	-0.015(4)	0.002(4)	-0.009(3)
C(5)	0.033(5)	0.075(8)	0.046(6)	0.000	0.012(5)	0.000
N(2)	0.061(8)	0.077(9)	0.073(9)	0.000	-0.006(7)	0.000
C(7)	0.059(9)	0.180(30)	0.057(8)	-0.025(13)	0.013(8)	0.017(15)
C(8)	0.112(12)	0.150(20)	0.061(9)	0.001(13)	0.019(11)	0.036(12)
C(6A)	0.110(19)	0.110(20)	0.057(9)	0.038(11)	0.015(11)	-0.049(15)
C(9A)	0.155(17)	0.130(20)	0.068(11)	-0.018(13)	0.049(14)	-0.032(15)
O(2H)	0.250(50)	0.190(40)	0.150(30)	0.020(30)	0.010(40)	0.120(30)
C(6B)	0.180(30)	0.024(8)	0.086(11)	-0.010(7)	-0.002(18)	0.029(14)
C(9B)	0.170(20)	0.061(10)	0.093(12)	-0.034(9)	0.037(15)	0.018(11)
O(1H)	0.160(30)	0.128(19)	0.065(17)	0.054(17)	-0.040(20)	-0.020(20)
C(10)	0.101(11)	0.113(10)	0.057(7)	0.000	0.029(7)	0.000

5.2.3 Solid state NMR

Solid state NMR experiments were performed on a Bruker DMX-400 spectrometer operating at a frequency of 74.495 MHz for ^{29}Si . A Bruker 4 mm MAS probe, capable of spinning up to 15 kHz with the frequency controlled to ± 5 Hz was used. The ^{29}Si chemical shifts were referenced to tetramethylsilane (TMS) using Q_8M_8 (the octamer $\text{Si}_8\text{O}_{12}[\text{OSi}(\text{CH}_3)_3]_8$) or octadecasil as an external secondary reference. ^{29}Si CP MAS spectra were collected with a contact time of 3 ms, a recycle time of 1.5 s ($\sim 1.25 T_1$), and an acquisition time of about 50 ms using a spin rate of 15 kHz.

5.3 Results and Discussion

5.3.1 Structure of [BQol,F]-ITQ-4

Refinements of the centrosymmetric $I2/m$ models against data collected using both [BQ,F]-IFR and [BQol,F]-IFR crystals were unsatisfactory. For example, in the [BQol,F]-IFR case at 200 K, the refinement stopped with the agreement factor, R_1 , of approximately 9% (see attached CD). Lowering of the symmetry to polar space group Im produced a much-improved refinement with a final residual agreement factor of 5.07%. The difference in agreement factors between the centrosymmetric and polar space group refinements is clearly significant, and indicates that the polar model is the correct one. In addition, the hydrogen atoms of the template were located in the difference Fourier maps and further refinement revealed only very small residual electron density peaks that could not be modelled as any extra/disordered template atoms.

A powdered sample of [BQol,F]-IFR frequency doubled the light from a Nd:YAG (1064 nm) laser to such an extent that the resulting green light (532 nm) was visible to the naked eye. This demonstration of NLO properties is proof that the crystal structure is indeed noncentrosymmetric. In addition the refinement is very well behaved especially when the disorder is modelled.

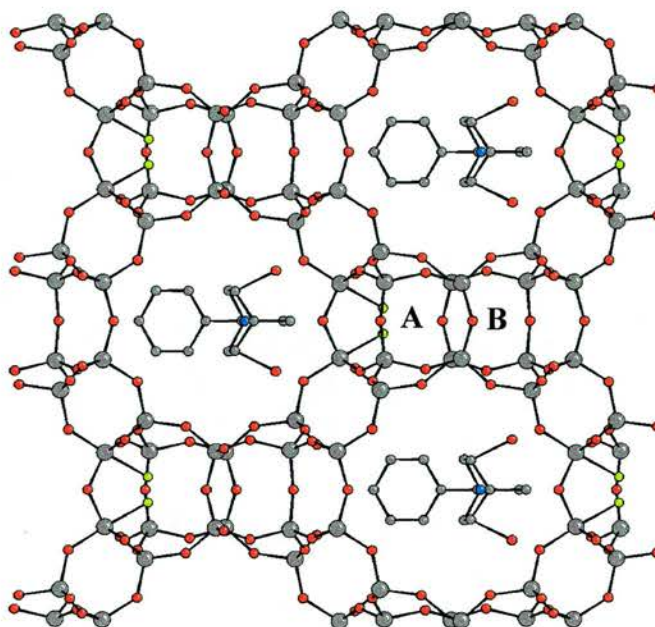


Figure 5.3 The average structure of [BQol,F]-ITQ-4 viewed parallel to the *c*-axis. The Si, O, and F atoms of the framework are depicted as grey, red, and green spheres, respectively. The BQol⁺ cation template occupies the 8MR channel with C, N and O atoms shown in grey, blue and red, respectively. The [4³5²6¹] cage occupied by F⁻ is labelled **A**, the unoccupied cage **B**. The disorder of the template has still to be resolved in this figure.

The average model, illustrated in Figure 5.3, indicated that the template is ordered in a noncentrosymmetric arrangement within the pores of the zeolite. It also revealed that the fluorine, as part of a pentacoordinate [SiO_{4/2}F]⁻ unit, is only present in one of the two possible [4³5²6¹] cages, although disordered over two possible sites within the cage it occupies. Single-crystal X-ray diffraction experiments on the [BQ,F]-IFR sample, despite the crystals being of slightly lesser quality than the [BQol,F]-IFR ones, show the same arrangement of template and fluoride ions. The reason the fluoride and templates order in such a fashion is not altogether apparent at first sight. There is no obvious significant interaction between neighbouring templates that might account for the ordering, such as the dipolar “head-to-tail” interactions that can order *p*-nitroaniline inside zeolite pores.⁹ In fact, the location of the template is more likely to be affected by the position of the fluoride ion, since it is the negative charge

on the F^- that balances the positive charge on the cationic template. As the templates are asymmetric, with the positive charge localised primarily on the quinuclidine unit, it is this end of the template that is most strongly attracted by a region of negative charge. This strong, electrostatic interaction will lead to the template being oriented so that the quinuclidinium end of the molecule is as close to the negatively charged F^- ion as possible. The alternative orientation of the template, which is necessarily present in the centrosymmetric model, will have the positive charge on the template significantly further away from the fluoride ions. The arrangement of the template is therefore intimately connected with the ordering of the fluoride ions into the $[4^35^26^1]$;

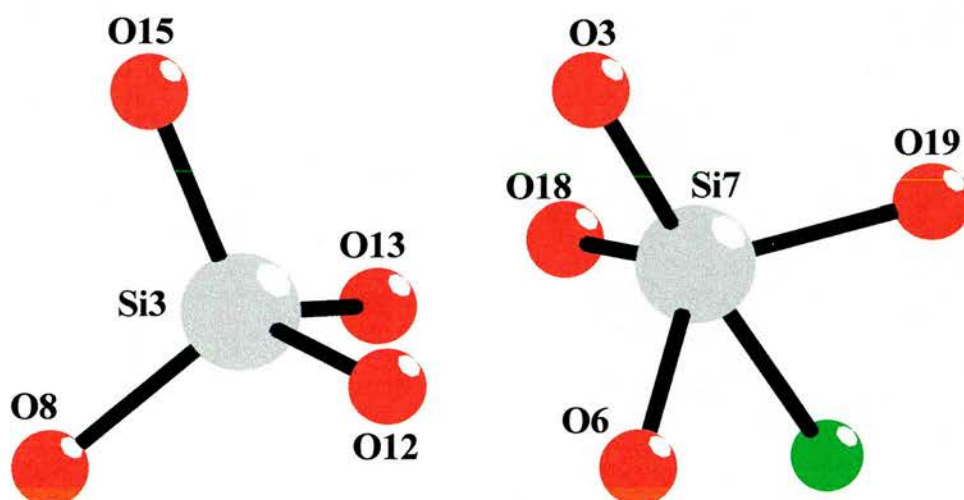


Figure 5.4 The tetrahedral coordination polyhedron around Si3 (left) and the almost trigonal bipyramidal coordination around Si7 (right). These two silicon atoms would be equivalent by symmetry in the centrosymmetric $I2/m$ model. Selected distances and angles (at 200 K) : Si7-F, 1.918(9) Å; Si7-O3, 1.654(5) Å; Si7-O6, 1.617(3) Å; O3-Si7-F1, 177.2(3) °; O3-Si7-O6, 100.6(3) °. Si3-O bond distances are in the range of 1.587(5) to 1.627(5), and O-Si3-O angles range from 107.9(3) to 111.7(3).

an ordered arrangement of F^- will lead to ordered templates (or vice versa).

Why the fluoride orders into only one of the two possible $[4^35^26^1]$ cages is thus the important question in determining the structure of the as-made IFR materials. There are two possible reasons for this. One is a simple electrostatic effect in which

the negatively charged $[\text{SiO}_{4/2}\text{F}]^-$ units arrange themselves as far away from each other as possible, which requires ordering of the fluoride ions. The second reason can be found in the distortions of the framework structure caused by the presence of the five-coordinated $[\text{SiO}_{4/2}\text{F}]^-$ units. Figure 5.4 shows the coordination polyhedra around two of the eight crystallographically independent silicon atoms in the polar structure. These two silicon atoms are equivalent by symmetry in the centrosymmetric $I2/m$ model, and the large differences in bond lengths and angles between these two polyhedra adds significant weight to the assertion that the polar model is the correct one. The Si7-centered polyhedron is much nearer a trigonal bipyramid than a tetrahedron, as would be expected for the $[\text{SiO}_{4/2}\text{F}]^-$ unit. The

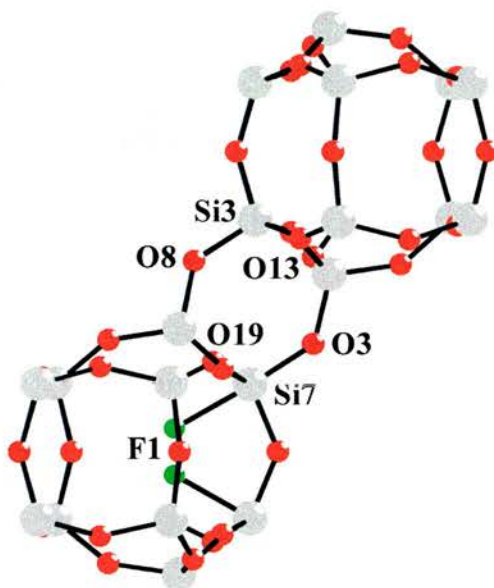


Figure 5.5 Two $[4^3 5^2 6^1]$ cages from the structure of $[\text{BQol},\text{F}]\text{-ITQ-4}$ linked by a single four-ring unit, illustrating the presence of fluorine in only the lower cage. Si, O, and F shown as grey, red and green, respectively.

coordination around the seven other silicon atoms in the structure is tetrahedral.

The distortion of the Si7 coordination polyhedron also has an effect on the single four-ring (containing oxygens O3, O8, O13, and O19) that links the [4³5²6¹] cages together (Figure 5.5). The fluorine in the lower cage causes the O3-Si7-O19 to be distorted from tetrahedral (109.7°) to 102.8(3)°, and the Si7-O3 distance is elongated to 1.627(5) Å, which is about 0.04 Å longer than that expected for a Si-O bond. The presence of another fluorine in the upper cage, bonded to Si3, would distort the single four-ring even further by similarly decreasing the O8-Si3-O13 angle to an extent that would strain the small four-ring unit to an unfavourable degree. Therefore, accommodation of F⁻ into one cage necessarily requires that the next is empty, the next-but-one then has F⁻ present, and so on. A combination of this distortion and electrostatic effects probably causes the fluorine to order into one cage only, which in turn causes ordering of the templates, thus requiring the overall polar noncentrosymmetric structure. However, in the growth of the crystal, the +ve template (SDA) and -ve fluoride must act in a complementary manner. It is probably not just the fluoride that is involved but a more complex process.

5.3.2 Disorder

Some potential inaccuracies could be seen in the previous crystallographic model. For instance the organic template had some rather large thermal parameters, which is suggestive of an inaccurate model. This was consolidated by the suggestion of peak splitting within the results of the refinement. In addition there was evidence that the fluorine is dynamically disordered which would in turn have an influence on the framework. Here we discuss the disorder and suggest a more accurate crystallographic model.

The crystallographic model reported in the last section clearly shows that the fluorine is disordered over two positions within each cage. This is in agreement with

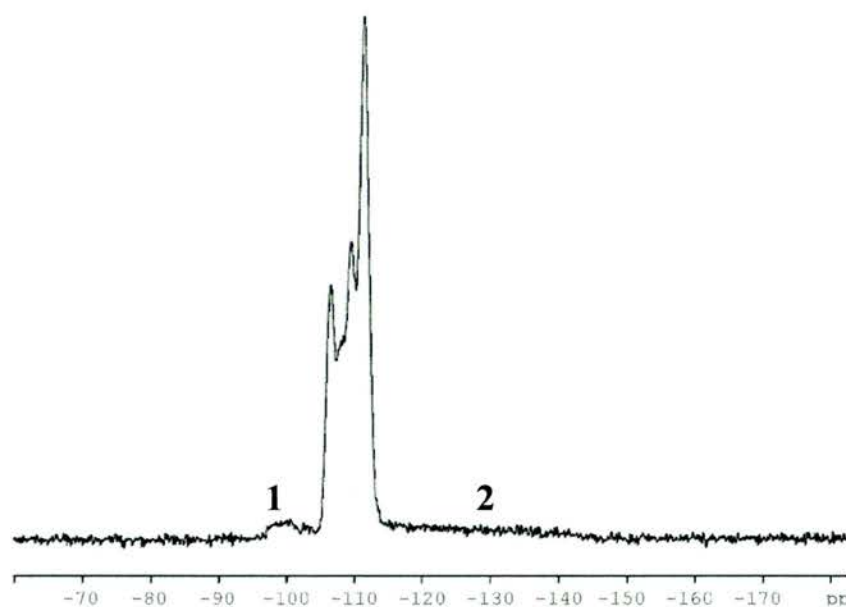


Figure 5.6 ^{29}Si CPMAS NMR spectra of [BQol,F]-ITQ-4 showing broad peaks at -100 (peak 1) and -130 (peak 2) ppm indicative of the dynamic disorder of fluoride ions in silica zeolites.

the NMR studies of Koller et al.² They reported broad ^{29}Si NMR signals (see figure 5.6) between -140 and -150 ppm that are indicative of the dynamic motion of the fluoride ion between the two crystallographic sites. This results in molecular reorientation within the framework between tetrahedral silicon (SiO_4) and pentacoordinated silicon (SiO_4F) as shown in figure 5.7.

This dynamic disorder of the fluoride raised the possibility of the template showing similar disorder. In fact the refinement seen in the previous section suggested that some of the carbon sites (with large thermal parameters) might be split into two sites indicative of this disorder. This disorder was successfully modelled crystallographically (see figure 5.7) and refined to give an agreement factor, R_1 , of 5.12%. Figure 5.7 shows that the quinuclidine moiety of the template is disordered whereas the benzyl moiety is static, which is in agreement with the ^{13}C CP/MAS NMR studies of similar template disorder within SSZ-42.¹⁰

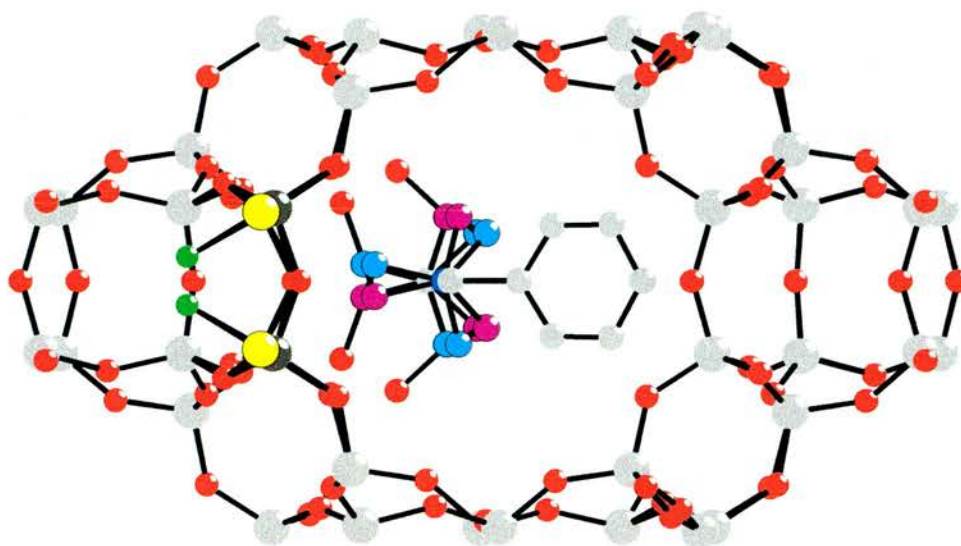


Figure 5.7 Molecular reorientation of the quinuclidine moiety of the template within the 12 MR channel of ITQ-4. The two disordered orientations are coloured purple and cyan. There is also some disorder within the framework due to the dynamic disorder of the fluoride ion, in the form tetrahedral silicon (dark grey) and pentacoordinated silicon (yellow).

Several restraints were placed upon this model to allow a stable refinement (see the instruction file on attached CD). Essentially this model provided a more accurate portrayal of the molecular reorientation of the quinuclidine moiety of the template, which was modelled as two positions. The FREE instruction was used to ensure that neither of the two positions bonded with each other. In addition the shape of the quinuclidine was maintained by restraining 1,2 and 1,3 distances using the SADI and DFIX commands.

The accuracy of this disordered model is corroborated by the improved thermal parameters of the quinuclidine moiety as shown in figure 5.8. It can clearly be seen that the atoms with large thermal parameters of the average structure (figure 5.8a) and be split into two atom positions with smaller thermal parameters (figure 5.8b). Prior to the modelling of this disorder it proved difficult to accurately locate the hydroxyl group on the template. The C-O distance was 1.751 Å, which is

unrealistically long. However in the disordered model four possible hydroxyl positions refine to give more realistic C-O distances of 1.436(1) and 1.430(1) Å. This again promotes the accuracy of the disordered model. It should be noted that although this new model is more accurate it is not perfect, suggested by the overlapping of the thermal parameters belonging to the split atoms (i.e. cyan and purple overlap). This indicates that the atoms are not isolated, and therefore some unmodelled disorder remains. These may be multiple positions for the quinuclidine end of the template, and the disorder may be dynamic at 200 K. Further investigations of this would require more involved NMR experiments.

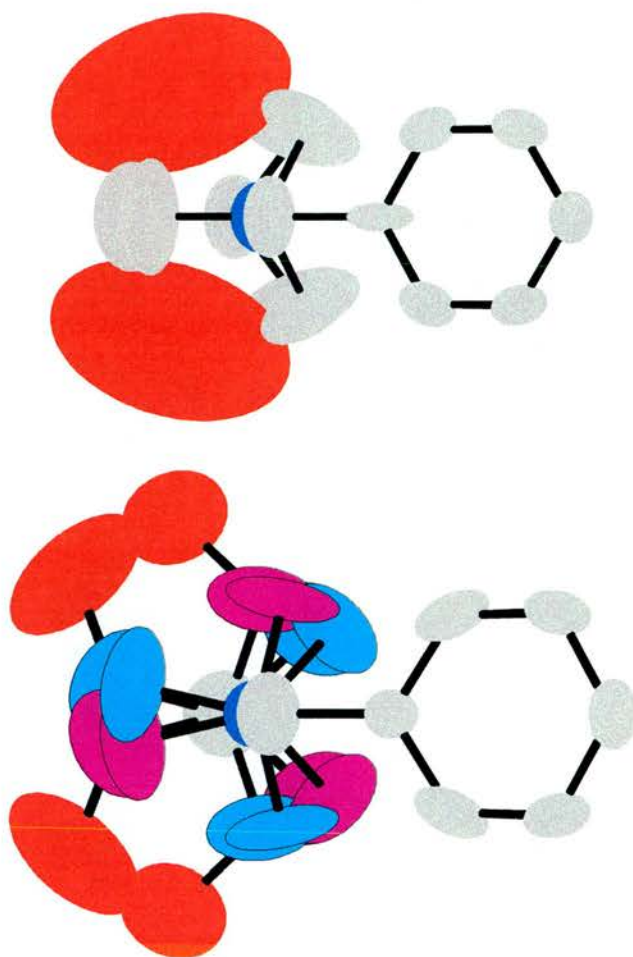


Figure 5.8 Illustrations of the thermal motion of the atoms in (a) average structure model and (b) the structure that molecular reorientation model. It can be seen that the thermal ellipsoids are larger for the atoms before splitting than they are after indicating that the model that accounts for disorder is more accurate. In addition the oxygen (red) becomes more stable and the bond distance becomes more realistic. C-O distance in (a) is 1.751 Å compared 1.436(1) and 1.430(1) Å in (b).

5.4 Conclusions

This work represents the first time that the distortion of a silica zeolite framework by fluoride has been experimentally verified using diffraction. That the presence of fluoride causes such a dramatic change of symmetry and ordering of the organic template may have an effect on how future optically active composite materials of this kind are designed. In fact this work was instrumental in developing similar studies in other zeolites. My colleagues went on to examine the fluoride positions in ITQ-9, which is described by the STF framework.¹¹ The topology of STF is very similar to that of IFR (ITQ-4) and provided a great comparison to enable a greater understanding of the details of fluoride incorporation. It was postulated that there would be similar fluoride ordering in these structures. Both have framework symmetry $I2/m$, and similar framework density. The differences between the structures are mainly in the nature of the cages themselves: IFR contains $[4^35^26^1]$ cages, where as STF contains $[4^15^26^2]$ cages and the pores are defined by 12MR and 10MR respectively.

Both structures do contain fluoride as part of a trigonal bipyramidal $[\text{SiO}_4\text{F}]$ unit. However, NMR and single-crystal XRD studies revealed that the major difference between these two structures was the long-range ordering of fluoride ions in the framework as shown in figure 5.9. In IFR the fluoride was dynamically disordered over two positions within every second $[4^35^26^1]$ cage. In contrast to the static disorder of one fluoride within every $[4^15^26^2]$ cage seen in STF. Although STF lacks the alternating occupied/empty cage sequence required in IFR for electrostatic and geometric reasons, it can be seen that the fluoride in each neighbouring cage is positioned to maximise the distance between fluoride ions. So in both cases the reasons for this ordering can be traced back to electrostatic and geometric

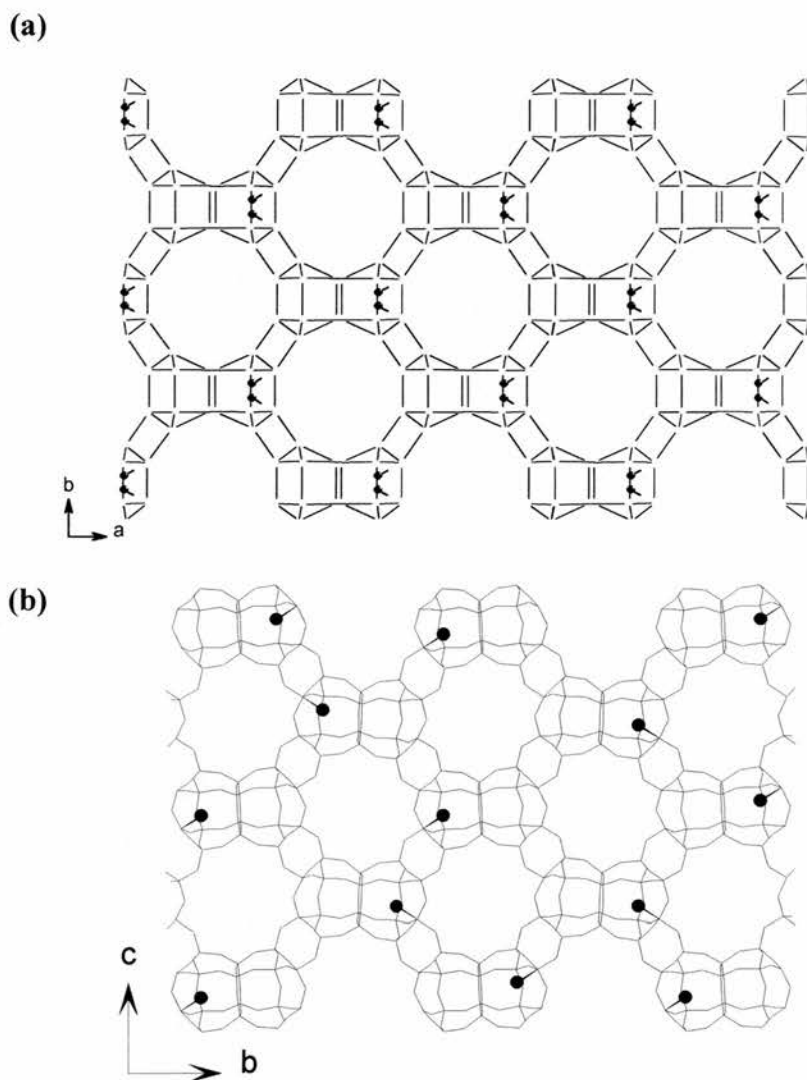


Figure 5.9 The arrangement of fluoride ions (black spheres) in zeolites (a) IFR and (b)STF. Both structures contain only one of any two fused cages occupied by fluoride and no 4MR with more than one fluoride ions attached to it. The differences between STF and the situation in IFR is the intracage ordering of fluoride ions in STF means there is no requirement for strict alternation of empty/filled cages in the crystallographic c -direction.

requirements to keep fluoride ions from being too close to one another and having only one fluoride attached to a 4MR at one time.

In addition crystallographic and NMR studies have confirmed the dynamic disorder of the fluoride ion which probably causes the cooperative molecular reorientation of the framework and template.

In chapter 6 the substitution of metal ions with different oxidation state into zeolite frameworks reveals another method of charge balancing. Further work relevant to ITQ-4 could compare an aluminosilicate ITQ-4 with the fluoride model presented here. I would hope that the aluminosilicate ITQ-4¹² would be centrosymmetric since there would be no ordering of charge within the framework. This would consolidate the theory that fluoride plays an important role in the imposition of polarity on the centrosymmetric zeolite.

5.5 References

1. H. Kessler, J. Patarin and C. Schott-Darie, *In Advanced Zeolite Science and Applications*, J.C. Jansen, M. Stöcker, H.G. Karge and J. Weitkamp Eds., Elsevier, Amsterdam, 1994, 75.
2. H. Koller, A. Wölker, L.A. Villaescusa, M.J. Diaz-Cabañas, S. Valencia and M.A. Camblor, *J. Am. Chem. Soc.*, 1999, **121**, 3368.
3. P.A. Barrett, M.A. Camblor, A. Corma, R.H. Jones and L.A. Villaescusa, *J. Phys. Chem. B*, 1998, **102**, 4147.
4. P.A. Barrett, M.A. Camblor, A. Corma, R.H. Jones and L.A. Villaescusa, *Chem. Mater.*, 1997, **9**, 1713.
5. I. Bull, L.A. Villaescusa, S.J. Teat, M.A. Camblor, P.A. Wright, P. Lightfoot and R.E. Morris, *J. Am. Chem. Soc.*, 2000, **122**, 7128.
6. J. Caro, G. Finger, J. Kornatowski, J. Richter-Mendau, L. Werner and B. Zibrowius, *Adv. Mater.*, 1992, **4**, 273.
7. J.B. Parise and T.E. Gier, *Chem. Mater.*, 1992, **4**, 1065.
8. B. Borecka-Bednarz, A.V. Bree, B.O. Patrick, J.R. Scheffer and J. Trotter, *Can. J. Chem.*, 1998, **76**, 1616.

9. G. Reck, F. Marlow, J. Kornatowski, W. Hill and J. Caro, *J. Phys. Chem.*, 1996, **100**, 1698.
10. C.-Y. Chen, L.W. Finger, R.C. Medrud, C.L. Kibby, P.A. Crozier, I.Y. Chan, T.V. Harris, L.W. Beck and S.I. Zones, *Chem. Eur. J.*, 1998, **4**, 1312.
11. L.A. Villaescusa, P.S. Wheatley, I. Bull, P. Lightfoot and R.E. Morris, *J. Am. Chem. Soc.*, 2001, **123**, 8797.
12. L.A. Villaescusa, P.A. Barrett, M. Kalwei, H. Koller and M.A. Cambor, *Chem. Mater.*, 2001, **13**, 2332.

Chapter 6 - Disordered Structures

6.1 Introduction

The previous two chapters have illustrated the importance of understanding the structures of zeolites. Knowledge of the template positions, fluoride location and framework symmetry is essential in gaining information on the properties of these materials.¹ Many zeolites contain a certain degree of disorder due to the framework flexibility and its symmetry. In the past this limited the amount of structural information that could be gained from crystallography due to difficulties in finding the templates and other molecules (such as fluoride) within the zeolite frameworks. However the combination of the cryostream with microcrystal diffraction has led to some of these issues being resolved. This chapter reports the template positions in Si-chabazite and MAPO-17 (magnesium aluminium phosphate-17). In addition the location of fluorine in chabazite is reported. The comparison of these two zeolites is very interesting as they demonstrate different ways of charge balancing. Both involve the incorporation of cationic templates within their associated channels and so need a source of negative charge. In chabazite this is provided by the incorporation of fluoride into the framework, as seen previously in both ferrierite and ITQ-4. Where as MAPO-17 has substituted Mg^{2+} for Al^{3+} in order to provide charge balancing.

Dent and Smith² first solved the crystal structure of chabazite in 1958. More recently Pluth et al.³ solved the single-crystal structure of SAPO-chabazite in R-3. This work reported the charge coupling between the framework and the templating ammonium species. However due to the disorder associated with the high symmetry of the framework it was difficult to locate the encapsulated organic species from their

crystallographic data. Further advances were made using synchrotron radiation enabling the solution of the single-crystal structure of AlPO₄-CHA in 1994.⁴ Cambor and co workers presented the structure and synthesis of SiO₂ chabazite in 1998.⁵ The elemental analysis of the as-made chabazite indicated the presence of fluoride, however they only solved the structure of the calcined version from powder. Therefore a number of unknowns still remain. The locations of the template and fluoride could yield information imperative to our understanding of this structure. Here I report the single-crystal structure showing the location of the disordered template species and fluoride in the as-made SiO₂ chabazite. In addition I present the ²⁹Si and ¹⁹F NMR to confirm the presence of fluorine.

MAPO-17 belongs to the aluminium phosphate family of zeotype materials, it is characterised by its Erionite structure topology. This has a three-dimensional system of 8 MR channels running perpendicular to the *c*-axis as illustrated in figure 6.2. The framework is described as hexagonal and has a unit cell of *a*=13.3, *c*=15.1 Å and $\gamma=120^\circ$ in space group P6₃/mmc. Pluth et al. solved the structure of as-made AlPO-17 containing piperdine as the templating agent.⁶ He I report the single-crystal structure of as-made MAPO-17 containing propylene-diquinuclidium as a templating agent.

6.2 Experimental

6.2.1 Single-crystal XRD

The crystals of chabazite and MAPO-17 were both very small (10x10x5 and 10x10x10 μm respectively), so diffraction data were collected using a Bruker AXS SMART CCD area detector diffractometer on the high flux microcrystal-diffraction facility (station 9.8) of the SRS at Daresbury. Both experiments used X-ray

wavelength 0.7107 Å selected by a horizontally focussing silicon (111) monochromator and vertically focussed by a cylindrically bent palladium-coated zerodur mirror. Corrections were made for the synchrotron beam intensity decay as part of the standard inter-frame scaling procedures. Details of the chabazite and MAPO-17 data collections and structures are given in tables 6.1 and 6.2 respectively.

Table 6.1. Crystal data and structure refinement for SiO₂ chabazite.

Identification code	chabazite	
Empirical formula	C ₃₉ H ₂₄ F ₃ N ₃ O ₇₂ Si ₃₆	
Formula weight	2754.85 g	
Temperature	150 K	
Wavelength	0.71073 Å	
Crystal system	Trigonal	
Space group	R-3	
Unit cell dimensions	a = 13.4902(10) Å	α = 90°.
	b = 13.4902(9) Å	β = 90°.
	c = 14.7578(11) Å	γ = 120°.
Volume	2325.9(3) Å ³	
Z	1	
Density (calculated)	1.967 Mg/m ³	
Absorption coefficient	0.610 mm ⁻¹	
F(000)	1386	
Crystal size	0.01 x 0.01 x 0.01 mm ³	
Theta range for data collection	2.22 to 30.09°.	
Index ranges	-18 ≤ h ≤ 17, -8 ≤ k ≤ 19, -20 ≤ l ≤ 7	
Reflections collected	3220	
Independent reflections	1400 [R(int) = 0.0156]	
Completeness to theta = 30.09°	92.6 %	
Max. and min. transmission	0.9970 and 0.9939	
Refinement method	Full-matrix least-squares on F ²	
Data / restraints / parameters	1400 / 23 / 84	
Goodness-of-fit on F ²	1.150	
Final R indices [I > 2σ(I)]	R1 = 0.0593, wR2 = 0.1662	
R indices (all data)	R1 = 0.0648, wR2 = 0.1699	
Largest diff. peak and hole	0.779 and -0.969 e.Å ⁻³	

Table 6.2 Crystal data and structure refinement for MAPO-17.

Identification code	MAPO-17	
Empirical formula	$C_{4.25} H_5 A_{12.25} N_{0.50} O_9 P_{2.25}$	
Formula weight	337.48 g	
Temperature	293(2) K	
Wavelength	0.71073 Å	
Crystal system	Hexagonal	
Space group	P 63/m	
Unit cell dimensions	$a = 13.180(2)$ Å	$\alpha = 90^\circ$.
	$b = 13.180(2)$ Å	$\beta = 90^\circ$.
	$c = 15.409(3)$ Å	$\gamma = 120^\circ$.
Volume	2318.1(7) Å ³	
Z	8	
Density (calculated)	1.934 Mg/m ³	
Absorption coefficient	0.618 mm ⁻¹	
F(000)	1352	
Crystal size	0.10 x 0.10 x 0.10 mm ³	
Theta range for data collection	2.22 to 30.42°.	
Index ranges	-17<=h<=18, -18<=k<=18, -20<=l<=16	
Reflections collected	16329	
Independent reflections	2288 [R(int) = 0.0695]	
Completeness to theta = 30.42°	94.1 %	
Max. and min. transmission	0.9407 and 0.9407	
Refinement method	Full-matrix least-squares on F ²	
Data / restraints / parameters	2288 / 3 / 107	
Goodness-of-fit on F ²	1.115	
Final R indices [I>2sigma(I)]	R1 = 0.0844, wR2 = 0.2176	
R indices (all data)	R1 = 0.1120, wR2 = 0.2311	
Largest diff. peak and hole	1.352 and -0.864 e.Å ⁻³	

6.2.2 Solid state NMR

MAS NMR experiments were carried out on the as-made chabazite using the EPSRC Solid-State NMR Service (Durham) on a Varian Unityplus 200 MHz spectrometer. ^{19}F NMR spectra were obtained using an acquisition time of 10 ms, relaxation time of 10 s and a contact time of 1 ms. Two runs were collected using spin rates of 11.44 kHz and 13.4 kHz to help identify real peaks. ^{29}Si were obtained using a spinning rate of 4 kHz, acquisition time of 10 ms, relaxation time of 1 s, and a contact time of 1 ms.

6.3 Results and discussion

6.3.1 Structure of chabazite

The final unit cell of *N,N,N*-trimethyladamantammonium-SiO₂-chabazite (TMAda⁺-SiCHA) refined to values of $a=13.4902(10)$ Å and $c=14.7578(11)$ Å at a temperature of 150 K. The model refined in space group, R-3 to give an R-factor of 5.93 %. Full atomic coordinates, bond lengths and angles and thermal displacement parameters are given in tables 6.3 to 6.5.

Table 6.3. Atomic coordinates and equivalent isotropic displacement parameters (Å²) for TMAda⁺-SiCHA. U(eq) is defined as one third of the trace of the orthogonalised U_{ij} tensor.

	x	y	z	U(eq)	Occupancy
Si(1)	0.4374(1)	0.1039(1)	0.7293(1)	0.012(1)	1.00000
Si(2)	0.6665(1)	0.1038(1)	0.7294(1)	0.012(1)	1.00000
O(1)	0.5468(1)	0.935(1)	0.7024(1)	0.018(1)	1.00000
O(2)	0.3331(1)	0.0138(1)	0.6666(1)	0.017(1)	1.00000
O(3)	0.4608(1)	0.2305(1)	0.7082(1)	0.023(1)	1.00000
O(4)	0.4007(1)	0.0674(1)	0.8334(1)	0.019(1)	1.00000
F(1)	0.5686(14)	0.3436(14)	0.8034(12)	0.019(3)	0.08200
F(2)	0.5672(16)	0.2246(16)	0.8030(13)	0.025(4)	0.08200
C(1)	0.3333	-0.3333	0.6469(3)	0.042(3)	0.16667
C(2)	0.2695(6)	-0.2687(6)	0.7846(4)	0.155(8)	0.50000
C(3)	0.3951(5)	-0.2116(7)	0.8189(5)	0.092(4)	0.50000
C(4)	0.2710(6)	-0.2697(6)	0.6783(4)	0.082(3)	0.50000
N(1)	0.3333	-0.3333	0.5441(4)	0.110(7)	0.16667
C(5)	0.3842(5)	-0.4038(5)	0.5104(5)	0.146(8)	0.50000

Table 6.4 Bond lengths (Å) and angles (°) for TMAda⁺-SiCHA.

Si(1)-O(1)	1.6009(18)	O(3)-Si(1)-F(2)	67.3(6)
Si(1)-O(3)	1.6042(18)	O(4)-Si(1)-F(2)	75.1(5)
Si(1)-O(4)	1.6132(17)	O(2)-Si(1)-F(2)	176.2(6)
Si(1)-O(2)	1.6136(16)	O(1)-Si(2)-O(3)#1	110.17(9)

Si(1)-F(2)	2.012(18)	O(1)-Si(2)-O(2)#2	106.53(9)
Si(2)-O(1)	1.5992(18)	O(3)#1-Si(2)-O(2)#2	108.85(10)
Si(2)-O(3)#1	1.6031(19)	O(1)-Si(2)-O(4)#3	111.49(10)
Si(2)-O(2)#2	1.6088(18)	O(3)#1-Si(2)-O(4)#3	112.19(10)
Si(2)-O(4)#3	1.6100(17)	O(2)#2-Si(2)-O(4)#3	107.37(9)
Si(2)-F(1)#1	2.025(18)	O(1)-Si(2)-F(1)#1	74.5(5)
O(2)-Si(2)#4	1.6088(18)	O(3)#1-Si(2)-F(1)#1	67.6(5)
O(3)-Si(2)#5	1.6031(19)	O(2)#2-Si(2)-F(1)#1	176.3(5)
O(4)-Si(2)#6	1.6100(17)	O(4)#3-Si(2)-F(1)#1	75.2(5)
F(1)-Si(2)#5	2.025(18)	Si(2)-O(1)-Si(1)	149.88(13)
C(1)-N(1)	1.517(7)	Si(2)#4-O(2)-Si(1)	143.01(13)
C(1)-C(4)	1.543(7)	Si(2)#5-O(3)-Si(1)	150.00(13)
C(1)-C(4)#8	1.543(7)	Si(2)#6-O(4)-Si(1)	144.33(11)
C(1)-C(4)#9	1.543(7)	N(1)-C(1)-C(4)	107.5(3)
C(2)-C(3)#9	1.542(8)	N(1)-C(1)-C(4)#8	107.5(3)
C(2)-C(3)	1.554(7)	C(4)-C(1)-C(4)#8	111.4(3)
C(2)-C(4)	1.568(7)	N(1)-C(1)-C(4)#9	107.5(3)
C(3)-C(2)#8	1.542(8)	C(4)-C(1)-C(4)#9	111.4(3)
C(4)-C(4)#2	1.511(8)	C(4)#8-C(1)-C(4)#9	111.4(3)
C(4)-C(4)#4	1.511(8)	C(3)#9-C(2)-C(3)	105.4(9)
N(1)-C(5)#8	1.507(7)	C(3)#9-C(2)-C(4)	108.7(5)
N(1)-C(5)#9	1.507(7)	C(3)-C(2)-C(4)	108.3(5)
N(1)-C(5)	1.507(7)	C(2)#8-C(3)-C(2)	114.2(8)
O(1)-Si(1)-O(3)	110.24(9)	C(1)-C(4)-C(2)	108.6(5)
O(1)-Si(1)-O(4)	111.39(10)	C(2)#2-N(1)-C(5)#8	114.3(3)
O(3)-Si(1)-O(4)	112.15(10)	C(5)#8-N(1)-C(5)#9	109.7(3)
O(1)-Si(1)-O(2)	106.66(9)	C(5)#8-N(1)-C(5)	109.7(3)
O(3)-Si(1)-O(2)	108.88(10)	C(5)#9-N(1)-C(5)	109.7(3)
O(4)-Si(1)-O(2)	107.29(8)	C(5)#8-N(1)-C(1)	109.3(3)
O(1)-Si(1)-F(2)	74.8(6)	C(5)#9-N(1)-C(1)	109.3(3)
		C(5)-N(1)-C(1)	109.3(3)

Symmetry transformations used to generate equivalent atoms:

#1 $-y+1, x-y, z$ #2 $y+2/3, -x+y+1/3, -z+4/3$ #3 $x-y+1/3, x-1/3, -z+5/3$
 #4 $x-y-1/3, x-2/3, -z+4/3$ #5 $-x+y+1, -x+1, z$ #6 $y+1/3, -x+y+2/3, -z+5/3$
 #7 $-x+2/3, -y-2/3, -z+4/3$ #8 $-x+y+1, -x, z$ #9 $-y, x-y-1, z$

Table 6.5 Anisotropic displacement parameters (Å) for TMAda⁺-SiCHA. The anisotropic displacement factor exponent takes the form:

$$-2\pi^2[h^2a^{*2}U_{11}+\dots+2hka^*b^*U_{12}]$$

	U ₁₁	U ₂₂	U ₃₃	U ₂₃	U ₁₃	U ₁₂
Si(1)	0.014(1)	0.014(1)	0.011(1)	0.001(1)	0.001(1)	0.008(1)
Si(2)	0.009(1)	0.013(1)	0.011(1)	0.001(1)	0.000(1)	0.005(1)
O(1)	0.014(1)	0.023(1)	0.022(1)	-0.001(1)	-0.001(1)	0.012(1)
O(2)	0.015(1)	0.018(1)	0.016(1)	-0.003(1)	-0.006(1)	0.007(1)
O(3)	0.027(1)	0.013(1)	0.034(1)	0.005(1)	0.012(1)	0.013(1)
O(4)	0.023(1)	0.022(1)	0.009(1)	-0.001(1)	0.001(1)	0.009(1)

The structure of the chabazite framework has been reported in space group R-3m. The reduction in symmetry to R-3 can be explained by the incorporation of the TMAda⁺ template. The chabazite framework is composed of 6-rings stacked in the sequence AABBC. The double 6-rings (D6R) are connected by 4-rings to produce the chabazite cage. These cages have six 8-ring windows. Figure 6.2a shows the template occluded within the framework (within the CHA cage). The positive charge from the template is charge balanced by the presence of fluorine in the D6R of the framework as shown in figure 6.2b.

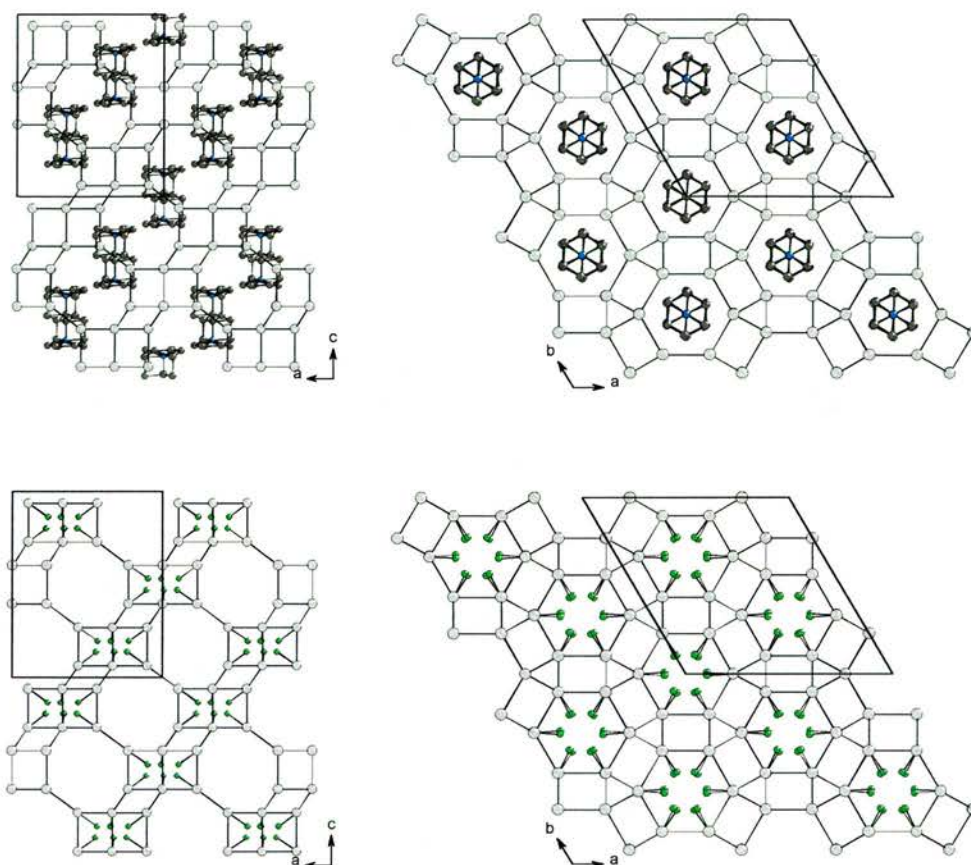


Figure 6.2 Single-crystal structures of as-synthesised Si-CHA with the unit cell outlined. Oxygen has been removed for clarity. Si is light grey, fluorine is grey, nitrogen is blue and carbon is dark grey. (a) Shows the template positions viewed down the *b* and *c* axes. (b) Shows the location of the fluorine in the double six ring viewed down the *b* and *c* axes.

Figure 6.3a illustrates the location of fluorine with respect to the template containing chabazite cage. It can be seen that the template is disordered over two directions within the chabazite cage - it can point either up or down (see figure 6.3c). The fluorine also demonstrates disorder within the double 6-ring as shown in figure 6.3b.

To accurately model the template disorder a number of restraints (see instruction file on attached CD) had to be placed upon the template in order to maintain its shape and prevent bonding between each of the two separate positions. Restraining the 1,2

and 1,3 distances on the template using DFIX and SADI commands maintained its shape. Where as FREE commands prevented bonding between either of the individual templates.

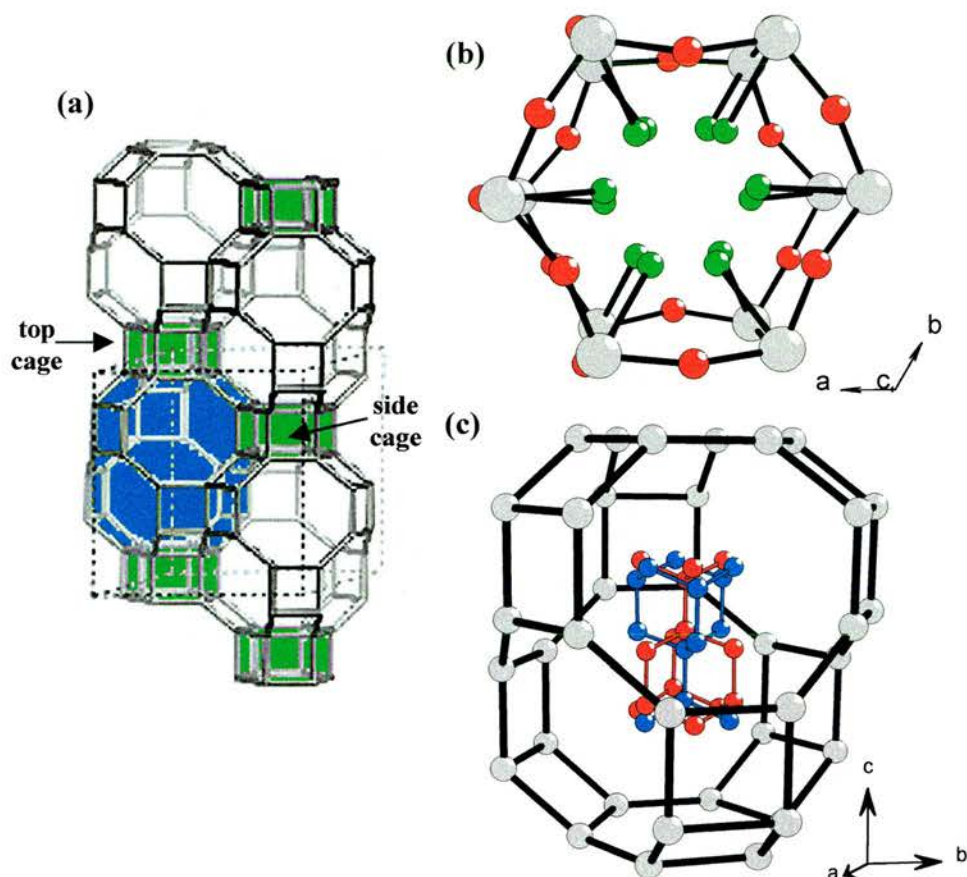


Figure 6.3 (a) An illustration of the fluorine location (green) with respect to the template containing chabazite cage (blue). (b) The fluorine is disordered within the double 6-ring where silicon is grey, oxygen is red and fluorine is green. (c) The two disordered positions of the template are shown in red and blue within the chabazite cage. Oxygen has been removed for clarity.

Eight D6Rs surround each chabazite cage and so the positive charge of the template has eight potential regions of negative charge to interact with. This is the same as saying that each template interacts with four areas of negative charge since the nitrogen of each template resides in opposite halves of the cage (i.e. the template can either point up or down). These four D6Rs can be subdivided into two groups as shown in figure 6.3a - the D6R that is situated at the top of the cage and the three D6Rs which surround the cage. The nitrogen to fluorine distance from the top D6R

varies in the range of 5.3 to 6.2 Å. Whereas the nitrogen to fluorine distance from one of the side D6Rs varies from 6.5 to 8 Å. This would suggest that the positive charge of the template is more strongly associated with the negative charge residing in the top D6R than the side D6Rs. However it is more likely the template's positioning over the two directions is due to the positive charge of the template interacting with the negative charge on the top or bottom half of the cage as a whole and not due to any single D6R.

For simplicity I have charge-balanced this structure by assigning equal fluorine and nitrogen content. However, Cambor et al.⁵ reported the presence of $\text{Si}(\text{OSi})_3\text{OH}$ defect groups and suggested a composition of $[\text{C}_{13}\text{H}_{24}\text{NF}_{0.5}]_3[\text{Si}_{36}\text{O}_{72}(\text{OH})_{1.5}]$. The ^{29}Si MAS NMR spectrum of $\text{TMAda}^+\text{-SiCHA}$ agrees with this model (see figure 6.4). There are two bands at δ -99.4 and -110.7. The first relating to the defect groups ($\text{Si}(\text{OSi})_3\text{O}^-$ and $\text{Si}(\text{OSi})_3\text{OH}$) and the second to the $\text{Si}(\text{OSi})_4$ species. There is no

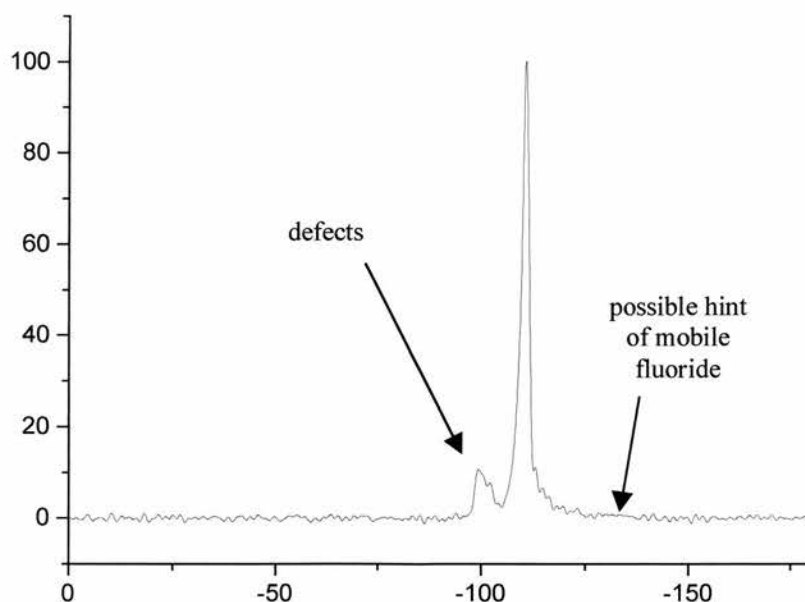


Figure 6.4 ^{29}Si MAS NMR spectrum of as-made [Pyr,F]-Si-CHA.

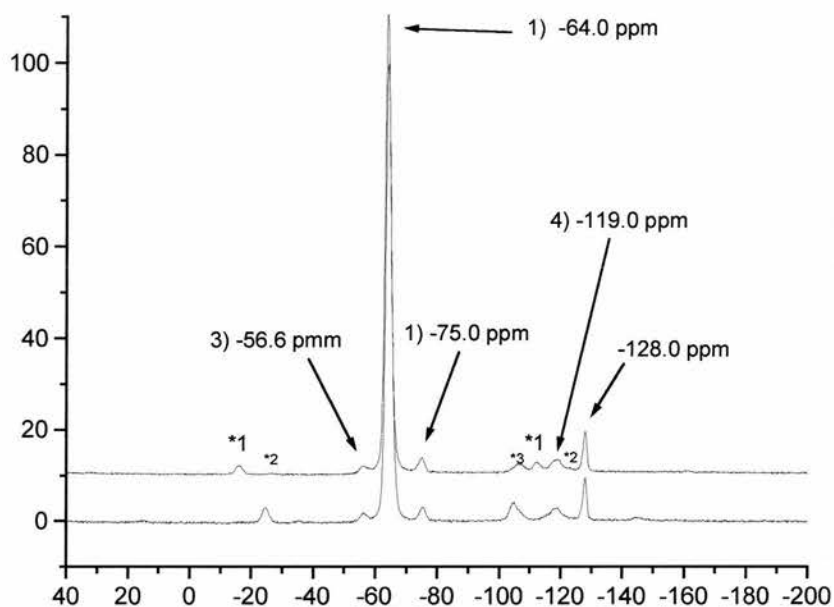


Figure 6.5 ^{19}F MAS NMR spectrum of as-made [Pyr,F]-Si-CHA.

obvious evidence of the presence of fluoride in the ^{29}Si NMR. However the ^{19}F MAS NMR shows a major peak at -64.0 ppm (see figure 6.5). This value is within the reported range for fluoride in siliceous zeolites prepared in fluoride medium (-60 to -80 ppm/ CFCl_3 according to structure type).⁷

This detailed structure investigation of as-made Si-CHA outlines the location and interactions of the negative charge associated with the framework fluoride, with that of the cationic template occluded in the CHA framework. In addition I have reported the complexity of host-guest relationships due to the additional presence of framework defects.

6.3.2 Structure of MAPO-17

The final unit cell of propylene-diquinuclidium-MAPO-17 (PdQ-MAPO-17) refined to values of $a=13.1800(20)$ Å and $c=15.4090(30)$ Å. The model refined in P63/m to give an R-factor of 8.44 %. Full atomic coordinates, bond lengths and angles and thermal displacement parameters are given in tables 6.5 to 6.8.

Table 6.6 Atomic coordinates and equivalent isotropic displacement parameters (Å²) for PdQ-MAPO-17. $U(\text{eq})$ is defined as one third of the trace of the orthogonalised

	U_{ij} tensor.			$U(\text{eq})$	Occupancy
	x	y	z		
P(1)	0.4253(1)	0.0901(1)	0.7500	0.019(1)	0.50000
P(2)	0.2436(1)	0.0051(1)	0.4007(1)	0.024(1)	1.00000
Al(1)	0.4208(2)	0.3289(2)	0.7500	0.020(1)	0.50000
Al(2)	0.2376(1)	0.0048(1)	0.6017(1)	0.028(1)	1.00000
O(1)	0.4581(5)	0.2182(4)	0.7500	0.038(1)	0.50000
O(2)	0.2818(4)	0.0064(4)	0.4938(2)	0.043(1)	1.00000
O(4)	0.2021(4)	0.1155(4)	0.6108(3)	0.045(1)	1.00000
O(5)	0.3412(4)	0.3209(4)	0.6563(3)	0.047(1)	1.00000
O(6)	0.1234(3)	-0.1360(4)	0.6237(3)	0.046(1)	1.00000
O(7)	0.3560(3)	0.0293(4)	0.6692(2)	0.037(1)	1.00000
O(3)	0.5355(5)	0.0824(6)	0.7500	0.042(1)	0.50000
C(1)	0.3811(16)	0.7902(17)	0.5657(15)	0.165(7)	0.16667
C(2)	0.3333	0.6667	0.4357(19)	0.133(9)	0.16667
C(3)	0.3878(18)	0.7925(19)	0.4767(17)	0.176(8)	0.16667
N(1)	0.3333	0.6667	0.5990(20)	0.164(9)	0.16667
C(4)	0.3240(150)	0.7480(70)	0.6650(50)	0.240(70)	0.16667
C(5)	0.2880(80)	0.7030(90)	0.7500	0.320(40)	0.33333

Table 6.7 Bond lengths (Å) and angles (°) for PdQ-MAPO-17.

P(1)-O(3)	1.506(5)	O(3)-P(1)-O(1)	109.1(3)
P(1)-O(7)#1	1.514(4)	O(7)#1-P(1)-O(1)	110.4(2)
P(1)-O(7)	1.514(4)	O(7)-P(1)-O(1)	110.4(2)
P(1)-O(1)	1.519(5)	O(5)#2-P(2)-O(6)#3	108.9(3)

P(2)-O(5)#2	1.505(4)	O(5)#2-P(2)-O(4)#2	111.2(3)
P(2)-O(6)#3	1.513(4)	O(6)#3-P(2)-O(4)#2	108.5(3)
P(2)-O(4)#2	1.517(4)	O(5)#2-P(2)-O(2)	107.2(3)
P(2)-O(2)	1.518(4)	O(6)#3-P(2)-O(2)	110.4(2)
Al(1)-O(3)#4	1.729(5)	O(4)#2-P(2)-O(2)	110.5(3)
Al(1)-O(1)	1.756(5)	O(3)#4-Al(1)-O(1)	109.6(3)
Al(1)-O(5)#1	1.757(4)	O(3)#4-Al(1)-O(5)#1	107.36(19)
Al(1)-O(5)	1.757(4)	O(1)-Al(1)-O(5)#1	110.91(19)
Al(2)-O(6)	1.741(4)	O(3)#4-Al(1)-O(5)	107.36(19)
Al(2)-O(4)	1.746(4)	O(1)-Al(1)-O(5)	110.91(19)
Al(2)-O(2)	1.758(4)	O(5)#1-Al(1)-O(5)	110.6(3)
Al(2)-O(7)	1.766(4)	O(6)-Al(2)-O(4)	115.1(2)
O(4)-P(2)#3	1.517(4)	O(6)-Al(2)-O(2)	107.6(2)
O(5)-P(2)#3	1.505(4)	O(4)-Al(2)-O(2)	106.9(2)
O(6)-P(2)#2	1.513(4)	O(6)-Al(2)-O(7)	107.1(2)
O(3)-Al(1)#5	1.729(5)	O(4)-Al(2)-O(7)	112.4(2)
C(1)-C(3)	1.37(3)	O(2)-Al(2)-O(7)	107.3(2)
C(1)-N(1)	1.51(2)	P(1)-O(1)-Al(1)	151.7(4)
C(2)-C(3)	1.57(2)	P(2)-O(2)-Al(2)	142.0(3)
C(2)-C(3)#6	1.57(2)	P(2)#3-O(4)-Al(2)	148.5(3)
C(2)-C(3)#7	1.57(2)	P(2)#3-O(5)-Al(1)	145.9(3)
N(1)-C(1)#6	1.51(2)	P(2)#2-O(6)-Al(2)	149.1(3)
N(1)-C(1)#7	1.51(2)	P(1)-O(7)-Al(2)	145.6(3)
N(1)-C(4)#6	1.52(3)	P(1)-O(3)-Al(1)#5	173.1(5)
N(1)-C(4)	1.52(3)	C(3)-C(1)-N(1)	110(2)
N(1)-C(4)#7	1.52(3)	C(1)-C(3)-C(2)	113(2)
C(4)-C(5)	1.42(5)	C(1)#7-N(1)-C(4)#6	105(7)
C(5)-C(4)#1	1.42(5)	C(1)#6-N(1)-C(4)	105(7)
O(3)-P(1)-O(7)#1	108.1(2)	C(1)-N(1)-C(4)#7	105(7)
O(3)-P(1)-O(7)	108.1(2)	N(1)-C(4)-C(5)	117(5)
O(7)#1-P(1)-O(7)	110.6(3)		

Symmetry transformations used to generate equivalent atoms:

#1 x,y,-z+3/2 #2 y,-x+y,-z+1 #3 x-y,x,-z+1
 #4 -x+y+1,-x+1,z #5 -y+1,x-y,z #6 -y+1,x-y+1,z
 #7 -x+y,-x+1,z #8 -y+1,x-y+1,-z+3/2

Table 6.8 Anisotropic displacement parameters (Å) for TMAda⁺-SiCHA. The anisotropic displacement factor exponent takes the form:

$$-2\pi^2[h^2a^*{}^2U_{11}+\dots+2hka^*b^*U_{12}]$$

	U ₁₁	U ₂₂	U ₃₃	U ₂₃	U ₁₃	U ₁₂
P(1)	0.017(1)	0.024(1)	0.017(1)	0.000	0.000	0.012(1)
P(2)	0.030(1)	0.019(1)	0.023(1)	-0.002(1)	0.003(1)	0.012(1)
Al(1)	0.015(1)	0.018(1)	0.023(1)	0.000	0.000	0.006(1)
Al(2)	0.026(1)	0.021(1)	0.032(1)	-0.003(1)	-0.010(1)	0.008(1)
O(1)	0.044(3)	0.025(2)	0.048(3)	0.000	0.000	0.020(2)
O(2)	0.050(2)	0.053(3)	0.028(2)	-0.005(2)	-0.004(2)	0.027(2)
O(4)	0.056(3)	0.036(2)	0.051(3)	0.002(2)	0.002(2)	0.030(2)
O(5)	0.040(2)	0.047(2)	0.045(2)	-0.005(2)	-0.020(2)	0.015(2)
O(6)	0.027(2)	0.042(2)	0.044(2)	0.009(2)	-0.007(2)	-0.001(2)
O(7)	0.038(2)	0.048(2)	0.023(2)	-0.010(2)	-0.010(2)	0.019(2)
O(3)	0.034(3)	0.062(4)	0.044(3)	0.000	0.000	0.035(3)

The structure of MAPO-17 is described by the erionite (ERI) framework, which has been reported in space group P 6₃/mmc. The reduction in symmetry to P63/m can be explained by the incorporation of the propylene-diquinuclidium template. The MAPO-17 framework is composed of 6-rings stacked in the sequence AABAAC as shown in figure 6.6. This sequence results in the formation of erionite cages, which have six 8-ring, and five 6-ring windows. In addition this stacking results in the formation of the cancrinite cages. Six erionite cages surround one cancrinite cage. Figure 6.7 shows the template occluded within the erionite cages and the unoccupied cancrinite cage within the framework. The template exhibits a space-filling role. It can be seen that the propylene unit of the propylene-diquinuclidium template is most disordered due to its chain-like properties which is also reflected in the high thermal parameters of C4 and C5 (see table 6.6).

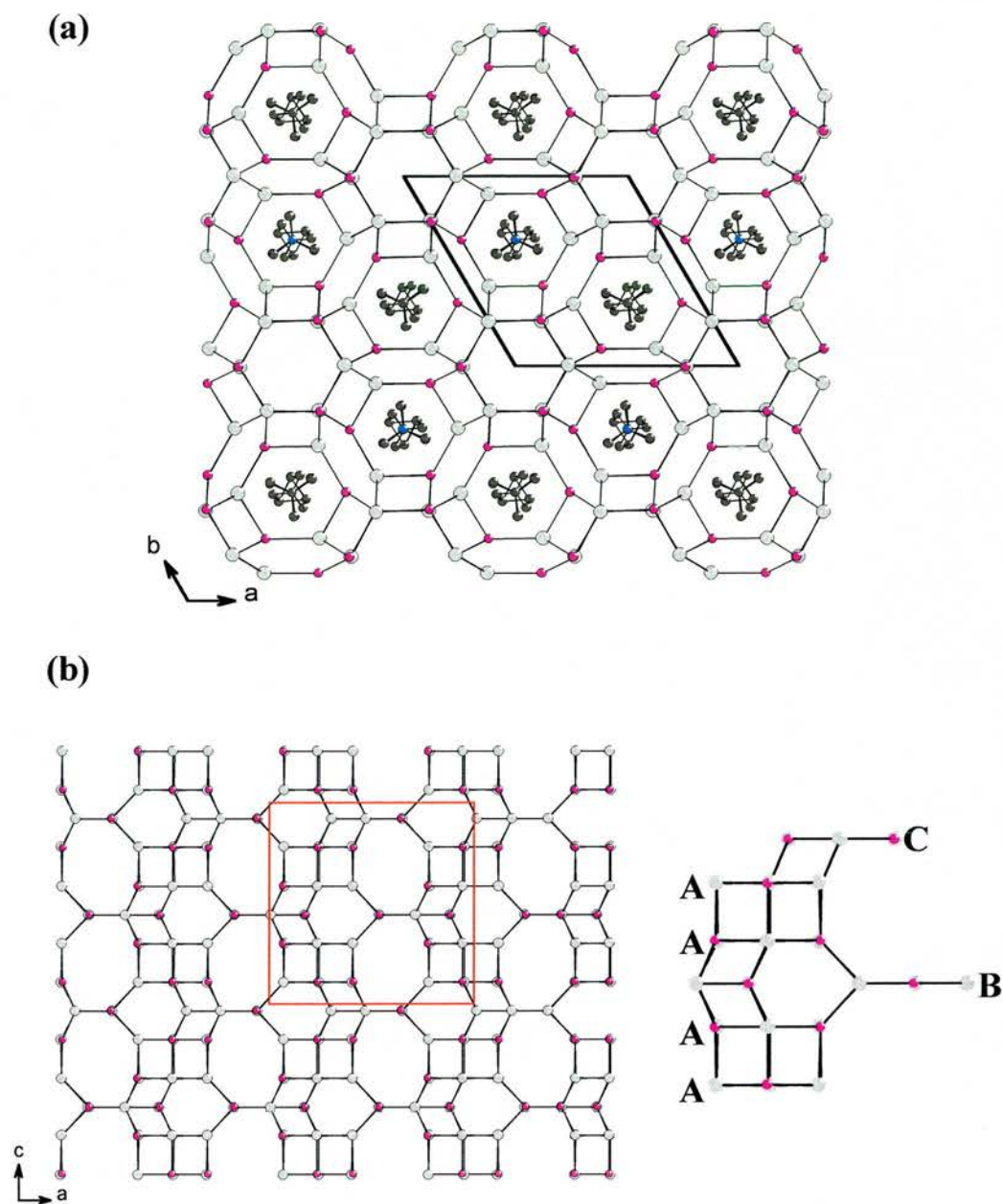


Figure 6.6 Illustrations of the ERI framework where Al is purple, P is light grey, carbon is dark grey and nitrogen is blue. (a) Shows the presence of the organic template in the ERI cages when viewed down the *c*-axis and the empty cancrinite cages. (b) Illustrates the stacking of 6-rings to form the framework. The area in the red rectangle is highlighted as the ABAAC stacking sequence shown on the left. The organic has been removed for clarity.

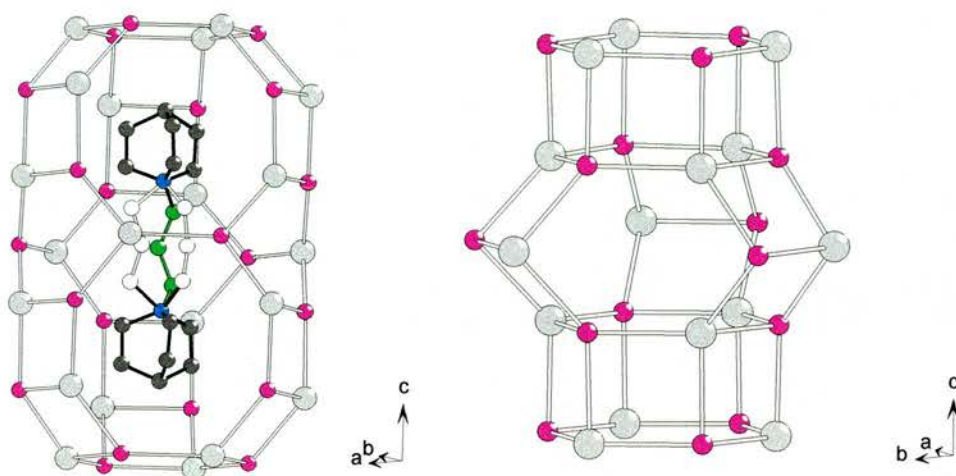


Figure 6.7 (a) An illustration of the template containing erionite cage in MAPO-17 (colour scheme is same as before). The template is disordered on a 3-fold rotation axis. This disorder can be seen in the propylene chain shown in green, red and yellow. (b) The empty cancrinite cage is composed of two D6Rs joined by three sets of two bridging D4Rs.

MAPO-17 has been crystallographically modelled as a pure AlPO-17 for simplicity with unit cell contents of $2[\text{C}_{16}\text{N}_2\text{H}_{32}^{2+}]\text{-Al}_{18}\text{P}_{18}\text{O}_{72}$. However in the MAPO-17 magnesium substitutes for aluminium in the framework. The reported composition is $2[\text{C}_{16}\text{N}_2\text{H}_{32}^{2+}]\text{-Al}_{18-x}\text{Mg}_x\text{P}_{18}\text{O}_{72}$ where $x=4$. The substitution of Mg^{2+} for Al^{3+} provides the necessary charge balancing. This is in contrast to the charge-balancing incorporation of fluoride ions into the framework as seen in the previous example of chabazite.

6.4 Conclusions

The use of low temperature single-crystal X-ray diffraction has allowed an accurate model of structures that display disorder. This has allowed the location of template molecules within as-made MAPO-17 and Si-CHA.

The crystallographic location of fluoride within the D6Rs of chabazite has furthered previous structural studies and proved previously unconfirmed elemental analysis evidence for the presence of fluoride within the CHA framework to be accurate. The location of the fluoride has also provided an understanding of the template disorder and the method of charge balancing within this structure. Although the effect of fluoride upon the template is not as great as seen in ITQ-4^{8,9}, I would suggest that this work consolidates the theory that fluoride provides a localised negative charge which is responsible for ordering the template.

The single-crystal structure of as-made MAPO-17 accurately modelled the disorder of the template within the erionite cage and illustrated its space-filling role. In addition this metalloaluminophosphate structure illustrated a contrasting method of charge balancing of a zeolite by the substitution of magnesium for aluminium in the framework. Illustrating a potential method for testing the significance of the role that fluoride has in imposing polarity on a noncentrosymmetric framework by examining an aluminosilicate ITQ-4 or similar metal substituted ITQ-4 frameworks.¹⁰

6.5 References

1. R.E. Morris and P.A. Wright, *Chem. Ind.*, 1998, 7, 256.
2. L.S. Dent and J.V. Smith, *Nature*, 1958, **181**, 1794.

3. J.J. Pluth and J.V. Smith, *J. Phys. Chem.*, 1989, **93**, 6516.
4. M.M. Harding and B.M. Kariuki, *Acta Crystallogr.*, 1994, **C50**, 852.
5. M.-J. Diaz-Cabanas, P.A. Barrett and M.A. Camblor, *Chem. Commun.*, 1998, **17**, 1881.
6. J.J. Pluth, J.V. Smith and J.M. Bennett, *Acta Crystallogr.*, 1986, **C42**, 283.
7. L. Delmotte, M. Souillard, F. Guth, A. Seive, A. Lopez and J.-L. Guth, *Zeolites*, 1990, **10**, 778.
8. I. Bull, L.A. Villaescusa, S.J. Teat, M.A. Camblor, P.A. Wright, P. Lightfoot and R.E. Morris, *J. Am. Chem. Soc.*, 2000, **122**, 7128.
9. L.A. Villaescusa, P.S. Wheatley, I. Bull, P. Lightfoot and R.E. Morris, *J. Am. Chem. Soc.*, 2001, **123**, 8797.
10. L.A. Villaescusa, P.A. Barrett, M. Kalwei, H. Koller and M.A. Camblor, *Chem. Mater.*, 2001, **13**, 2332.

Chapter 7 – Novel Materials

7.1 Introduction

The rational design of new materials is an important goal for zeolite chemists in order to provide varied structures for new technologies. For instance, the design of zeolites containing larger sizes of pores would potentially open up other applications for these materials such as different catalytic reactions. In fact despite being well known already in catalysis, ion exchange and adsorption applications (see chapter 1.2), microporous materials are an example where designer synthesis will certainly have an impact on future technologies. Recently, the US Department of Energy identified the preparation of tailored porous solids as a major challenge and stated potential applications in areas such as shape selective gas or liquid permselective membranes, catalytic membrane reactors, energy storage systems, molecular electronic and optoelectronic devices, as well as biomolecule separation, isolation and delivery.¹

The study of structurally diverse framework solids is flourishing. The realisation that most of the elements in the Periodic Table can be incorporated has stimulated the preparation of very many new structures of this type. A key area for the discovery of structures with novel properties is that of frameworks containing both tetrahedrally- and octahedrally-coordinated cations.² Examples include titanium, yttrium and rare-earth silicates, and a wide variety of phosphates of metals such as gallium, indium, nickel and vanadium.³⁻⁸ Fewer sulphate frameworks have been reported⁹⁻¹¹, although the framework of langbeinite ($K_2Mg_2(SO_4)_3$) displays full corner-sharing between MgO_6 octahedra and SO_4 tetrahedra and open framework cadmium sulphates have been prepared recently using the 'amine sulphate' route.

A very wide range of metal cations have been used in the hydrothermal synthesis of this kind, but to our knowledge no studies exist on the incorporation of scandium. This is a little surprising given that it possesses suitable ionic size, ionicity and solubility. This is presumably a result of its expense from typical commercial supplies. In addition there is the mineral kolbeckite, $\text{ScPO}_4 \cdot 2\text{H}_2\text{O}$, which is isostructural with phosphosiderite, a dense framework in which octahedral-coordinated scandium shares corners with four phosphate tetrahedra and is additionally coordinated to two water molecules.¹²

Macrocycles have recently been utilised as templating agents in zeolite syntheses. The cyclic nature of these contrasts to the normal linear amines generally used as structure directing agents.¹³ The charge density is also higher as there is higher nitrogen to carbon ratio than on the linear amines. These differences should also promote the synthesis of new frameworks. Wright and co-workers have prepared two novel zeolite structures (STA-6 and STA-7) using macrocycles as SDAs.^{14,15} A different structure interaction involves a direct binding of the macrocycle to the framework as seen by Wragg et al. in a gallium phosphate.¹⁶ The cyclam macrocycle forms a gallium-cyclam complex which links the double four rings to produce a zeolite framework. Macrocycles can also display strong H-bonding interactions with oxyanions, so they are the logical choice for novel syntheses of this kind. In addition functional metals could be substituted into the macrocycle which could lead to multifunctional materials.

By applying both these innovative synthetic ideas (octahedral-tetrahedral frameworks and macrocycle templates) to scandium and sulphates we set out to prepare a new microporous structure. Here I report the hydrothermal synthesis, structure solution of a novel of a scandium sulphate/phosphate and a scandium

sulphate templated by cyclen. Powder X-ray diffraction patterns indicates that the sulphate-only version of this compound can be prepared, but the scandium sulphate- and phosphate-containing preparation gave a monophasic product of small cubic crystals suitable for laboratory-based single crystal diffraction and so we report here the characterisation of the mixed anion compound. The powder diffraction pattern can be fitted accurately by the crystallographic data from the single-crystal experiment, indicating the bulk material is phase pure.

7.2 Experimental

7.2.1 Synthesis of scandium sulphate/phosphate and scandium sulphate templated by cyclen

A homogeneous gel of composition $0.5 \text{ Sc}_2\text{O}_3 : 2.3 \text{ H}_2\text{SO}_4 : 1 \text{ H}_3\text{PO}_4 : 0.4 \text{ Cyclen} : 4 \text{ H}_2\text{O} : \text{HF}$, which was prepared by adding 0.39 g of scandium sulphate pentahydrate (Aldrich), 0.19 g phosphoric acid (80 wt%, Aldrich), 0.24 g cyclen sulphate (Aldrich), 0.045 g distilled water and 0.03 g HF. After ageing for one hour the resultant paste was transferred to a PTFE-lined acid digestion bomb (23ml, Parr). This reaction was carried out under static conditions at 463 K for 4 days. It was then removed from the furnace and quenched. The product was washed with deionised water and dried at 353 K. The product contained small cubic crystals (approximately $50\mu\text{m} \times 50\mu\text{m} \times 50\mu\text{m}$) that were suitable for in-house X-ray diffraction studies.

A homogeneous gel of composition $0.5 \text{ Sc}_2\text{O}_3 : 2.3 \text{ H}_2\text{SO}_4 : 1 \text{ H}_3\text{PO}_4 : 0.4 \text{ cyclen} : 4 \text{ H}_2\text{O} : \text{HF}$, which was prepared by adding 0.39 g of scandium sulphate pentahydrate (Aldrich), 0.162 g sulphuric acid (99%, Aldrich), 0.24 g cyclen sulphate (Aldrich), 0.045 g distilled water and 0.03 g HF. After ageing for one hour the resultant paste was transferred to a polytetrafluoroethylene lined acid digestion bomb (23ml, Parr).

This reaction was carried out under static conditions at 463 K for 4 days. It was then removed from the furnace and quenched. The product was then washed with deionised water and dried at 353 K.

7.2.2 X-ray Diffraction

Single crystal X-ray diffraction data was collected in St Andrews on the Bruker AXS SMART CCD area detector diffractometer at room temperature using molybdenum K_{α} X-rays from sealed tube sources. A single-crystal structure solved, see figure 7.1, and gave an R-factor of 12.25 %.

The scandium sulphate product was a crystalline powder so a powder diffraction pattern was collected on the STOE stadip diffractometer (using primary monochromated $Cu-K_{\alpha 1}$ radiation) over the 2θ range of 3 to 80° . X-ray fluorescence from the $Cu-K_{\alpha}$ resulted in a high background signal.

7.2.3 Energy dispersive X-ray analysis and elemental analysis

To confirm the presence and ratios of metal cations within the framework, single crystals were studied by energy dispersive X-ray analysis. This was carried out on a Joel JEM-2010 electron microscope using an Oxford Instruments EDX attachment.

A phase pure sample of the mixed anion compound was examined by CHN and the organic content was measured by a Carlo Erba CHN elemental analyser.

7.2.4 NMR

MAS NMR experiments were carried out on the cyclen-scandium sulphate/phosphate (cyclen-ScSPO) using the EPSRC Solid-State NMR Service (Durham) on a Varian Unityplus 200 MHz spectrometer. Chemical shifts were reported with respect to TMS and 85 % H_3PO_4 for ^{13}C and ^{31}P respectively. ^{13}C CP MAS NMR spectra were obtained using a spinning rate of 4 kHz, acquisition time of

30 ms, relaxation delay of 2 s and a contact time of 1 ms. ^{31}P DP MAS NMR spectra were obtained using a spinning rate of 7.5 kHz, acquisition time of 20.2 ms, relaxation delay of 120 s.

MAS NMR experiments were carried out on the cyclen-scandium sulphate (cyclen-ScSO) using the EPSRC Solid-State NMR Service (Durham) on a Varian Unityplus 200 MHz spectrometer. Chemical shifts were reported with respect to TMS and 85 % H_3PO_4 for ^{13}C and ^{15}N respectively. ^{13}C CP MAS NMR spectra were obtained using a spinning rate of 4.65 kHz, acquisition time of 15 ms, relaxation delay of 1 s and a contact time of 1 ms. ^{15}N CP MAS NMR spectra were obtained using the same conditions.

7.3 Results and discussion

7.3.1 Structural characterisation of cyclen-scandium sulphate/phosphate

The structure of this material was determined from laboratory single-crystal XRD data. Full details of the data collection and structure solution are given in table 7.1.

Table 7.1 Crystal data and structure refinement for cyclen-ScS/PO

Identification code	cyclen-ScS/PO	
Empirical formula	$\text{Sc}_{56}(\text{SO}_4)_{98}(\text{PO}_4)_{22} \cdot [\text{C}_8\text{N}_4\text{H}_{24}]_{15} \cdot 34[\text{H}_3\text{O}^+] \cdot 23\text{H}_2\text{O}$	
Formula weight	17721 g	
Temperature	293(2) K	
Wavelength	0.71073 Å	
Crystal system, space group	Cubic, Pn-3n	
Unit cell dimensions	$a = 25.2469(3)$ Å	$\alpha = 90^\circ$.
	$b = 25.2469(3)$ Å	$\beta = 90^\circ$.
	$c = 25.2469(3)$ Å	$\gamma = 90^\circ$.
Volume	$16092.5(3)$ Å ³	
Z, Density (calculated)	60, 1.732 Mg/m ³	

Absorption coefficient	1.093 mm ⁻¹
F(000)	8424
Crystal size	0.5 x 0.5 x 0.5 mm ³
Theta range for data collection	1.61 to 23.26°.
Index ranges	-28<=h<=27, -26<=k<=28, -28<=l<=26
Reflections collected	74745
Independent reflections	1945 [R(int) = 0.3526]
Completeness to theta = 23.26°	99.9 %
Refinement method	Full-matrix least-squares on F ²
Data / restraints / parameters	1945 / 0 / 155
Goodness-of-fit on F ²	1.364
Final R indices [I>2sigma(I)]	R1 = 0.1225, wR2 = 0.3397
R indices (all data)	R1 = 0.1816, wR2 = 0.3897
Largest diff. peak and hole	7.498 and -0.887 e.Å ⁻³

This structure is complicated as it contains both phosphorus and sulphur as T atoms. EDX showed the ratio to be 1 S : 0.3 P and that they are evenly distributed throughout the structure. The model was refined as a pure sulphate since XRD only shows the average structure. This is reflected in both the isotropic and anisotropic displacement parameters (see table 7.3 and 7.4) and the bond lengths (see table 7.4). The average calculated bond length for a S-O bond in this refinement is 1.45 Å compared to the expected 1.39 Å. This is the average of the P-O distance (1.54) and the S-O distance. However the model refines well to an R factor of 12.25 %.

Table 7.2 Atomic coordinates and equivalent isotropic displacement parameters (\AA^2) for cyclen-ScS/PO. $U(\text{eq})$ is defined as one third the orthogonalised U_{ij} tensor

	x	y	z	$U(\text{eq})$
Sc(1)	0.0000	0.5000	0.0000	0.013(2)
Sc(2)	0.1025(1)	0.6683(1)	0.0423(1)	0.015(1)
S(1)	0.0685(2)	0.5531(2)	0.1024(2)	0.017(1)
S(2)	0.0956(2)	0.7884(2)	-0.0163(2)	0.017(1)
S(3)	0.1425(2)	0.7500	0.1425(2)	0.065(3)
O(1)	0.0974(5)	0.6031(4)	0.0913(5)	0.025(3)
O(2)	0.0585(4)	0.5254(4)	0.0528(5)	0.025(3)
O(3)	0.1152(5)	0.7338(4)	-0.0053(5)	0.032(3)
O(4)	0.1776(5)	0.6423(5)	0.0208(6)	0.038(3)
O(5)	0.0654(6)	0.7897(5)	-0.0655(5)	0.042(4)
O(6)	0.0283(4)	0.6940(5)	0.0629(5)	0.030(3)
O(7)	0.1010(5)	0.5205(5)	0.1362(5)	0.042(4)
O(8)	0.0185(5)	0.5659(5)	0.1283(5)	0.034(3)
O(9)	0.1410(20)	0.1957(11)	0.7681(9)	0.360(40)
O(10)	0.1363(5)	0.7061(5)	0.1059(5)	0.042(4)
C(1)	0.1291(8)	0.7649(6)	0.8361(7)	0.028(4)
C(2)	0.1074(8)	0.7094(6)	0.8497(7)	0.029(5)
N(1)	0.0880(6)	0.8037(5)	0.8224(5)	0.024(3)

Table 7.3 Anisotropic displacement parameters for cyclen-ScS/PO. The anisotropic displacement factor takes the form :

$$-2\pi^2[h^2a^{*2}U_{11}+\dots+2hka^*b^*U_{12}]$$

	U_{11}	U_{22}	U_{33}	U_{23}	U_{13}	U_{12}
Sc(1)	0.013(2)	0.013(2)	0.013(2)	-0.002(2)	0.002(2)	-0.002(2)
Sc(2)	0.014(2)	0.010(2)	0.022(2)	-0.004(1)	0.006(1)	-0.001(1)
S(1)	0.018(2)	0.015(2)	0.017(2)	-0.001(2)	-0.002(2)	-0.003(2)
S(2)	0.022(2)	0.013(2)	0.017(2)	-0.001(2)	0.006(2)	-0.002(2)
S(3)	0.079(5)	0.035(4)	0.079(5)	-0.036(4)	-0.060(5)	0.036(4)
O(1)	0.029(7)	0.017(6)	0.028(7)	0.006(5)	-0.004(5)	-0.008(5)
O(2)	0.023(7)	0.020(6)	0.031(7)	-0.005(5)	-0.001(5)	-0.007(5)
O(3)	0.028(7)	0.012(6)	0.057(9)	0.004(6)	0.017(6)	0.002(5)

O(4)	0.026(7)	0.021(7)	0.066(10)	-0.004(6)	0.022(7)	0.011(5)
O(5)	0.056(9)	0.046(9)	0.025(7)	-0.001(6)	-0.003(6)	-0.021(7)
O(6)	0.019(7)	0.024(7)	0.045(8)	-0.003(6)	0.010(6)	0.009(5)
O(7)	0.054(9)	0.024(7)	0.047(9)	0.001(6)	-0.020(7)	0.005(6)
O(8)	0.030(7)	0.041(8)	0.031(7)	-0.006(6)	0.011(6)	-0.005(6)
O(9)	0.840(110)	0.0150(30)	0.080(20)	0.074(19)	-0.200(40)	-0.330(50)
O(10)	0.056(9)	0.032(8)	0.039(8)	-0.025(6)	-0.007(7)	-0.003(7)
C(1)	0.047(12)	0.017(10)	0.021(10)	0.000(7)	0.008(8)	-0.007(8)
C(2)	0.052(13)	0.015(9)	0.020(10)	-0.001(7)	0.002(8)	-0.011(8)
N(1)	0.031(9)	0.023(8)	0.020(8)	0.005(6)	0.016(7)	0.005(6)

Table 7.4 Bond lengths (Å) and angles (°) for cyclen-ScS/PO

Sc(1)-O(2)#1	2.089(11)	O(2)#3-Sc(1)-O(2)#5	92.2(4)
Sc(1)-O(2)	2.089(11)	O(2)#4-Sc(1)-O(2)#5	87.8(4)
Sc(1)-O(2)#2	2.089(11)	O(8)#2-Sc(2)-O(1)	91.6(5)
Sc(1)-O(2)#3	2.089(11)	O(8)#2-Sc(2)-O(10)	176.7(5)
Sc(1)-O(2)#4	2.089(11)	O(1)-Sc(2)-O(10)	85.7(5)
Sc(1)-O(2)#5	2.089(11)	O(8)#2-Sc(2)-O(6)	86.3(5)
Sc(2)-O(8)#2	2.055(12)	O(1)-Sc(2)-O(6)	92.4(5)
Sc(2)-O(1)	2.064(11)	O(10)-Sc(2)-O(6)	91.9(5)
Sc(2)-O(10)	2.054(12)	O(8)#2-Sc(2)-O(3)	91.7(5)
Sc(2)-O(6)	2.049(11)	O(1)-Sc(2)-O(3)	174.5(5)
Sc(2)-O(3)	2.067(12)	O(10)-Sc(2)-O(3)	91.1(5)
Sc(2)-O(4)	2.078(11)	O(6)-Sc(2)-O(3)	92.1(5)
S(1)-O(7)	1.442(13)	O(8)#2-Sc(2)-O(4)	93.4(5)
S(1)-O(2)	1.456(12)	O(1)-Sc(2)-O(4)	87.8(5)
S(1)-O(8)	1.458(12)	O(10)-Sc(2)-O(4)	88.4(5)
S(1)-O(1)	1.487(11)	O(6)-Sc(2)-O(4)	179.6(6)
S(2)-O(5)	1.458(13)	O(3)-Sc(2)-O(4)	87.7(5)
S(2)-O(6)#6	1.464(12)	O(7)-S(1)-O(2)	109.6(7)
S(2)-O(4)#7	1.466(12)	O(7)-S(1)-O(8)	110.7(8)
S(2)-O(3)	1.492(12)	O(2)-S(1)-O(8)	110.1(7)
S(3)-O(9)#8	1.42(3)	O(7)-S(1)-O(1)	108.5(7)
S(3)-O(9)#9	1.42(3)	O(2)-S(1)-O(1)	109.4(7)
S(3)-O(10)	1.452(12)	O(8)-S(1)-O(1)	108.7(7)
S(3)-O(10)#6	1.452(12)	O(5)-S(2)-O(6)#6	110.7(8)
O(4)-S(2)#10	1.466(12)	O(5)-S(2)-O(4)#7	110.0(8)
O(6)-S(2)#6	1.464(12)	O(6)#6-S(2)-O(4)#7	109.6(8)

O(8)-Sc(2)#3	2.055(12)	O(5)-S(2)-O(3)	110.6(8)
O(9)-S(3)#11	1.42(3)	O(6)#6-S(2)-O(3)	109.0(7)
C(1)-N(1)	1.47(2)	O(4)#7-S(2)-O(3)	106.8(7)
C(1)-C(2)	1.54(2)	O(9)#8-S(3)-O(9)#9	99(4)
C(2)-N(1)#9	1.49(2)	O(9)#8-S(3)-O(10)	109.2(17)
N(1)-C(2)#12	1.49(2)	O(9)#9-S(3)-O(10)	110.6(11)
O(2)#1-Sc(1)-O(2)	180.0(7)	O(9)#8-S(3)-O(10)#6	110.6(11)
O(2)#1-Sc(1)-O(2)#2	87.8(4)	O(9)#9-S(3)-O(10)#6	109.2(17)
O(2)-Sc(1)-O(2)#2	92.2(4)	O(10)-S(3)-O(10)#6	116.5(12)
O(2)#1-Sc(1)-O(2)#3	87.8(4)	S(1)-O(1)-Sc(2)	145.2(7)
O(2)-Sc(1)-O(2)#3	92.2(4)	S(1)-O(2)-Sc(1)	144.9(8)
O(2)#2-Sc(1)-O(2)#3	87.8(4)	S(2)-O(3)-Sc(2)	142.6(7)
O(2)#1-Sc(1)-O(2)#4	92.2(4)	S(2)#10-O(4)-Sc(2)	144.1(8)
O(2)-Sc(1)-O(2)#4	87.8(4)	S(2)#6-O(6)-Sc(2)	160.3(9)
O(2)#2-Sc(1)-O(2)#4	92.2(4)	S(1)-O(8)-Sc(2)#3	165.1(8)
O(2)#3-Sc(1)-O(2)#4	180.000(1)	S(3)-O(10)-Sc(2)	153.8(9)
O(2)#1-Sc(1)-O(2)#5	92.2(4)	N(1)-C(1)-C(2)	114.1(15)
O(2)-Sc(1)-O(2)#5	87.8(4)	C(1)-C(2)-N(1)#9	115.6(14)
O(2)#2-Sc(1)-O(2)#5	180.0(6)	C(1)-N(1)-C(2)#12	114.4(14)

Symmetry transformations used to generate equivalent atoms:

#1 -x,-y+1,-z #2 y-1/2,z+1/2,-x #3 -z,x+1/2,y-1/2
 #4 z,-x+1/2,-y+1/2 #5 -y+1/2,-z+1/2,x
 #6 z,-y+3/2,x #7 y-1/2,-x+1,-z #8 y,z,x
 #9 x,-z+3/2,y #10 -y+1,x+1/2,-z #11 z,x,y
 #12 x,z,-y+3/2

The sulphate/phosphate problem is quite clearly seen in the thermal parameters of S3 and its dangling oxygen O9. The large displacement parameters can be explained by figure 7.1.

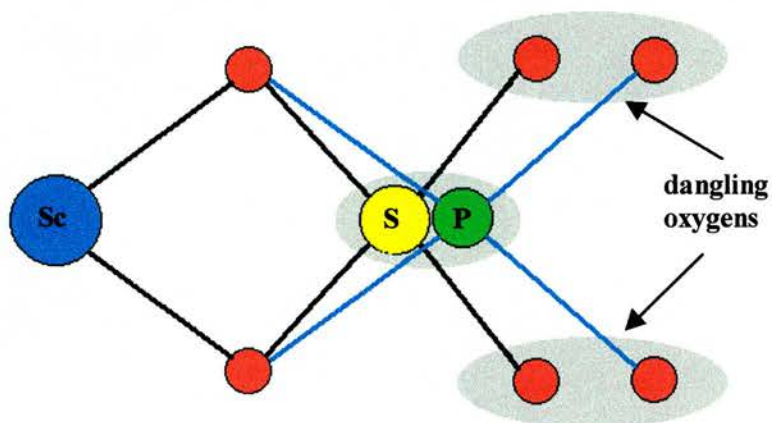


Figure 7.1 An illustration explaining the large thermal parameters exhibited by S3 and its dangling oxygen O9. XRD will show the average position of possible S (yellow) and P (green) positions and the motion of these atoms are shown in grey. The displacement parameter for the dangling oxygen is considerably larger as this disorder increases as we move away from the ordered framework.

To confirm the bulk sample was phase pure, powder X-ray diffraction was performed from 3 to 80 °2θ on a STOE stadip diffractometer using Cu K_{α1} radiation. Le Bail fitting of the pattern in cubic P n-3n was able to account for almost all the reflections (R=6 %). Rietveld refinement gave a reasonable fit (Rwp=6.88%), bearing in mind that water molecules and possibly cyclen and sulphate species included disordered in the pores were not included in the model, and confirmed that the bulk sample of the sulphate-phosphate is close to phase pure.

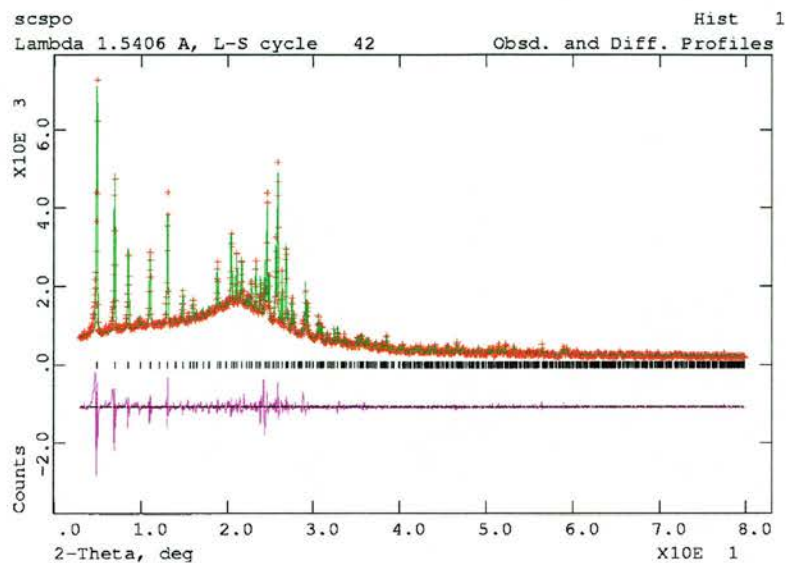


Figure 7. 2 Observed (red) and calculated (green) X-ray diffraction pattern for cyclen-ScSPO following Le Bail refinement. Vertical ticks indicate positions of allowed reflections in space group Pn-3n. The lower purple trace is the difference plot.

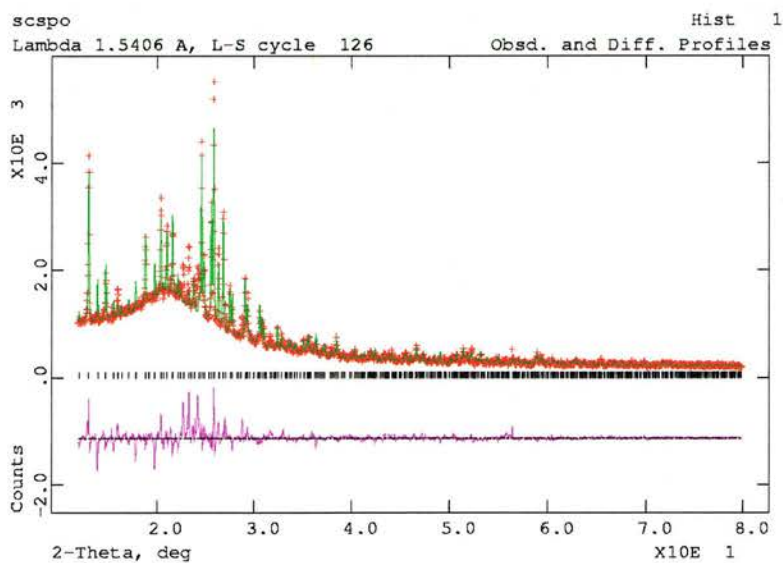


Figure 7. 3 Observed (red) and calculated (green) X-ray diffraction pattern for cyclen-ScSPO following Le Bail refinement. Vertical ticks indicate positions of allowed reflections in space group Pn-3n. The lower purple trace is the difference plot.

7.3.2.1 Structure of cyclen-ScSPO

The structure is novel (see figure 7.4), and the closest related material is a sulphate mineral called voltaite which is cubic (space group $Fd-3c$) with a unit cell dimension of 27.254 Å and is made up of a three-dimensionally connected framework of MO_6 octahedra ($M=Fe(II)$, $Fe(III)$ and Al) and sulphate tetrahedra.¹¹ The novel structure possesses parallel series of alternating rows of large and small channels along the diagonal of each crystallographic axis. The 16 MR and 8 MR channels can be seen more clearly in figure 7.4b where the template has been removed for clarity.

The structural building unit of this structure (formula $Sc_7S_{23}O_x$) is shown in figures 7.5a and b. All scandium ions are octahedrally coordinated by oxygen and all sulphate groups are tetrahedral. Each building unit consists of one central scandium, which is connected to six external scandiums via sulphate groups. Each external scandium is connected to three scandium of the same building unit via two sulphates within the unit - one of which is not in either building unit, but possesses two (rather than one, which is the case with all the other sulphate units) dangling oxygens. In this way, each Sc_7S_{12} building unit is connected to six others, with the only other polyhedra unaccounted for being the SO_4 tetrahedra with two dangling bonds that link between building units. The manner in which two building units are connected is illustrated in figure 7.5b. The building units arrange to give a framework that contains two types of cage; a small cage occupied by two cyclen templates, and a larger cage which has a free diameter of around 13 Å and possess six windows blocked by cyclen molecules. The large cages are filled with physically absorbed water.

These structural building units join to form a three-dimensional network. Another

way of usefully visualising the network is by considering it as being made up from the secondary building units in the following way. Firstly, the building units are linked into corrugated layers, each SBU being attached to four others in the sheet (see figure 7.6b) Then these corrugated layers are connected above and below to adjacent layers as shown in figure 7.6c. This results in large and small channels.

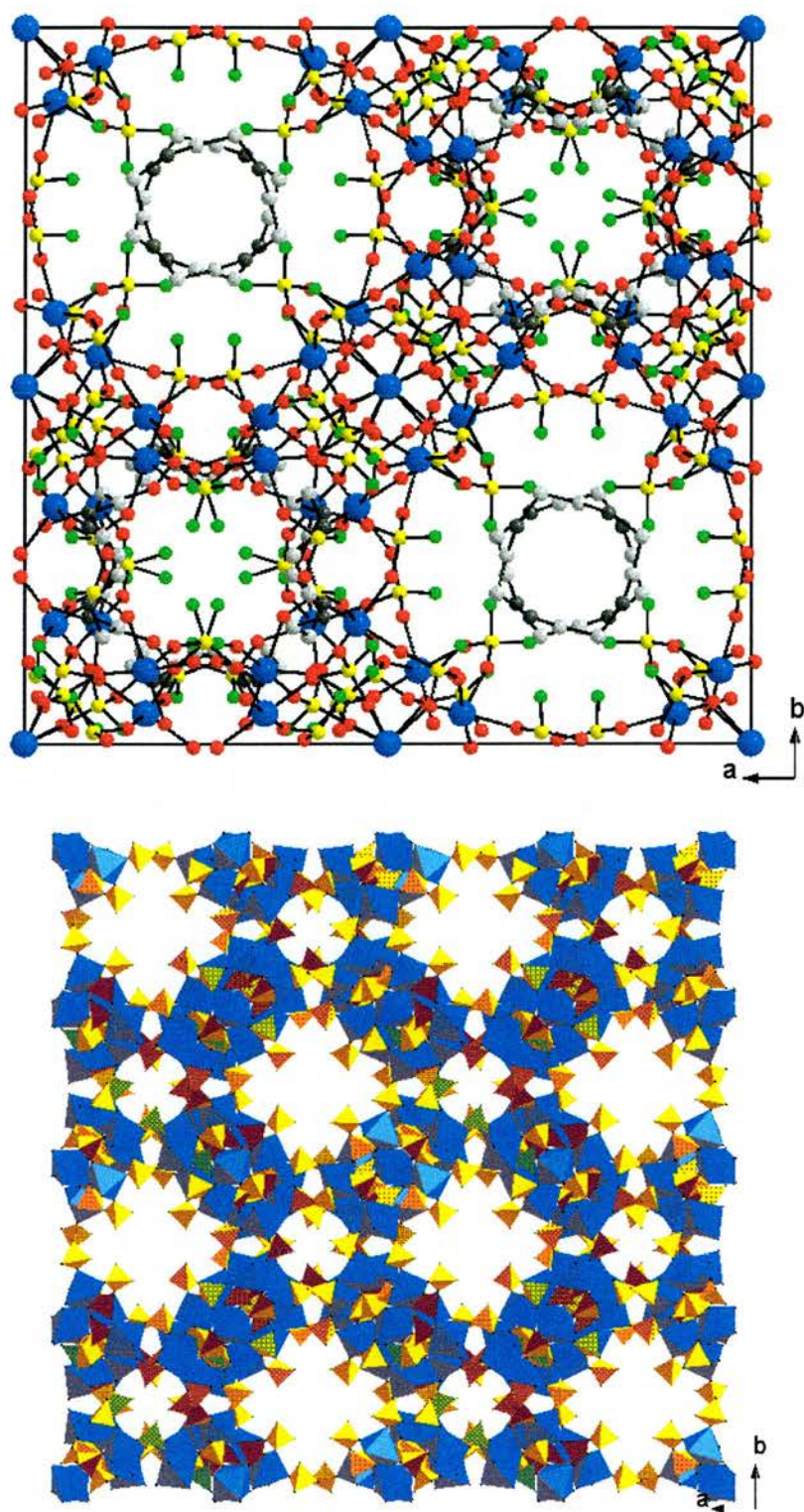


Figure 7.4 Representations of the structure of cyclen-ScS/PO. (a) A projection down the a-axis (unit cell outlined) showing the cyclen contained in the windows of the channels. Sc is blue, S is yellow, framework O is red, dangling O is green, C is grey and N is dark grey. (b) An extended projection with the cyclen removed to enable the view of the channel system more clearly. Sc octahedra are blue and S tetrahedra are yellow. It can be described as a series of parallel rows of 16 MR channels running diagonal to each crystallographic axis.

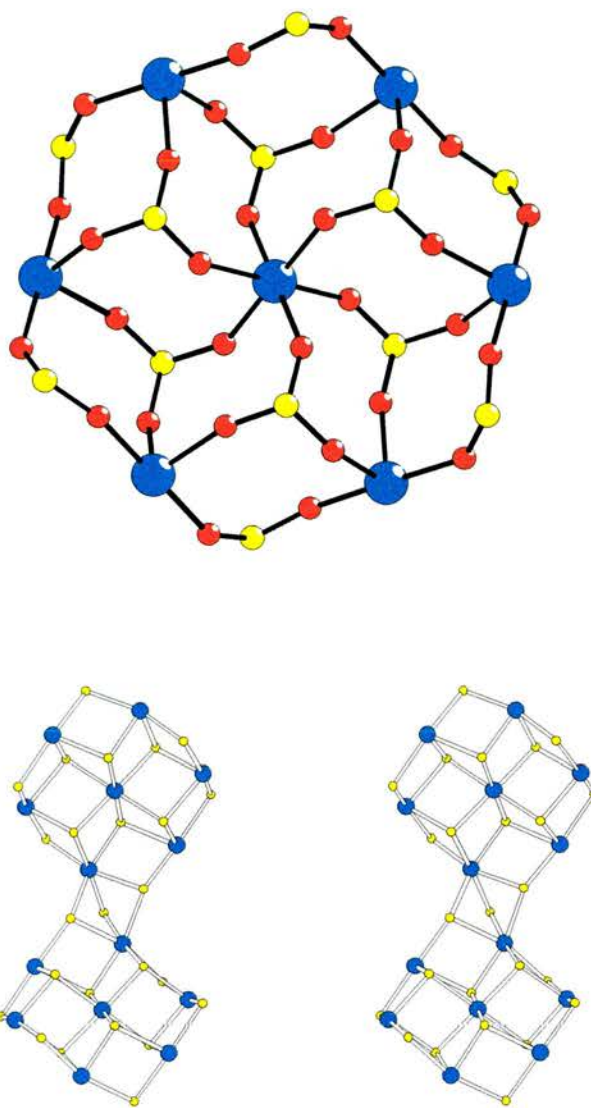
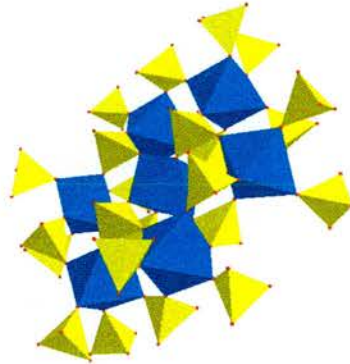
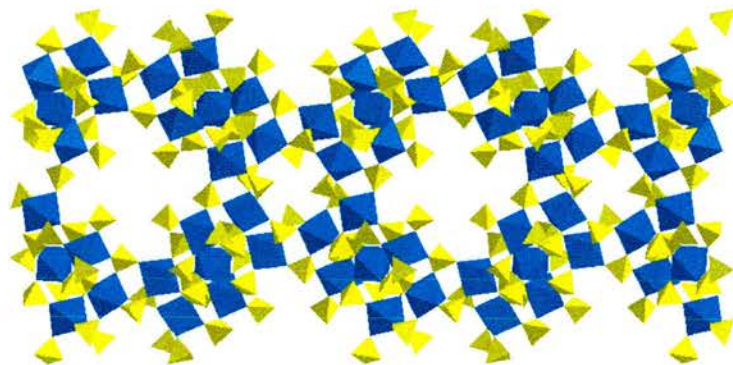


Figure 7.5 (a) Illustration of the structural building unit with scandium as blue, sulphur as yellow and oxygen as red. (b) A stereoview showing the linking of these SBUs via three bridging sulphate groups. Oxygen has been removed for clarity.

(a)



(b)



(c)

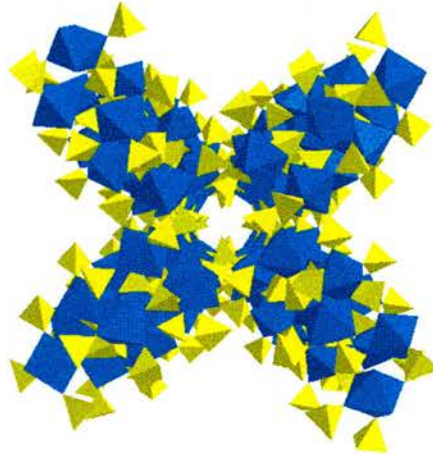


Figure 7.6 Illustrations of the structural building unit and its ordering in the structure where the SO_4 tetrahedra are yellow and the ScO_6 octahedra are blue. (a) Depicts the SBU with all the polyhedra present to allow easy identification of the SBU within the network. (b) Shows the linking of these SBUs to form a 2-dimensional sheet of layers. (c) Illustrates of two of these 2-dimensional sheets joining towards the 3-dimensional network.

All the sulphate groups possess dangling oxygens- two of the sulphurs have one dangling oxygen and the other is attached to two. These oxygens project into the channels and strongly interact with the cyclen through hydrogen bonding and/or electronically (this will be discussed later in the consideration of charge balancing and the oxygen species present).

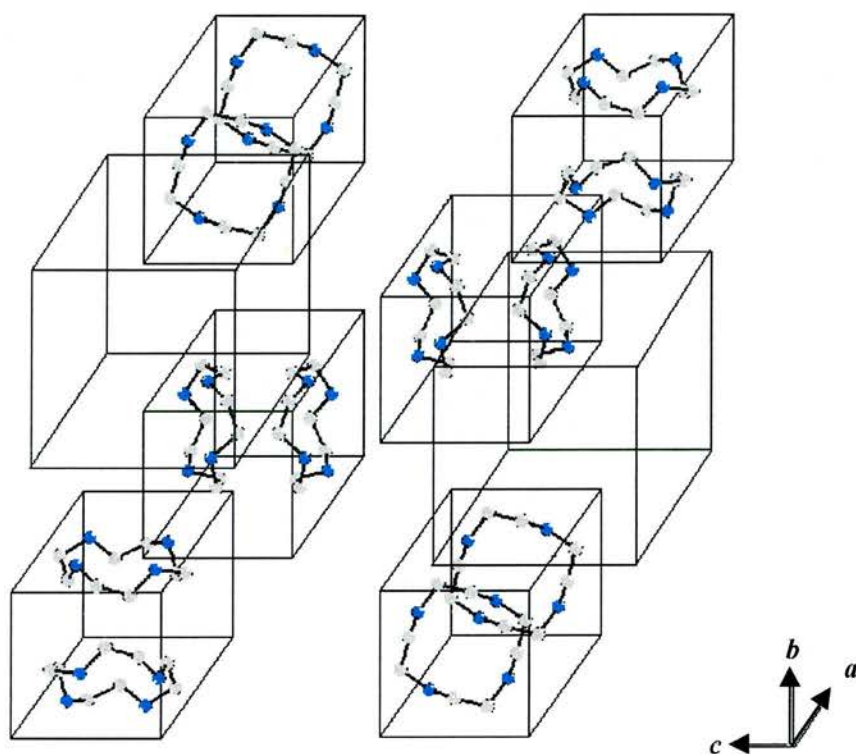
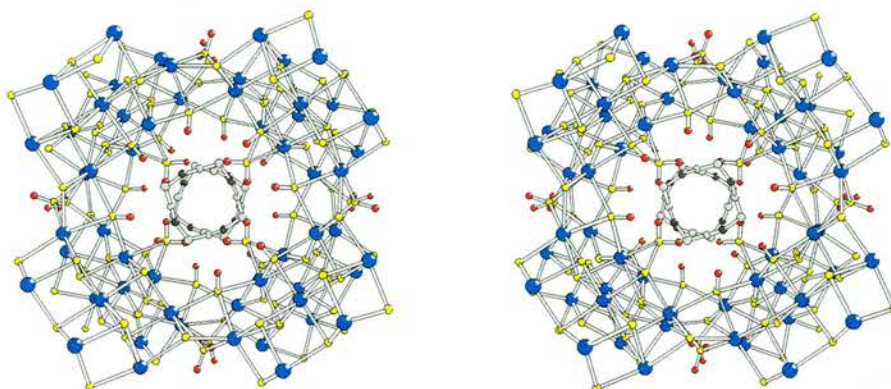


Figure 7.7 An illustration of the positions of the 12 cyclen in the unit cell. The unit cell can be separated into its 8 component cages and be thought of as 8 cubes. These can be divided into 2 groups - the cyclen occupied cage and the unoccupied cage. C is light grey and N is blue.

It is very difficult to picture the cages and the cyclen positions within the cubic structure due to the high degree of symmetry. Figure 7.7 illustrates the cyclen positions within the unit cell schematically for clarity. In a unit cell there are six smaller cages and 2 larger cages. The cyclen template occupies the six smaller cages, leaving the two supercages unoccupied. Figure 7.8a shows the positions of the cyclen

within this smaller cage, it shows the high degree of interaction with the projected oxygens. Twenty four projected oxygens are close to each cyclen (distances are given in table 7.5). Most templates are space filling in nature and tend to occupy the cages, whereas this cyclen is located in the window into the cage. The positioning of the template in the window of a zeolite pore is rare, a known example of this is the occupancy of the window of Zeolite Y by sodium. The high degree of interactions with the dangling oxygens may justify this positioning. Each cyclen cage contains two template molecules that occupy the large windows of the cage, thus accounting for two of the possible six windows. The remaining four windows are smaller 8 MR windows as shown in figure 7.8b.

(a)



(b)

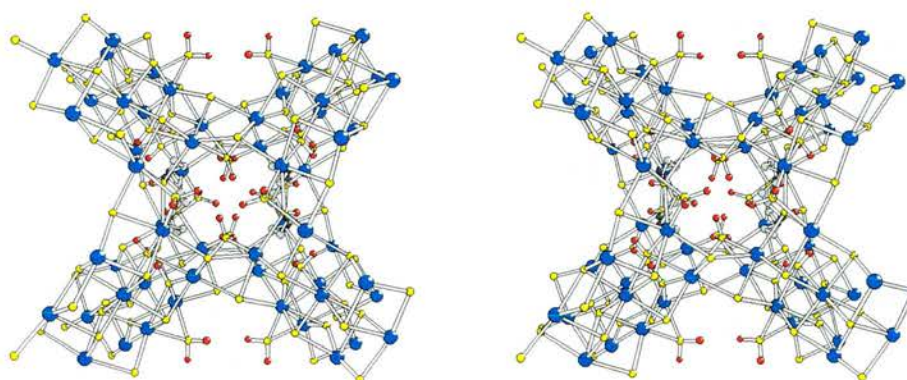


Figure 7.8 Stereoviews of the cyclen occupied cage. **(a)** Shows the cyclen lying perpendicular to the direction of the 16 MR channels in this case down the *a*-axis. **(b)** Shows the cyclen cage in the direction of the 8 MR channel, in this case is present in both the *b* and *c* directions. Both of these projections can be seen in all crystallographic directions, with the large channel direction always perpendicular to the cyclen and the small channels in both the remaining crystallographic axes. Sc is blue, S is yellow, and dangling O is red. All other framework oxygen is removed for clarity.

Table 7.5 Distances (Å) between dangling oxygens and cyclen.

	N1	C1	C2
O5	3.13	4.508	3.131
O7	2.908	3.03	3.121
O9_S1	3.923	3.184	3.186
O9_S2	4.597	3.672	4.526

The unoccupied cage can be seen in figure 7.9a. It has 16MR channels running in the direction of each of the crystallographic axes. Crystallographically there does not

seem to be anything occupying this vast cage. However, TGMS suggests that 5 wt% of this structure is water and this could well contain much of this water. Another way of thinking of this large unoccupied cage is to consider that cyclen is occupying eight positions on the outside this cage which are parallel to the 16MR windows as seen in figure 7.9b, leaving the inside of this cage devoid of organic content. This directs the size and shape of the 16 MR window.

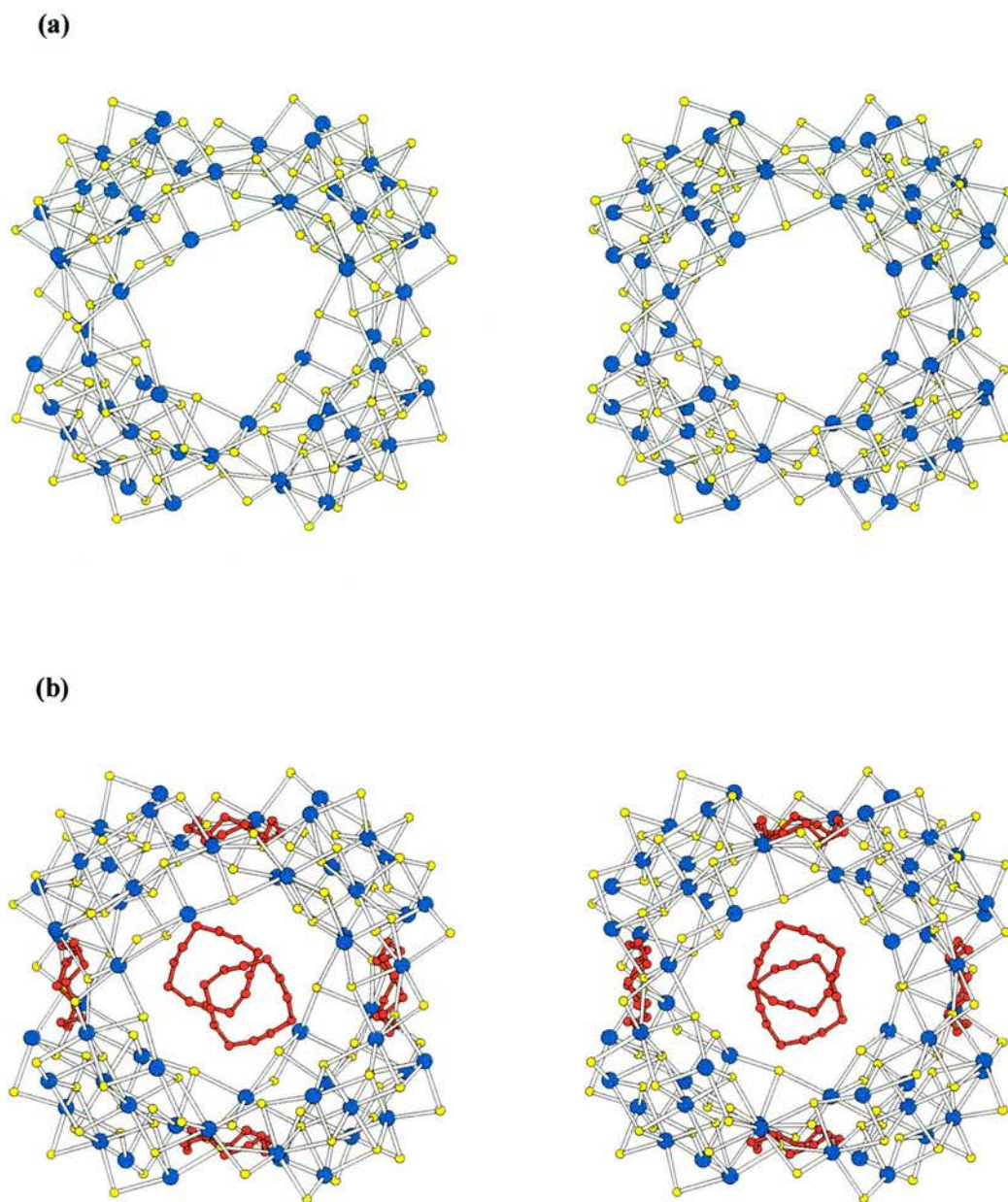


Figure 7.9 Stereoviews of the large unoccupied cage **(a)** A projection down the a -axis showing the 16 MR channels running along each of the crystallographic axes. **(b)** This shows the cyclen occupying each of the six windows into the large unoccupied cage. It can be described as sitting in a crater of the cage. Sc is blue, S is yellow and cyclen is red. All oxygen has been removed for clarity.

Figure 7.10 depicts the formation of the large channels by considering the environment of the large unoccupied cage. Six cyclen-occupied cages surround the large cage - 2 cages either side of the cage along each of the crystallographic axes. It's the cyclen in these occupied cages that directs the size of the 16 MR and therefore the size of the entrance into the large cage. As a consequence of the positioning of the templates a 16 MR channel exists along each of the crystallographic axes (perpendicular to the cyclen in the occupied cages). The cyclen-occupied cages also direct the small channels and leads to the parallel series of alternating diagonal rows of 16 MR and 8 MR channels.

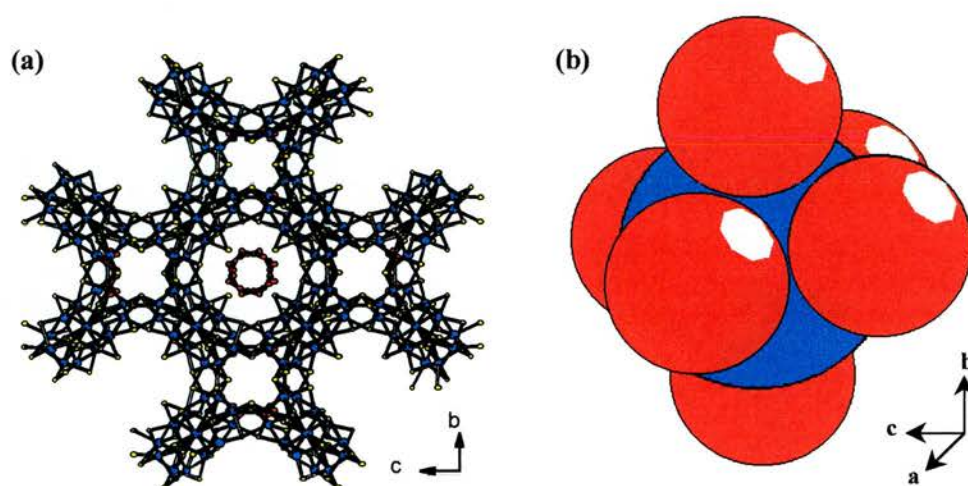


Figure 7.10 (a) Picture of the large cage surrounded by six cyclen-occupied cages forming 16 MR channels in the direction of each crystallographic axes. Colours are the same as figure 7.9. (b) A 3-dimensional illustration showing the positions of the cyclen-occupied cage (red) around the large cage (blue) when we rotate (a) slightly around the *b*-axis.

To understand the bonding and interactions of this structure it is important to consider the unit cell contents and the charge balancing. Although the structure was refined as a pure scandium sulphate, for these calculations it must be remembered that the structure is a sulphate/phosphate mix. The ^{31}P NMR (see figure 7.11a) of

cyclen-ScSPO consolidates the presence of phosphorus by the presence of the three peaks. These may be attributed to the three crystallographically distinct tetrahedral positions. Combining structural data with inorganic analysis indicates a unit cell composition of *ca* $\text{Sc}_{56}\text{S}_{94}\text{P}_{26}\text{O}_{480}\cdot 14(\text{C}_8\text{N}_4\text{H}_{18}^{4+})\cdot 50\text{H}_2\text{O}$.

Although only twelve cyclen molecules could be located crystallographically, there was some residual electron density that may account for two more molecules of cyclen per unit cell and perhaps some crystallographic water. It is likely that the problems associated with disorder in this high symmetry space group made it difficult to locate the remaining cyclens crystallographically. The ^{13}C NMR of cyclen-ScSPO shows two peaks (see figure 7.11b), which could relate to the two crystallographically distinct carbon locations or perhaps two different carbon environments (perhaps a diprotonated cyclen). This is also seen in the ^{13}C NMR of the cyclen-ScSO (see figure 7.12a). However the ^{15}N NMR has only one peak which is suggestive that both carbons have the same environment (see figure 7.12b). Hence I would suggest the two peaks on the ^{13}C NMR are associated with the two distinct crystallographic locations of carbon.

Calculating the charge of the above structural composition leaves an unbalanced charge of -ve 42. However when we consider that 144 of the oxygens in the composition are dangling oxygens, this charge can be compensated by protonating approximately a third of them. These are likely to be disordered over all the dangling oxygen sites it may be predicted that the oxygens which lie closest to protons already existing on the cyclen molecule will not be protonated themselves. Therefore we would have two tetrahedral groups present of SO_3OH and SO_4^{2-} .

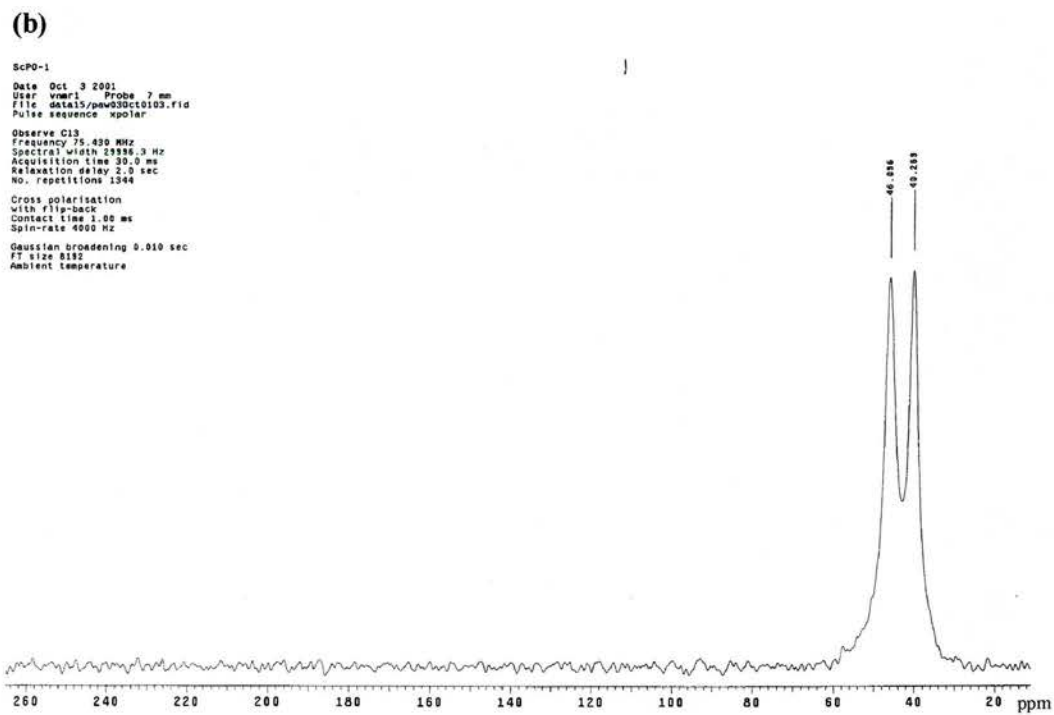
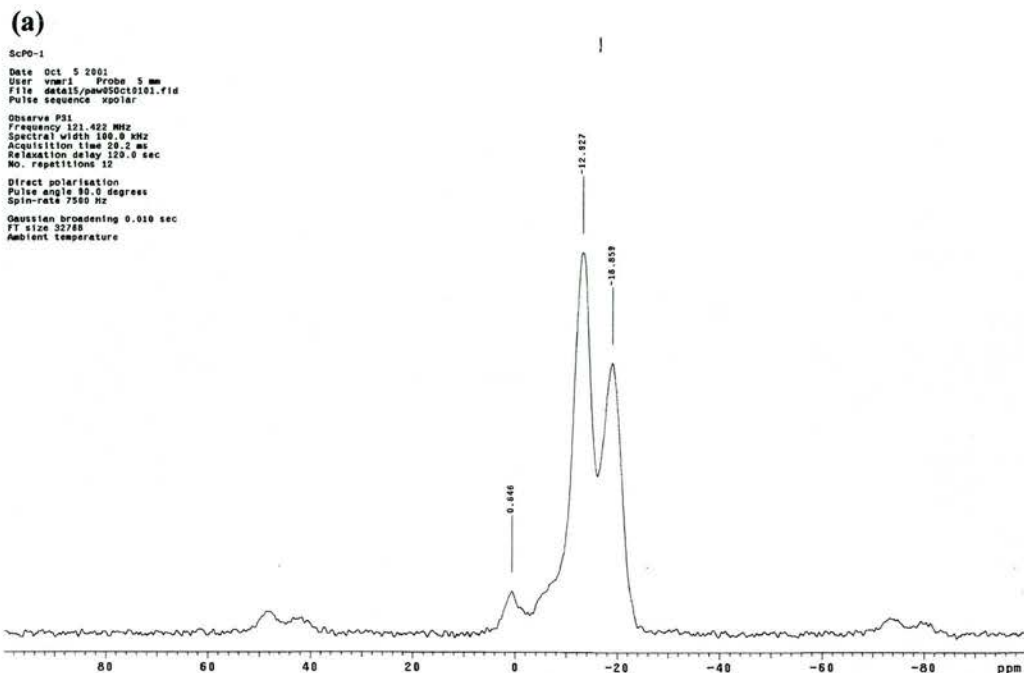


Figure 7.11 NMR spectra of cyclen-ScS/PO (a) ^{31}P , (b) ^{13}C .

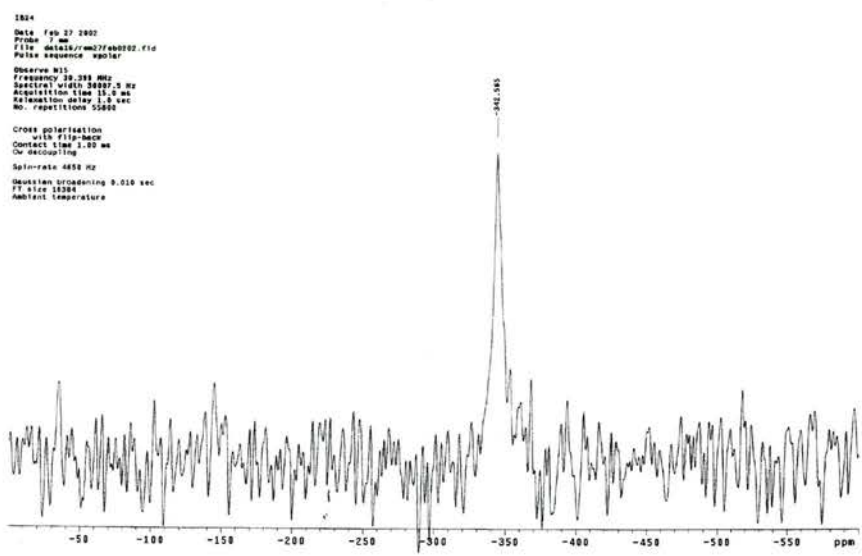
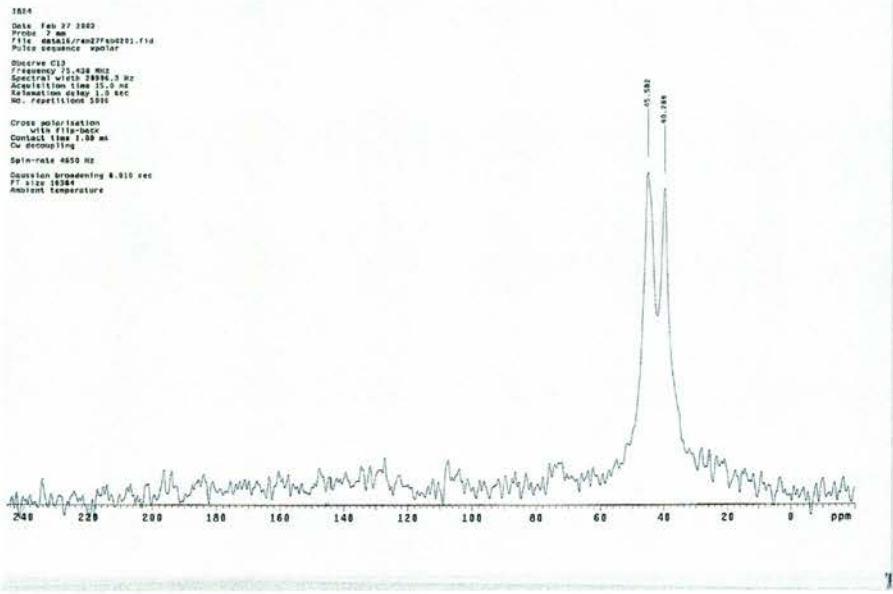


Figure 7.12 NMR spectra of cyclen-ScS/PO (a) ^{13}C , (b) ^{15}N .

7.3.2.2 Structure of cyclen-ScSO

This structure was solved by powder data using the Le Bail method since the data collected was too poor to apply the single-crystal model because of the high background. Both cyclen-ScSO and scandium sulphate were present in the powder pattern. All the peaks relating to each phase are accounted for as show in figure 7.12 The refinement gives an $R=5.24\%$.

The unit cell of the cyclen-ScSO refines in the cubic space group $Pn\bar{3}n$ to give $a=25.21303(129)$. The scandium sulphate refines in $R\bar{3}$ to give $a=4.98364(25)$ and $c=24.05661(108)$.

There was only sulphate present as a T-atom source in the reaction and so this powder pattern provides proof that it is possible to prepare the pure sulphate version of the previously reported cyclen-ScS/PO.

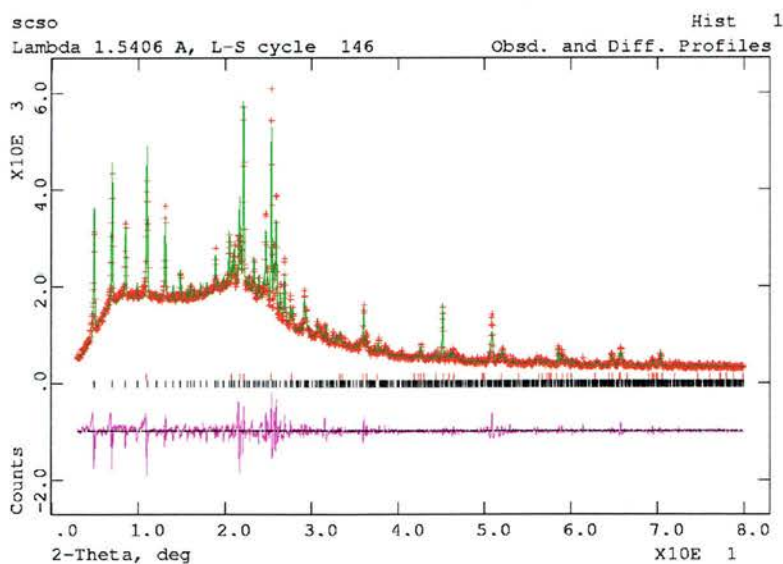


Figure 7.13 Observed (red) and calculated (green) X-ray diffraction pattern for cyclen-ScSO following Le Bail refinement. Vertical ticks indicate positions of allowed reflections in space group $Pn\bar{3}n$. The lower purple trace is the difference plot.

7.3.3 Thermal Analysis

Figure 7.14 contains the thermogravimetric weight loss curves for the cyclen-ScS/PO. The total weight loss is 62.5% due to the loss of water, cyclen and the degradation of the sulphate framework. The final products would compose of scandium oxide and scandium phosphate.

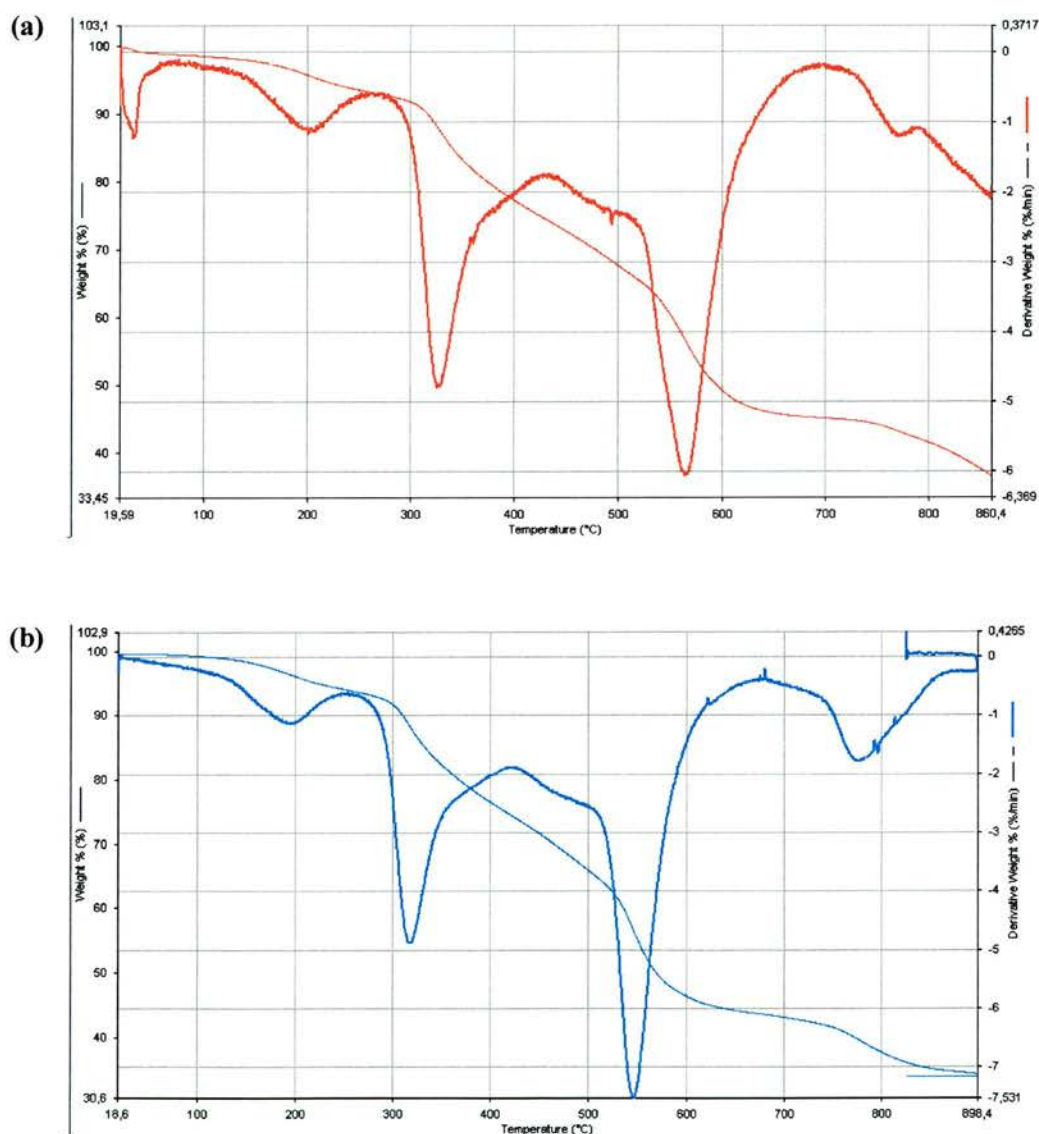


Figure 7.14 TG and DTG curves for cyclen-ScS/PO carried out (a) in air, (b) in helium with connected to MS.

If we examine the TGMS with temperature (shown in figures 7.15 to 7.17) it can be seen that the first peak observed at ~200 °C (or ~8 min) corresponds clearly to water loss. The second peak at ~325 °C (or ~ 14.5 min) relates to some water loss and some decomposition of the sulphate framework: with masses of 64, 48 and 30 corresponding to SO₂. Between temperatures of 400-600 °C there is an intense signal of 44 amu that would correspond to 1/4 of a cyclen molecule (C₂NH₆). As the temperature increases within this range, the signals relating to the cyclen become weaker and the signals relating to sulphate increase (amu=32) as we shift from the burning of the organic to the decomposition of the sulphate framework. At ~780 °C there are signals of 32 and 16 amu which could relate to the decomposition of SO₄²⁻ to SO₂ plus O₂. Thus confirming a weight loss of 62.5 % due to loss of water, sulphate and cyclen and then decomposition of the sulphate framework from the initial composition of *ca* Sc₅₆S₉₄P₂₆O₄₈₀·14(C₈N₄H₁₈²⁺)·50H₂O (FW of ~17357g) to give the final composition of Sc₅₆P₂₆O₁₉₉ (FW of ~6507g).

Table 7.6 Weight losses with temperature as shown by TGMS.

Temperature Range (°C)	Associated Losses	Weight Loss (%)	Total Weight Loss (%)
0-250	H ₂ O	6.25	6.25
250-400	H ₂ O and sulphate	18.5	24.75
400-600	H ₂ O, cyclen, sulphate	26.75	51.5
600-800	sulphate	35.75	62.5

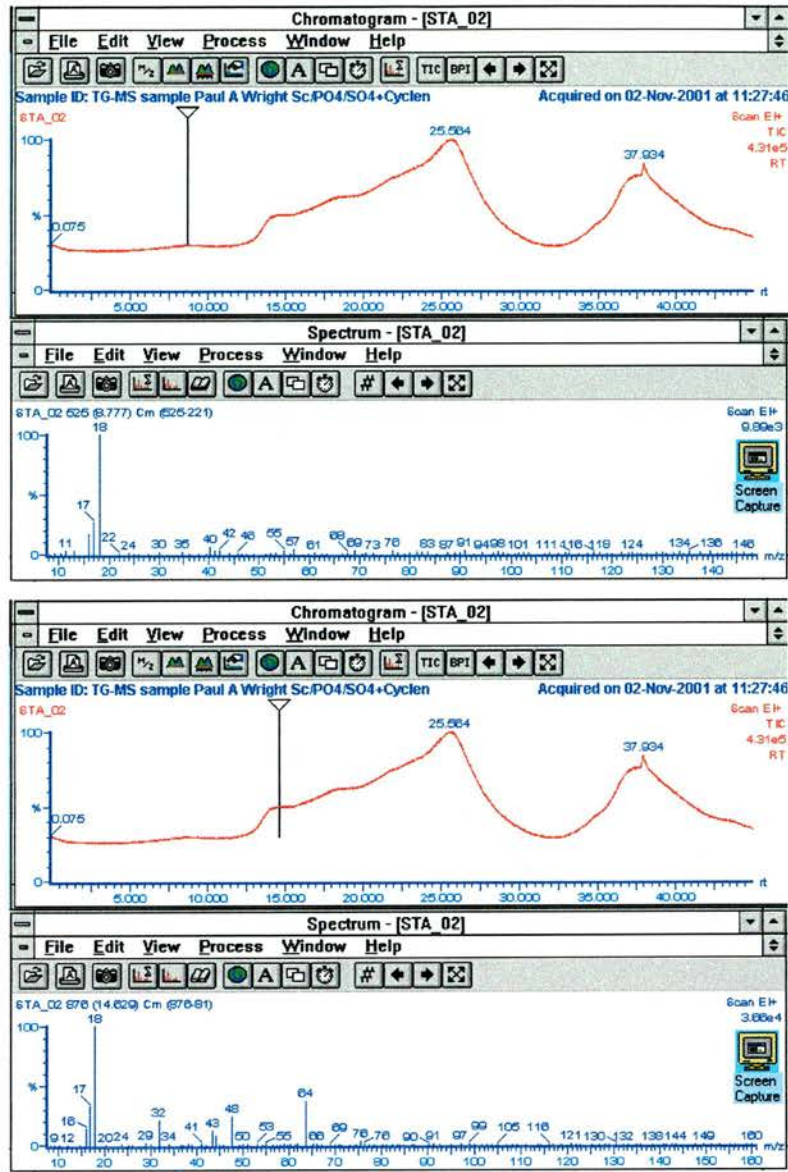


Figure 7.15 TGMS curves for cyclen-ScS/PO carried out at (a) ~200 °C, (b) ~325 °C. These show the loss of water and sulphate groups.

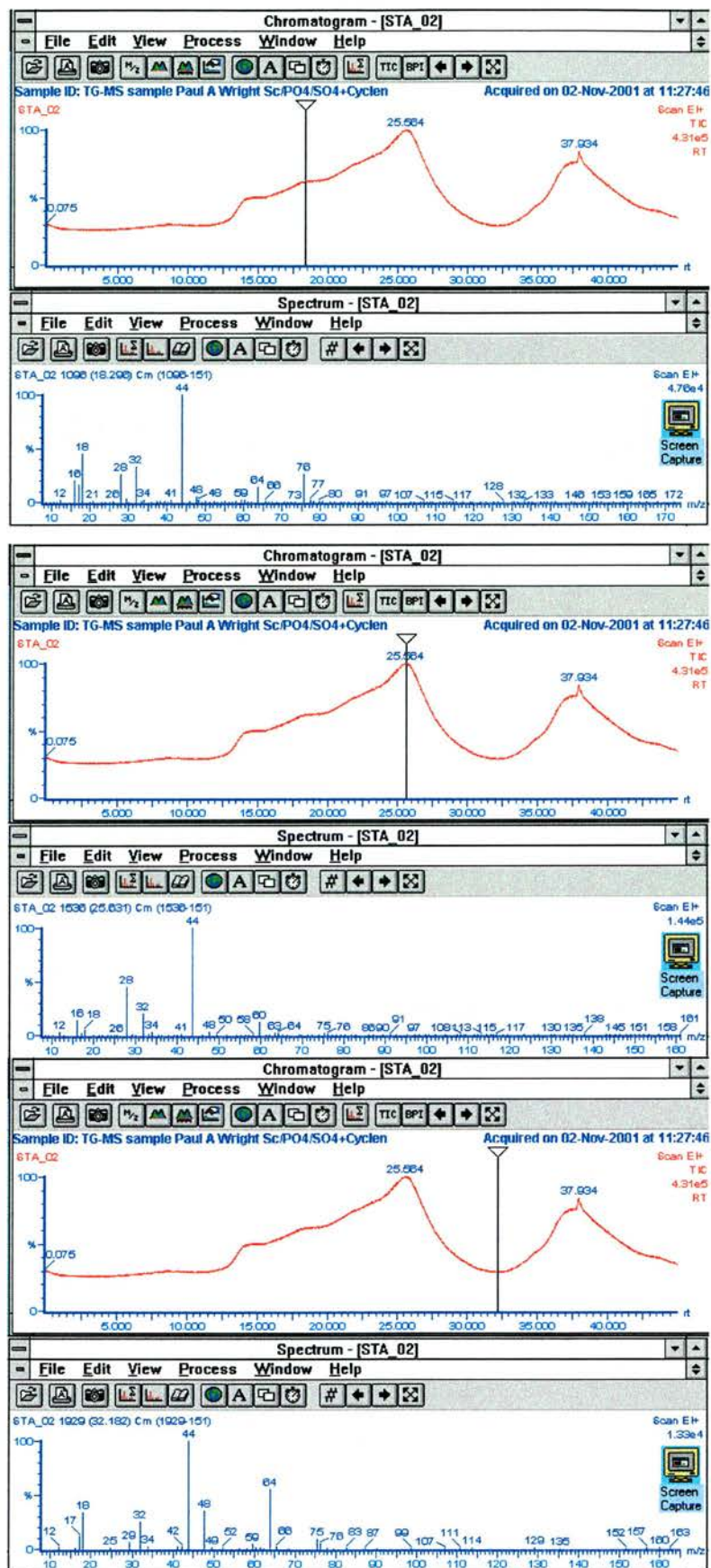


Figure 7.16 TGMS curves for cyclen-ScS/PO carried out at between 400-600 °C. (a) Shows the loss of cyclen. (b) Shows the loss of cyclen and start of the framework decomposition. (c) The continuing loss of cyclen and increasing decomposition of the sulphate framework.

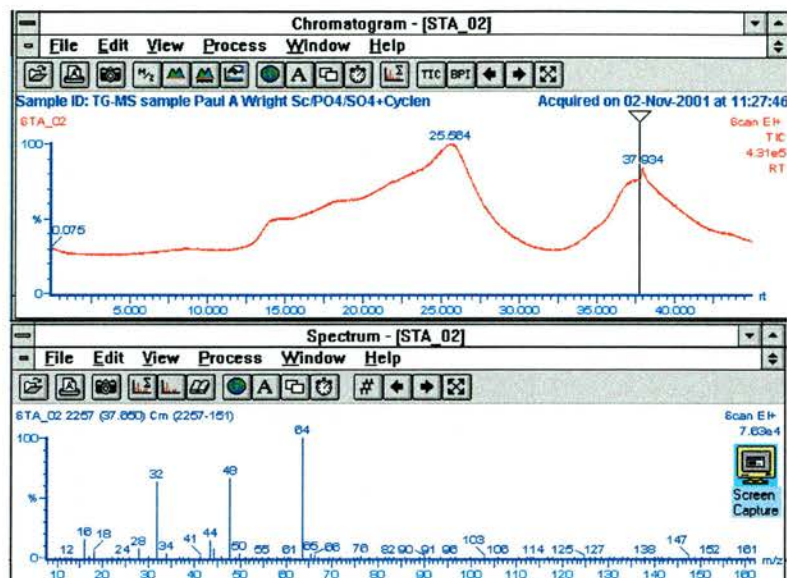


Figure 7.17 TGMS curves for cyclen-ScS/PO showing the decomposition of the sulphate framework at $\sim 780^\circ\text{C}$.

7.4 Conclusions

The structure is novel, but possesses features in common with naturally-occurring sulphates. For example, langbeinite¹⁷ possesses a dense octahedral-tetrahedral framework, and the cubic voltaite, , possesses a three dimensional framework with pores running in three orthogonal directions.¹¹ The demonstration of scandium as a framework-forming element is very promising for the preparation of a range of novel open framework and microporous solids. In particular, the title compound is characterised by the clearly defined building units that link together to form the framework. Parallels may be drawn with the studies of Ferey on iron phosphate systems.¹⁸ The structural rigidity of these units, together with the structure directing action of the cyclen molecule, result in the cage structure in a similar way to rigid units in the structure of vanadyl phosphates¹² and nickel phosphates. Further work is in progress to determine if this same building unit can be connected in different ways to give novel structures.

It is interesting to note that the incorporation of phosphorus into what is mostly a scandium sulphate framework results in the formation of cubic crystals large enough for laboratory XRD studies whereas, the pure sulphate only exists as a crystalline powder. Further work could examine the ratios of phosphorus and sulphur metal sources and a thorough study of the resulting framework compositions.

Although this structure has refined reasonably well it must be noted that the R_{int} has a high value of approximately 35 %. The crystal was very small and perhaps tested the limits of our in-house facilities. However, this could reflect a major problem such as twinning, which could also be responsible for the significant residual electron density. However it is more likely that the residual electron density is due to unmodelled water as there is a great deal of water in this structure. This crystal shall be collected at a synchrotron source to solve this problem.

7.5 References

1. T.J. Barton, L.M. Bull, W.G. Klemperer, D.A. Loy, B. McEnaney, M. Misono, P.A. Monson, G. Pez, G.W. Scherer, J.C. Vartuli and O.M. Yaghi, *Chem. Mater.*, 1999, **11**, 2633.
2. J. Rocha and M.W. Anderson, *Eur. J. Inorg. Chem.*, 2000, **10**, 801.
3. J. Rocha, P. Ferreira, Z. Lin, P. Brandao, A. Ferreira and J.D.P. de Jesus, *J. Phys. Chem. B*, 1998, **102**, 4739.
4. J. Rocha, P. Ferreira, Z. Lin, J.R. Agger and M.W. Anderson, *Chem. Commun.*, 1998, **12**, 1269.
5. M. S. Dadachov, J. Rocha, A. Ferreira, Z. Lin and M.W. Anderson, *Chem. Commun.*, 1997, **21**, 2371.
6. A.I. Bortun, L. N. Bortun and A. Clearfield, *Chem. Mater.*, 1997, **9**, 1854.

7. P. Ferreira, A. Ferreira, J. Rocha and M.R. Soares, *Chem. Mater.*, 2001, **13**, 355.
8. J.R. Agger and M.W. Anderson, *J. Phys. Chem. B.*, **103**, 957.
9. R.A. Dilanian, F. Izumi, K. Itoh and T. Kamiyama, *J. Phys. Soc. Jap.*, 1999, **68**, 3893.
10. A. Choudhury, J. Krishnamoorthy and C.N.R. Rao, *Chem. Commun.*, 2001, 2610.
11. K. Mereiter, *Tschermaks Miner. Petrogr. Mitt.*, 1972, **18**, 185.
12. M.H. Hey, C. Milton and E.J. Dwornik, *Mineralogical Magazine*, 1982, **46**, 493.
13. M.E. Davis and R.F. Lobo, *Chem. Mater.*, 1992, **4**, 756.
14. P.A. Wright, M.J. Maple, A.M.Z. Slawin, V. Patinec, R.A. Aitken, S. Welsh and P.A. Cox, *J. Chem. Soc., Dalton Trans.*, 2000, 1243.
15. V. Patinec, P.A. Wright, P. Lightfoot, R.A. Aitken and P.A. Cox, *J. Chem. Soc., Dalton Trans.*, 1999, 1721.
16. D. Wragg and R.E. Morris, *J. Mater. Chem.*, 2001, **11**, 513.
17. D.Y. Pushcharovsky, J. Lima de Faria and R.K. Rastsvetaeva, *Zeit. Krist.*, 1998, **214**, 141.
18. M. Riou-Cavellec, D. Riou and G. Ferey, *Inorganica Chimica Acta*, 1999, **291**, 317.
19. M. Schindler and W.H. Baur, *Angew. Chem. Int. Ed. Engl.*, 1997, **36**, 91.

Chapter 8 - Conclusions and Further Work

8.1 Summary

This thesis has shown how synchrotron X-ray radiation can be used to address problems in zeolite science by studying very small crystals. The majority of the studies reported in this thesis would not have been possible without synchrotron X-ray radiation.

In chapter four, I showed how the use of station 9.8 could be used to study the structures of as-made ferrierite and the thermal properties of the calcined version. Synchrotron radiation provided the high-resolution necessary to allow the study of atomic changes with temperature enabling the negative thermal behaviour of calcined siliceous ferrierite to be modelled. In addition the high intensity of the beam allowed the crystallographic location of fluoride to be found for the first time in siliceous ferrierite.

In chapter five, I showed how station 9.8 could be used to study the structure of as-made ITQ-4.¹ This result was particularly revealing, as it showed the higher quality of single crystal data could reveal more subtle structural features than is possible from powder data alone.² In this case, where the structure of [BQo,F]-ITQ-4 was shown to be noncentrosymmetric, the results opened up questions regarding how this ordering occurs. Similarly chapter six reports the study of as-made siliceous chabazite and MAPO-17. The combination of single-crystal synchrotron X-ray diffraction studies with low temperatures allowed the disorder in these zeolites to be accurately modelled. Again the high intensity of the synchrotron radiation allowed the location of fluoride within the framework.

Chapter seven reported the synthesis and characterisation of a novel scandium sulphate templated by the azamacrocycle, cyclen. This highlighted the potential for a great number of new octahedral/tetrahedral microporous structures containing building units and template interactions, which differ to those reported. In addition this work revealed the potential for the incorporation of different metals (in this case scandium) into the microporous metal oxide frameworks.

8.2 Significance of synchrotron radiation

Station 9.8 (microcrystal diffraction station) at the CCRLC Synchrotron Radiation Source, Daresbury Laboratories UK provided some enhanced properties, which all contributed to the advancement of our understanding of zeolites. These include:

- The higher intensity of the X-rays allowed the collection of data from microcrystals. It is extremely difficult to grow crystals large enough to study on anything other than a synchrotron source.
- As-made [BQo1,F]-ITQ-4 was originally solved from powder methods.² A single-crystal study at station 9.8 showed this study to be wrong.¹ The extra detail from the single-crystal X-ray diffraction study was needed.
- It would not have been possible to solve the disordered structures of as-made ITQ-4, chabazite, and MAPO-17 from powder x-ray diffraction data. Station 9.8 allowed the collection of data from microcrystals coupled with a low temperature to enable a detailed structural study. Again the extra detail allowed the location of fluoride in chabazite.

8.3 Significance of the location of fluoride

The challenge to the zeolite chemist is to understand the interplay between the host framework and the species occluded within the framework (templates and

fluoride).³ Unravelling these details should provide an improved understanding of synthetic influences, which should allow a more rational approach in designing zeolites. My thesis reports the location of fluoride in various zeolite frameworks and has allowed some progress in this area.

- Fluoride was located for the first time in both as-made siliceous ferrierite and chabazite.
- Fluoride was crystallographically located in ITQ-4 and was the first crystallographic proof of the $[\text{SiO}_4\text{F}]^-$ group that had been previously reported by NMR.^{1,4} That the presence of fluoride causes such a dramatic change in symmetry and ordering of the template may influence how non-linear optical materials are prepared.
- It was postulated that electrostatic and distortion effects were responsible for the noncentrosymmetric ordering of both the fluoride and the template. This work was instrumental in developing similar studies in zeolites. A study of STF revealed that similar electrostatic and distortion effects control the location and content of fluoride.⁵ Fluoride was always found to be attached to a silicon that is part of a 4-ring in ITQ-4, ITQ-9, and chabazite. Except for ferrierite which was connected to a 5-ring. However only one fluorine may attach to each 4-ring for stability reasons. Since 4-rings are present in a great number of zeolite structures this may be very important in the control of synthesis.
- In ITQ-4 and chabazite it was clearly seen that the template was to some degree positioned by the attraction between its positive charge and the negative charge imposed on the framework by the incorporation of fluoride.

It is hoped that further work towards the location of fluoride in zeolites may elucidate a reaction mechanism.

8.4 Significance of the synthesis of novel materials

A larger range of porous structures would greatly widen the potential applications for zeolites. So there is a great interest in developing novel structures. This was the driving force for the synthesis of the scandium sulphate reported in chapter seven. The results were significant in the following ways.

- This was the first scandium-containing microporous material. The demonstration of scandium as a framework-forming element is very promising for the preparation of a range of novel open framework and microporous materials.
- The structure is characterised by the clearly defined Sc_7S_{12} building units that link together to form the framework. Parallels can be drawn with the studies of Ferey on iron phosphate systems.⁶ The structural rigidity of these units, together with the structure directing action of the cyclen molecule, result in a cage structure in a similar way to rigid units in the structure of vanadyl phosphates⁷ and nickel phosphates. An examination of similar reactions could determine if this structural building unit could give other novel structures.

8.5 Further Work

Throughout this thesis I have stressed the importance of gaining as much information concerning zeolite structures as possible. So it is important to continue to study all aspects of these structures, from negative thermal expansion to the location of templates and other framework species. I would highlight the need for low temperature single-crystal studies of as-made zeolites towards a greater understanding of synthetic influences.

The location of fluoride has proved to be extremely important in the understanding of reactions. Fluoride used to be thought of as just a mineralising

agent, however these days it is recognised that its role can be important in the formation of structures. Further work would desire the single-crystal study of all zeolites prepared in fluoride media. This would be of particular interest in the sixty-one zeolites, which contain 4-rings since fluoride seems to preferentially bond to these building units. As a starting point it would be great to study more of the ITQ structures (similar to ITQ-4 and ITQ-9) which are prepared in fluoride media. The structures of ITQ-1⁸, ITQ-3⁹, ITQ-7¹⁰, ITQ-8, ITQ-10 and ITQ-14¹¹ all lack single-crystal studies, which may reveal structural details as yet unseen. Through this work a bigger picture of fluoride in zeolite structures can be built and perhaps this can reveal some very useful details in zeolite science.

MAPO-17 illustrated that metal cations with lower oxidation state can be incorporated to supply the negative charge needed to charge-balance the template instead of fluoride. By examining a metallo-substituted ITQ-4 such as an aluminosilicate or a borosilicate the role of fluorine can be clarified. I would postulate that a metallo-substituted ITQ-4 would be centrosymmetric since it lacks the effects of the fluoride. However this would assume that the aluminium or boron was randomly distributed around the framework. The other possibility would reveal that the template and the negative charge source (fluoride or metallo-substitute) must act in a complimentary manner.

There is a great desire for new zeolite structures with varying pore sizes to allow the application of these materials to expand. I have managed to introduce scandium to produce a mixed octahedral-tetrahedral framework oxide. This new archetypal material introduces tremendous scope for new structures and many potential novel applications in areas such as batteries, optoelectronics and sensors. Further work

would look at incorporating a whole series of templates into scandium containing mixed octahedral-tetrahedral frameworks.

8.6 References

1. I. Bull, L.A. Villaescusa, S.J. Teat, M.A. Cambor, P.A. Wright, P. Lightfoot and R.E. Morris, *J. Am. Chem. Soc.*, 2000, **122**, 7128.
2. P.A. Barrett, M.A. Cambor, A. Corma, R.H. Jones and L.A. Villaescusa, *Chem. Mater.*, 1997, **9**, 1713.
3. R.E. Morris and P.A. Wright, *Chem. Ind.*, 1998, 256.
4. H. Koller, A. Wölker, L.A. Villaescusa, M.J. Diaz-Cabañas, S. Valencia and M.A. Cambor, *J. Am. Chem. Soc.*, 1999, **121**, 3368.
5. L.A. Villaescusa, P.S. Wheatley, I. Bull, P. Lightfoot and R.E. Morris, *J. Am. Chem. Soc.*, 2001, **123**, 8797.
6. M. Riou-Cavellec, D. Riou and G. Ferey, *Inorganica Chimica Acta*, 1999, **291**, 317.
7. M. Schindler and W.H. Baur, *Angew. Chem. Int. Ed.*, 1997, **36**, 91.
8. M.A. Cambor, A. Corma and M.-J. Diaz-Cabañas, *J. Phys. Chem. B*, 1998, **102**, 44.
9. M.A. Cambor, A. Corma, P. Lightfoot, L.A. Villaescusa and P.A. Wright, *Angew. Chem. Int. Ed.*, 1997, **36**, 2659.
10. L.A. Villaescusa, P.A. Barrett and M.A. Cambor, *Angew. Chem. Int. Ed.*, 1999, **38**, 1997.
11. M.-J. Diaz-Cabañas, M.A. Cambor, A. Lui, T. Ohsuna and O. Terasaki, *J. Mater. Chem.*, 2002, **12**, 249.
12. L.A. Villaescusa, P.A. Barrett, M. Kalwei, H. Koller and M.A. Cambor, *Chem. Mater.*, 2001, **13**, 2332.

Chapter 8 - Conclusions and Further Work

8.1 Summary

This thesis has shown how synchrotron X-ray radiation can be used to address problems in zeolite science by studying very small crystals. The majority of the studies reported in this thesis would not have been possible without synchrotron X-ray radiation.

In chapter four, I showed how the use of station 9.8 could be used to study the structures of as-made ferrierite and the thermal properties of the calcined version. Synchrotron radiation provided the high-resolution necessary to allow the study of atomic changes with temperature enabling the negative thermal behaviour of calcined siliceous ferrierite to be modelled. In addition the high intensity of the beam allowed the crystallographic location of fluoride to be found for the first time in siliceous ferrierite.

In chapter five, I showed how station 9.8 could be used to study the structure of as-made ITQ-4.¹ This result was particularly revealing, as it showed the higher quality of single crystal data could reveal more subtle structural features than is possible from powder data alone.² In this case, where the structure of [BQoI,F]-ITQ-4 was shown to be noncentrosymmetric, the results opened up questions regarding how this ordering occurs. Similarly chapter six reports the study of as-made siliceous chabazite and MAPO-17. The combination of single-crystal synchrotron X-ray diffraction studies with low temperatures allowed the disorder in these zeolites to be accurately modelled. Again the high intensity of the synchrotron radiation allowed the location of fluoride within the framework.

Chapter seven reported the synthesis and characterisation of a novel scandium sulphate templated by the azamacrocycle, cyclen. This highlighted the potential for a great number of new octahedral/tetrahedral microporous structures containing building units and template interactions, which differ to those reported. In addition this work revealed the potential for the incorporation of different metals (in this case scandium) into the microporous metal oxide frameworks.

8.2 Significance of synchrotron radiation

Station 9.8 (microcrystal diffraction station) at the CCRLC Synchrotron Radiation Source, Daresbury Laboratories UK provided some enhanced properties, which all contributed to the advancement of our understanding of zeolites. These include:

- The higher intensity of the X-rays allowed the collection of data from microcrystals. It is extremely difficult to grow crystals large enough to study on anything other than a synchrotron source.
- As-made [BQo,F]-ITQ-4 was originally solved from powder methods.² A single-crystal study at station 9.8 showed this study to be wrong.¹ The extra detail from the single-crystal X-ray diffraction study was needed.
- It would not have been possible to solve the disordered structures of as-made ITQ-4, chabazite, and MAPO-17 from powder x-ray diffraction data. Station 9.8 allowed the collection of data from microcrystals coupled with a low temperature to enable a detailed structural study. Again the extra detail allowed the location of fluoride in chabazite.

8.3 Significance of the location of fluoride

The challenge to the zeolite chemist is to understand the interplay between the host framework and the species occluded within the framework (templates and

fluoride).³ Unravelling these details should provide an improved understanding of synthetic influences, which should allow a more rational approach in designing zeolites. My thesis reports the location of fluoride in various zeolite frameworks and has allowed some progress in this area.

- Fluoride was located for the first time in both as-made siliceous ferrierite and chabazite.
- Fluoride was crystallographically located in ITQ-4 and was the first crystallographic proof of the $[\text{SiO}_4\text{F}]^-$ group that had been previously reported by NMR.^{1,4} That the presence of fluoride causes such a dramatic change in symmetry and ordering of the template may influence how non-linear optical materials are prepared.
- It was postulated that electrostatic and distortion effects were responsible for the noncentrosymmetric ordering of both the fluoride and the template. This work was instrumental in developing similar studies in zeolites. A study of STF revealed that similar electrostatic and distortion effects control the location and content of fluoride.⁵ Fluoride was always found to be attached to a silicon that is part of a 4-ring in ITQ-4, ITQ-9, and chabazite. Except for ferrierite which was connected to a 5-ring. However only one fluorine may attach to each 4-ring for stability reasons. Since 4-rings are present in a great number of zeolite structures this may be very important in the control of synthesis.
- In ITQ-4 and chabazite it was clearly seen that the template was to some degree positioned by the attraction between its positive charge and the negative charge imposed on the framework by the incorporation of fluoride.

It is hoped that further work towards the location of fluoride in zeolites may elucidate a reaction mechanism.

8.4 Significance of the synthesis of novel materials

A larger range of porous structures would greatly widen the potential applications for zeolites. So there is a great interest in developing novel structures. This was the driving force for the synthesis of the scandium sulphate reported in chapter seven. The results were significant in the following ways.

- This was the first scandium-containing microporous material. The demonstration of scandium as a framework-forming element is very promising for the preparation of a range of novel open framework and microporous materials.
- The structure is characterised by the clearly defined Sc_7S_{12} building units that link together to form the framework. Parallels can be drawn with the studies of Ferey on iron phosphate systems.⁶ The structural rigidity of these units, together with the structure directing action of the cyclen molecule, result in a cage structure in a similar way to rigid units in the structure of vanadyl phosphates⁷ and nickel phosphates. An examination of similar reactions could determine if this structural building unit could give other novel structures.

8.5 Further Work

Throughout this thesis I have stressed the importance of gaining as much information concerning zeolite structures as possible. So it is important to continue to study all aspects of these structures, from negative thermal expansion to the location of templates and other framework species. I would highlight the need for low temperature single-crystal studies of as-made zeolites towards a greater understanding of synthetic influences.

The location of fluoride has proved to be extremely important in the understanding of reactions. Fluoride used to be thought of as just a mineralising

agent, however these days it is recognised that its role can be important in the formation of structures. Further work would desire the single-crystal study of all zeolites prepared in fluoride media. This would be of particular interest in the sixty-one zeolites, which contain 4-rings since fluoride seems to preferentially bond to these building units. As a starting point it would be great to study more of the ITQ structures (similar to ITQ-4 and ITQ-9) which are prepared in fluoride media. The structures of ITQ-1⁸, ITQ-3⁹, ITQ-7¹⁰, ITQ-8, ITQ-10 and ITQ-14¹¹ all lack single-crystal studies, which may reveal structural details as yet unseen. Through this work a bigger picture of fluoride in zeolite structures can be built and perhaps this can reveal some very useful details in zeolite science.

MAPO-17 illustrated that metal cations with lower oxidation state can be incorporated to supply the negative charge needed to charge-balance the template instead of fluoride. By examining a metallo-substituted ITQ-4 such as an aluminosilicate or a borosilicate the role of fluorine can be clarified. I would postulate that a metallo-substituted ITQ-4 would be centrosymmetric since it lacks the effects of the fluoride. However this would assume that the aluminium or boron was randomly distributed around the framework. The other possibility would reveal that the template and the negative charge source (fluoride or metallo-substitute) must act in a complimentary manner.

There is a great desire for new zeolite structures with varying pore sizes to allow the application of these materials to expand. I have managed to introduce scandium to produce a mixed octahedral-tetrahedral framework oxide. This new archetypal material introduces tremendous scope for new structures and many potential novel applications in areas such as batteries, optoelectronics and sensors. Further work

would look at incorporating a whole series of templates into scandium containing mixed octahedral-tetrahedral frameworks.

8.6 References

1. I. Bull, L.A. Villaescusa, S.J. Teat, M.A. Camblor, P.A. Wright, P. Lightfoot and R.E. Morris, *J. Am. Chem. Soc.*, 2000, **122**, 7128.
2. P.A. Barrett, M.A. Camblor, A. Corma, R.H. Jones and L.A. Villaescusa, *Chem. Mater.*, 1997, **9**, 1713.
3. R.E. Morris and P.A. Wright, *Chem. Ind.*, 1998, 256.
4. H. Koller, A. Wölker, L.A. Villaescusa, M.J. Diaz-Cabañas, S. Valencia and M.A. Camblor, *J. Am. Chem. Soc.*, 1999, **121**, 3368.
5. L.A. Villaescusa, P.S. Wheatley, I. Bull, P. Lightfoot and R.E. Morris, *J. Am. Chem. Soc.*, 2001, **123**, 8797.
6. M. Riou-Cavellec, D. Riou and G. Ferey, *Inorganica Chimica Acta*, 1999, **291**, 317.
7. M. Schindler and W.H. Baur, *Angew. Chem. Int. Ed.*, 1997, **36**, 91.
8. M.A. Camblor, A. Corma and M.-J. Diaz-Cabañas, *J. Phys. Chem. B*, 1998, **102**, 44.
9. M.A. Camblor, A. Corma, P. Lightfoot, L.A. Villaescusa and P.A. Wright, *Angew. Chem. Int. Ed.*, 1997, **36**, 2659.
10. L.A. Villaescusa, P.A. Barrett and M.A. Camblor, *Angew. Chem. Int. Ed.*, 1999, **38**, 1997.
11. M.-J. Diaz-Cabañas, M.A. Camblor, A. Lui, T. Ohsuna and O. Terasaki, *J. Mater. Chem.*, 2002, **12**, 249.
12. L.A. Villaescusa, P.A. Barrett, M. Kalwei, H. Koller and M.A. Camblor, *Chem. Mater.*, 2001, **13**, 2332.

